A QUANTITATIVE STUDY OF THE RADIANCE DISTRIBUTION AND ITS VARIATION IN OCEAN SURFACE WATERS

By

Jianwei Wei

Submitted in partial fulfillment of the requirements
for the degree of Doctor of Philosophy

at

Dalhousie University
Halifax, Nova Scotia
February 2013

DALHOUSIE UNIVERSITY

DEPARTMENT OF OCEANOGRAPHY

The undersigned hereby certify that they have read and recommend to the Faculty of Graduate Studies for acceptance a thesis entitled "A QUANTITATIVE STUDY OF THE RADIANCE DISTRIBUTION AND ITS VARIATION IN OCEAN SURFACE WATERS" by Jianwei Wei in partial fulfilment of the requirements for the degree of Doctor of Philosophy.

Dated: February 21, 2013

External Examiner: _____

Research Supervisor: _____

Examining Committee: _____

_____

_____

_____

_____

Departmental Representative: _____

DALHOUSIE UNIVERSITY

DATE: February 21, 2013

AUTHOR: Jianwei Wei

TITLE: A QUANTITATIVE STUDY OF THE RADIANCE DISTRIBUTION AND ITS VARIATION IN OCEAN SURFACE WATERS

DEPARTMENT OR SCHOOL: Department of Oceanography

DEGREE: PhD CONVOCATION: May YEAR: 2013

_____

Signature of Author

I dedicate the thesis work to my family – Yinglin, Xiaoxiao and Yangyang.

Table of Contents

List of Tables

List of Figures

Abstract

The radiance distribution provides complete information regarding the geometrical structure of the ambient light field within the ocean. A quantitative study of the radiance field in the dynamic ocean water is presented in this thesis work. The study starts with the development of a novel radiance camera for the measurement of the full spherical radiance distribution at the ocean surface and depth. Nonlinear response functions are designed and advanced radiometric calibrations are developed. The resulting camera measures the radiance distribution in absolute units over an extremely high dynamic range at fast rates. With the newly obtained radiance data, I have examined the fine structure of both the downwelling and upwelling radiance distribution and its variation with depth in optically diverse water types. The fully specified radiance distribution data are used to derive all apparent optical properties and some inherent optical properties including the absorption coefficient. With the camera fixed at shallow depths, I have observed and determined the sea surface wave disturbance of the radiance distribution. It is found that the radiance fluctuates anisotropically with regard to its amplitude and periodicity. Typical spatial structures of the dynamic radiance field are identified and shown relevant to the surface waves and the solar zenith angles. The variability in the radiance field also propagates to the irradiance field; the variability is pronounced in measured irradiance depth profiles in the upper layers of the ocean. The statistics of the irradiance fluctuations along the water depth, including the dominant frequency and coefficient of variation, are derived using wavelet techniques and fitted to novel analytic models. The results from the irradiance depth-profile decomposition are in agreement with theoretical models and other independent measurements. This thesis work represents the first attempt to quantify the full light field and its variability in dynamic ocean waters and is of significant relevance to many other optics-related applications.

List of Abbreviations and Symbols Used

a	Absorption coefficient	m^{-1}
$\alpha_{1/2}$	Half angle	deg
ANOVA	Analysis of variance	
AOP	Apparent optical property; plural form: AOPs	
b	Scattering coefficient	m^{-1}
b_b	Backscattering coefficient	m^{-1}
β	Volume scattering function	$m^{-1}\ sr^{-1}$
$\tilde{\beta}$	Scattering phase function, $\tilde{\beta} = \beta/b$	sr^{-1}
BMP	Bi-model pattern	
BSF	Beam spread function	
c	Beam attenuation coefficient, $c = a + b$	m^{-1}
CCD	Charge-coupled device	
CDOM	Colored dissolved organic matter	
$\overline{Chl}$	Average chlorophyll concentration	$mg\ m^{-3}$
CID	Charge injection device	
CMOS	Complementary Metal-Oxide Semiconductor	
C_p	Phase speed	$m\ s^{-1}$
CTD	Conductivity, Temperature and Depth	
CV	Coefficient of variation	dimensionless
CWT	Continuous wavelet transform	
d	Optical density	dimensionless
δ	Wave steepness	dimensionless
df	Degree of freedom	
DOLP	Degree of linear polarization	
ECP	Extreme CV pattern	
E_d	Downwelling plane irradiance	$\mu Wcm^{-2}nm^{-1}$
E_{net}	Net irradiance, $E_{net} = E_d - E_u$	$\mu Wcm^{-2}nm^{-1}$
E_{od}	Downwelling scalar irradiance	$\mu Wcm^{-2}nm^{-1}$

E_{ou}	Upwelling scalar irradiance	$\mu Wcm^{-2}nm^{-1}$
E_s	Downwelling plane irradiance above sea surface	$\mu Wcm^{-2}nm^{-1}$
E_u	Upwelling plane irradiance	$\mu Wcm^{-2}nm^{-1}$
EVD	Extreme value distribution	
F	A factor relating f_p to water depth	$[m\ s^{-2}]^{1/2}$
f	Temporal frequency	s^{-1} or Hz
FOV	Field of view	deg
f_p	Dominant frequency	s^{-1} or Hz
F_s	Instrument sampling rate	Hz
FT	Fourier transform	
FWHM	Full width at half maximum	nm or sr or degrees
g	Gravitational acceleration	$m\ s^{-2}$
H	Sea wave height	m
HDR	High dynamic range	
I_n	Normalized irradiance residuals	dimensionless
IOP	Inherent optical property; plural form: IOPs	
k	Wave number	m^{-1}
K_{cv}	Rate of change of the CV with depth	m^{-1}
K_d	Diffuse attenuation coefficient for E_d	m^{-1}
K_L	Diffuse attenuation coefficient for radiance	m^{-1}
K_{net}	Diffuse attenuation coefficient for E_{net}	m^{-1}
K_{od}	Diffuse attenuation coefficient for E_{od}	m^{-1}
K_{ou}	Diffuse attenuation coefficient for E_{ou}	m^{-1}
K_u	Diffuse attenuation coefficient for E_u	m^{-1}
$L(\theta,\varphi)$	Radiance	$\mu Wcm^{-2}sr^{-1}nm^{-1}$
$\bar{L}$	Mean of the radiance	$\mu Wcm^{-2}sr^{-1}nm^{-1}$
L_a	Incident radiance	$\mu Wcm^{-2}sr^{-1}nm^{-1}$
λ	Light wavelength	nm
Λ	Sea wave length	m
L_d	Downwelling radiance in water	$\mu Wcm^{-2}sr^{-1}nm^{-1}$
L_u	Upwelling nadir radiance, $L(\theta = 180°)$	$\mu Wcm^{-2}sr^{-1}nm^{-1}$

MC	Monte Carlo	
$\bar{\mu}$	Average cosine for total light field	dimensionless
$\bar{\mu}_d$	Downwelling average cosine	dimensionless
$\bar{\mu}_u$	Upwelling average cosine	dimensionless
n_a	Index of refraction of air (=1)	dimensionless
NIST	National Institute of Standards and Technology	
n_w	Index of refraction of sea water (=1.34)	dimensionless
OCR	Ocean color radiometer	
OD	Optical depth	dimensionless
ω	Angular frequency	rad s^{-1}
Ω	Solid angle	sr
ω_o	Single scattering albedo	dimensionless
PDF	Probability distribution function	
φ	Azimuth angle	degrees or radians
PPA	Plane-parallel assumption	
PSD	Power spectral density	
PSF	Point spread function	
ψ	Scattering angle	degrees or radians
Q	Q factor, $Q = E_u/L_u$	sr
R	Irradiance reflectance, $R = E_u/E_d$	dimensionless
RadCam	Radiance distribution camera	
RMSE	Root mean square error	
R_{sr}	Remote sensing reflectance	sr^{-1}
RTE	Radiative transfer equation	
S	Wavelet scale	second
σ_L	Standard deviation of the radiance time series	$\mu W cm^{-2} sr^{-1} nm^{-1}$
SMAPD	Symmetric mean absolute percentage difference	
t	Observation time	second
T	Fourier period	second
θ	Zenith angle	degrees or radians
θ_a	Incident angle in air	deg

θ_{cr}	Critical angle	deg
θ_s	Solar zenith angle in air	degrees or radians
θ_{sw}	Solar zenith angle in water	degrees or radians
θ_w	Refractive angle in water	degrees or radians
T_p	Dominant period	second
w_s	Instrument fall speed	m s^{-1}
W_n	Modulus of the wavelet transform	
WT	Wavelet transform	
z	Water depth	m
z_f	Focal depth	m
ζ	Sea surface instantaneous elevation	m
ζ_{xy}	Sea surface slope	degrees or radians

Acknowledgements

I am very lucky to work with some of the most outstanding scientists and engineers in the field of ocean optics while I am pursuing my PhD. My supervisor Dr. Marlon Lewis is an insightful oceanographer and always has the big picture of ocean in mind. I am extremely grateful to his consistent support, encouragement and guidance throughout the thesis work.

My committee members Drs. John Cullen, Anthony Bowen, Tetjana Ross, Susanne Craig and Randall Martin are especially acknowledged for their comments, criticisms and help in shaping this thesis work. And it is a great honor to have Dr. Kendall Carder, the 2012 Jerlov award recipient, as the external examiner of my thesis defense committee.

I am really thankful to the engineers in Satlantic LP for their assistance, especially Dr. Ronnie Van Dommelen, who helped with technical development, radiometric experiments, field tests and computer programming. I would also like to express my gratitude to my research collaborators who influenced my research along the way, Dr. Kenneth Voss from University of Miami and Dr. Christopher Zappa from Columbia University. Many lab staffs, especially Dr. Daisuke Hasegawa, Richard Davis and Gerri Hammer are thanked for their assistance.

This study was funded by the Office of Naval Research (ONR) under contracts of N00014-04-C-0132, N00014-07-C-0139 and N00014-09-C-0084, and the MITACS Accelerate PhD Fellowship (IT01026).

Chapter 1. Introduction

1.1. Motivation

The sun emits electromagnetic radiation over a wide wavelength spectrum, including ultraviolet (10-400 nm), visible (400-700 nm) and infrared and beyond (>700 nm). Energy in the visible bands dominates the total energy and is able to penetrate into the depths of the ocean. Characterization of propagation of the visible light and its temporal and spatial variability in the upper ocean is fundamental to the description of many oceanographic processes [*Dickey and Falkowski*, 2002; *Dickey et al.*, 2011; and references therein]. For example, as one of the most important contributors to the total net primary productivity on the planet [*Falkowski et al.*, 2003], phytoplankton is very sensitive to the variability of the light field in the upper ocean [*Falkowski*, 1984; *Litchman*, 2000; *Platt and Jassby*, 1976; *Ryther*, 1956; *Walsh and Legendre*, 1983]. The absorption of solar radiation heats and stratifies the upper ocean with implications for physical transport of nutrients and gases [*Lewis et al.*, 1988; *Lewis et al.*, 1986; *Lewis et al.*, 1990]. On the other hand, the nature of the light field itself can be used to infer the concentrations and characteristics of dissolved and particulate water constituents [*Dierssen et al.*, 2006; *Gordon and Morel*, 1983; *Gordon et al.*, 2009; *Lee et al.*, 2011; *Siegel et al.*, 2005] as well as the boundary conditions such as the sea surface wave field [*Bréon and Henriot*, 2006] or the sea bottom [e.g. *Lee et al.*, 1999].

Light propagation in the water is an involved process. When photons propagate onto the ocean surface, some are reflected and the rest transmited across the (variable) water surface [*Austin*, 1974]. In the ocean interior, the course of photons is further altered by

scattering and absorption. Assuming a horizontally stratified water body and ignoring fluorescent emission and Raman scattering and other sources, this radiative transfer process can be described as

$$\cos\theta \frac{\mathrm{d}L(\theta,\varphi,z,t)}{\mathrm{d}z} = -c(z)L(\theta,\varphi,z,t) + L^*(\theta,\varphi,z,t) \tag{1.1}$$

The term on the left is the rate of change of radiance along the optical path specified by the viewing direction (θ,φ), water depth z (m) and time t (s). The terms on the right refer to two opposite processes: the first term represents the loss due to light attenuation (sum of scattering and absorption), and the second term is the gain due to light scattering into the direction (θ,φ) from photons that were previously travelling in a different direction. Given the directional radiance distribution at each depth, one can obtain complete information of the light field distribution, and theoretically, and with the assumption above regarding sources, all inherent optical properties like scattering and absorption [*Jerlov*, 1976]. Prediction of the radiance distribution is however a very difficult problem due to the variability in the ocean-water boundary conditions and the generally unknown optical properties of water constituents such as the scattering and absorption coefficients.

Knowledge of the underwater light field has been largely developed in the context of biological studies. Irradiance is the most characterized descriptor of the light field [e.g. *Siegel and Dickey*, 1987; *Siegel et al.*, 1995]. It is the angular integration of the radiance field and is convenient to measure in the ocean [*Dickey and Chang*, 2001; *Duntley et al.*, 1955; *Smith et al.*, 1984; *Waters et al.*, 1990]. Irradiance is of significance in the photosynthetic rate of marine phytoplankton as it represents the primary energy source [*Jassby and Platt*, 1976; *Morel*, 1991; *Steemann Nielsen*, 1974]. Variability of the irradiance attenuation coefficient, the rate at which plane irradiance diminishes with

depth, relates to key biogeochemical properties of the ocean [*Morel and Maritorena*, 2001].

Since the launch of the Coastal Zone Color Scanner (CZCS) in 1978, tremendous progress has been achieved in understanding the light field. The upwelling nadir radiance is the key parameter in this line of research [*Gordon and Morel*, 1983]. With the upwelling nadir radiance or the reflectance (the ratio of upwelling nadir radiance to the downwelling irradiance at the sea surface), ocean color remote sensing allows for diagnoses of water constituents and biological processes over synoptic scales [*Behrenfeld and Falkowski*, 1997; *Lee et al.*, 2011; *Muller-Karger et al.*, 2005; *Platt and Sathyendranath*, 1988; *Siegel et al.*, 2005].

In the last few decades, various instruments have been developed to observe the underwater light field and optical properties of the water. Spectral irradiance, as well as absorption, scattering and beam attenuation sensors have now become standard equipment on hydrographic profiling packages [*Maffione*, 2001; *Moore et al.*, 2009; *Twardowski et al.*, 2005]. The field has experienced an evolution of the ad hoc methodology for sensing the radiance field from the primitive tools like the screened photometer [*Johnson and Liljequist*, 1938], to the rigid Gershun-tube sensors like the Scripps radiance photometer [*Duntley et al.*, 1955], and to a more recent development of the radiance camera system [*Antoine et al.*, 2013; *Voss*, 1989b; *Voss and Chapin*, 2005]. These existing radiance cameras have provided the most complete and quantitative radiance distribution data so far, but the downwelling field is generally depleted within the first tens of meters in the water column, where the radiance varies in an intra-scene dynamic range of over a million and the integration time required for the upwelling field

obviates the resolution of many processes of interest. We have a gap in our experience base of measuring the radiance distribution in the very layers of the water that contribute to the remotely sensed upwelling radiance and that contribute most strongly to the photosynthetic primary production. Very few radiance data sets exist today [*Tyler*, 1958; *Lundgren and Højerslev*, 1971; *Voss and Chapin*, 2005].

The relative weakness of radiance instrumentation has generally limited our ability to approach a more complete understanding of the ocean processes and phenomena involving interaction with light. Models are put forward stressing the variation in the upwelling radiance field and the effect of this variation on interpretation of measurements of the ocean reflectance made above the water [e.g. *Mobley*, 1989; *Morel and Gentili*, 1993; *Voss et al.*, 2007; *Zaneveld et al.*, 2001a]. The often used Q factor, the ratio of upwelling irradiance to upwelling nadir radiance, for example, has been shown to be much more variable than previously thought [*Hirata et al.*, 2009; *Morel et al.*, 2002; *Zibordi and Berthon*, 2001]. However, validation of all these models has to be put on hold until all critical properties including the radiance distribution can be accurately obtained. Many sophisticated optical models involve parameters such as the radiance distribution, which cannot be used in an operational sense. A typical example is the Gershun's law which relates the radiance distribution to the total absorption coefficient [*Gershun*, 1939]. Some elegant models regarding the radiance distribution and water inherent optical properties have rarely been tested [e.g. *Kirk*, 1981; *Preisendorfer*, 1958a].

The radiance field in surface ocean water is a three-dimensional problem. The dynamic nature of the surface results in a dynamic light field; the surface waves cause fluctuations in the radiance on time scales as short as milliseconds to seconds [*Darecki et*

al., 2011; *Sabbah and Shashar*, 2006]. Fluctuations in radiance propagate into its integrated counterpart, the irradiance field [*Fraser et al.*, 1980; *Gernez and Antoine*, 2009; *Snyder and Dera*, 1970; *Stramska and Dickey*, 1998] and to the average cosine. The dynamic characteristics of the light field cause great uncertainties in the in-situ radiometric measurements, which further impact the subsequent biogeochemical estimations. In actuality, the characteristic rapid variability of the underwater radiance field may contain a wealth of information about the air-water boundary conditions, analogous to the reflected radiance field above the water surface [*Cox and Munk*, 1954]. It is well known that the dynamic light field is of importance to the dynamics of photosynthesis [*Greene and Gerard*, 1990; *Stramski et al.*, 1993; *Walsh and Legendre*, 1983]. Sensory biologists also have great interest in the adaptation of marine animals to the dynamic radiance field as well [e.g. *Mäthger*, 2003; *Sabbah et al.*, 2012]. It is important and yet a great challenge to develop techniques for sampling the full radiance distribution at the appropriate time and space scales and examining the resulting data so as to unravel the highly convoluted environmental condition [*Ackleson*, 2001].

The objectives of the thesis are henceforth to exploit new tools for measuring the full radiance distribution and to gain insights into the propagation and distribution of the radiance field within the near-surface ocean waters. Specifically, four problems are to be addressed: 1) development of a new instrument for measuring the high dynamic range and highly variable radiance field; 2) interpretation of the mean light field and derivation of other optical properties in the ocean; 3) evaluation of wave disturbance of the radiance distribution; and 4) reexamination of the irradiance field fluctuations as induced by surface waves.

1.2. Outline of Thesis

The thesis is composed of seven chapters. A general introduction to the research motivation is given in the current chapter. Chapter 2 describes and provides a background on ocean optics. The principal content of this thesis is presented in the subsequent four chapters:

Chapter 3 introduces an instrument for measuring the full radiance distribution in the ocean interior. The general instrumentation, detailed calibration, and a characterization of the system are described. Validity of the camera system is demonstrated by comparison of the radiance measurements with other classical oceanographic radiometers.

Chapter 4 examines the mean structure of the downwelling and upwelling radiance fields as a function of water depth in diverse water bodies. It is shown that the measured nonpolarized radiance field therefore provides all the pertinent information to derive not only all of the apparent optical properties, but the inherent optical properties such as the absorption coefficient as well.

Chapter 5 addresses the problem of the wave disturbance of the radiance distribution. Observations from the radiance camera fixed at shallow depths of ocean surface water provide highly resolved radiance distribution measurements. The radiance fluctuations in every direction as well as the irradiance and average cosine fluctuations in terms of their probability distributions, periodicities and amplitudes of variation are characterized. The underlying mechanisms for the light field fluctuations are further discussed.

Chapter 6 deals with the rapid variations of the irradiance field as observed in the irradiance depth profiles in the upper water column. An effort is made to extract the

statistics pertinent to the light field fluctuations from the vertical profiles of irradiance measured under clear skies. Two parameters including the dominant frequency and the coefficient of variation of irradiance fluctuations along the water column are identified from the variance spectrum and characterized. Data validation is further provided. Mechanisms contributing to the observed variations and the observational uncertainties are discussed.

A general conclusion is given in Chapter 7, which summarizes the results and discusses the potential and future developments.

The copyright information is enclosed in Appendix A.

Chapter 2. Theoretical Bases

2.1. Radiance and Irradiance

Hydrologic optics is the quantitative study of the interaction of the ultraviolet, visible and near infrared radiation with the natural waters of the earth such as its seas and lakes [*Preisendorfer*, 1976]. As the fundamental radiometric quantity in hydrologic optics, an operational definition of the unpolarized spectral radiance [*Mobley*, 1994] is

$$L(z,\hat{\xi},\lambda)=\frac{\Delta Q}{\Delta t\Delta A\Delta\Omega\Delta\lambda} \qquad (\mu\text{W cm}^{-2}\ \text{sr}^{-1}\ \text{nm}^{-1}) \tag{2.1}$$

where ΔQ (J) is the radiant energy of photons travelling in a set of directions of solid angle $\Delta\Omega$ (steradian) centred on direction $\hat{\xi}$, in a wavelength interval $\Delta\lambda$ centred on wavelength λ (nm), and falling onto a surface of area ΔA (cm^2) perpendicular to $\hat{\xi}$, within time interval Δt (second). The direction $\hat{\xi}$ can be described by the zenith angle θ and azimuth angle φ in the spherical coordinate system (Figure 2.1). The solid angle Ω is an extension of a two dimensional angle measurement, and is given as the set of directions defining the patch A as

$$\Omega=\frac{A}{r^2} \quad \text{(unit: sr)} \tag{2.2}$$

where r represents the radius of the sphere. In the conceptual limit, the solid angle $d\Omega$ can be described as

$$d\Omega=\sin\theta\, d\theta\, d\varphi \tag{2.3}$$

Integration of Eq. (2.3) over the full spherical space yields 4π.

The spectral downwelling plane irradiance E_d (μWcm^{-2}nm^{-1}) is the radiant power of total photons travelling downward onto a level surface, defined as the integration of directional radiance in the corresponding hemisphere

$$E_d(z,\lambda) = \int_{\hat{\xi}\in\Xi_d} L(z,\hat{\xi},\lambda)\cos\theta \mathrm{d}\Omega(\hat{\xi}) \quad (\mu\mathrm{W}^{-2}\mathrm{cm}^{-2}\mathrm{nm}^{-1}) \tag{2.4}$$

where Ξ_d denotes the upper hemisphere of directions with $0° \le \theta \le 90°$. The upwelling plane irradiance E_u refers to the similar integration of radiance but in the lower hemisphere of directions, i.e. $90° \le \theta \le 180°$. The difference between the downwelling and upwelling plane irradiance is called the net (downwelling) irradiance,

$$E_{net}(z,\lambda) = E_d(z,\lambda) - E_u(z,\lambda) \quad (\mu\mathrm{W}^{-2}\mathrm{cm}^{-2}\mathrm{nm}^{-1}) \tag{2.5}$$

The spectral downwelling (unweighted) scalar irradiance, E_{od}, is related to the radiance in every direction within the upper hemisphere

$$E_{od}(z,\lambda) = \int_{\Xi_d} L(z,\theta,\varphi,\lambda)\mathrm{d}\Omega \quad (\mu\mathrm{W}^{-2}\mathrm{cm}^{-2}\mathrm{nm}^{-1}) \tag{2.6}$$

The total scalar irradiance is the integration of light incoming from every direction in the space,

$$E_o(z,\lambda) = E_{od}(z,\lambda) + E_{ou}(z,\lambda) \quad (\mu\mathrm{W}^{-2}\mathrm{cm}^{-2}\mathrm{nm}^{-1}) \tag{2.7}$$

where E_{ou} is the upwelling scalar irradiance integrated from the upwelling radiance in directions within the lower hemisphere, $90° \le \theta \le 180°$.

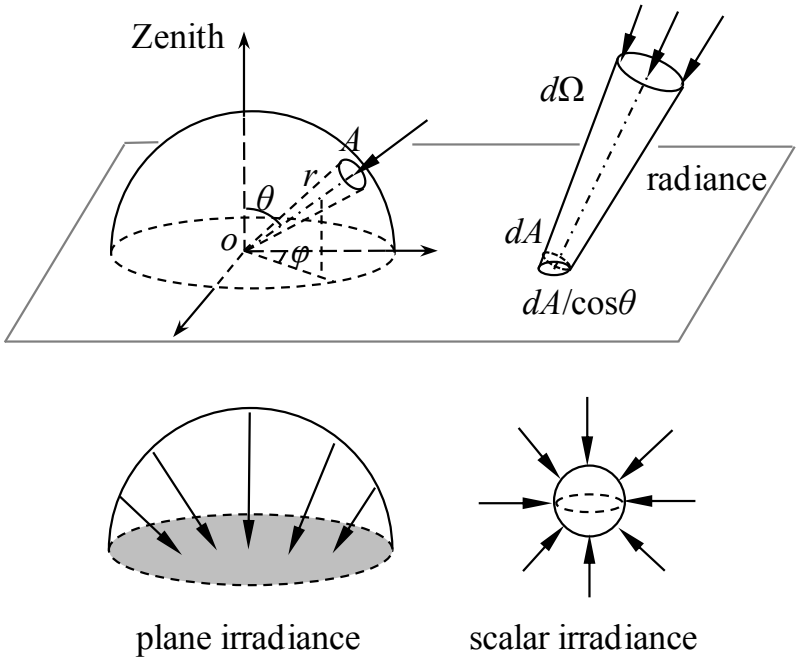

Figure 2.1 Measuring geometry of the radiometric quantities. In the spherical coordinate system, the zenith has a polar angle $\theta = 0°$ and the nadir corresponds to the direction with polar angle $\theta = 180°$. The azimuth angle is represented by its relative position to the sun, varying from 0° to 360° clockwise. The directional radiance refers to the total flux falling within a conic region of the solid angle $d\Omega$ and onto the cross-section dA.

2.2. Apparent Optical Properties

The apparent optical properties (AOPs) are those radiometrically determined scattering- and absorbing-induced quantities which generally depend on the geometrical structure of the light field (i.e. the radiance distribution), but which have enough regular features and enough stability to be entitled to "optical property" [*Preisendorfer*, 1976]. The commonly used AOPs in hydrologic optics include the distribution functions (average cosine and Q factor), R functions and K functions. All of the AOPs can be expressed as a function of the radiance.

The average cosine describes the angular distribution of radiance at a given point and is considered as the average of the cosine of the zenith angle of all photons at a particular point [*Kirk*, 1994; *Mobley*, 1994],

$$\bar{\mu}(z,\lambda) = \frac{E_d(z,\lambda) - E_u(z,\lambda)}{E_o(z,\lambda)} \quad \text{(dimensionless)} \tag{2.8}$$

For the downward travelling light, the average cosine is defined as

$$\bar{\mu}_d(z,\lambda) = \frac{E_d(z,\lambda)}{E_{od}(z,\lambda)} \tag{2.9}$$

For the upwelling light, the average cosine is defined as

$$\bar{\mu}_u(z,\lambda) = \frac{E_u(z,\lambda)}{E_{ou}(z,\lambda)} \tag{2.10}$$

In ocean color remote sensing, one often used parameter is the ratio of the upwelling plane irradiance to the upwelling nadir radiance at right below the sea surface (denoted as 0^-), which is known as the Q factor (sr)

$$Q(\lambda) = \frac{E_u(0^-,\lambda)}{L_u(0^-,\lambda)} \quad \text{(sr)} \tag{2.11}$$

For an isotropic light field, the Q factor is constant π.

The first R function is called the irradiance reflectance, which is defined as the ratio of upwelling to downwelling plane irradiance

$$R(z,\lambda) = \frac{E_u(z,\lambda)}{E_d(z,\lambda)} \tag{2.12}$$

In ocean color remote sensing, the spectral remote-sensing reflectance R_{rs} (sr^{-1}) is often used

$$R_{rs}(\lambda,\theta,\varphi) = \frac{L(0^+,\theta,\varphi,\lambda)}{E_d(0^+,\lambda)} \qquad (\mathrm{sr}^{-1}) \tag{2.13}$$

where the notation 0^+ indicates that the quantities are measured right above the sea surface.

In the upper water column of the ocean free of boundary effects (sea waves and sea bottom), various radiances and irradiances decrease approximately exponentially with the water depth [*Jerlov*, 1976; *Kirk*, 1994; *Siegel and Dickey*, 1987]. The rate of change of these quantities is called the diffuse attenuation coefficient, K (m^{-1}). For example, the diffuse attenuation coefficient for the downwelling plane irradiance can be defined as

$$K_d(z,\lambda) = -\frac{1}{E_d(z,\lambda)}\frac{\mathrm{d}E_d(z,\lambda)}{\mathrm{d}z} \qquad (\mathrm{m}^{-1}) \tag{2.14}$$

Analogously, we define K_u, K_{net}, K_o, and K_L as the diffuse attenuation coefficients for the upwelling plane irradiance, net irradiance, total scalar irradiance and directional radiance, respectively.

2.3. Inherent Optical Properties

The optical properties such as absorption coefficient a (m^{-1}), scattering coefficient b (m^{-1}), beam attenuation coefficient c (m^{-1}), and scattering phase function $\tilde{\beta}$ (dimensionless) are collectively called the inherent optical properties (IOPs), which are only dependent on the water constituents and not on the geometric structure of the various light fields [*Preisendorfer*, 1976].

Figure 2.2 schematically shows the measuring geometry for the IOPs. A narrow collimated beam of monochromatic light with radiant power Φ_i (μW) is incident onto one side of a tiny volume of water (ΔV). Some part of the radiant power Φ_a, is absorbed by the water and some power Φ_s is scattered along direction ψ relative to the original direction. The rest of the radiant power Φ_t is successfully transmitted through the volume and propagates along the original course. The absorption coefficient is then measured as the absorbance per unit distance

$$a = \lim_{\Delta r \to 0} \frac{\Phi_a / \Phi_i}{\Delta r} \qquad (m^{-1}) \tag{2.15}$$

The attenuation coefficient c is measured as the transmittance over Δr

$$c = \lim_{\Delta r \to 0} \frac{\Phi_t / \Phi_i}{\Delta r} \qquad (m^{-1}) \tag{2.16}$$

The total scattering coefficient b is the difference between c and a, $b = c - a$. The scattered light Φ_s only represents the fraction of the total scattered light along the direction ψ within the solid angle $\Delta\Omega$ which is centered at ψ. The angular distribution of the scatterance within $\Delta\Omega$ is the volume scattering function $\beta(\psi)$

$$\beta(\psi) = \lim_{\Delta r \to 0} \lim_{x \to \Delta\Omega} \frac{\Phi_s / \Phi_i}{\Delta r \Delta\Omega} \qquad (\mathrm{m}^{-1}\mathrm{sr}^{-1}) \tag{2.17}$$

where the scattering angle ψ varies between 0° and 180°.

The scattering phase function $\tilde{\beta}$ is the ratio of the volume scattering function to the scattering coefficient. The ratio of the scattering to attenuation coefficients is called the single scattering albedo, ω_o

$$\omega_o = \frac{b}{c} \quad \text{(dimensionless)} \tag{2.18}$$

The scattering coefficient can be further divided into the forward scattering ($0° \le \psi \le 90°$) and the backward scattering ($90° \le \psi \le 180°$), which can be integrated from the scattering phase function, respectively, according to

$$b_f = 2\pi b \int_0^{\pi/2} \tilde{\beta} \qquad \mathrm{d}\psi \tag{2.19}$$

and

$$b_b = 2\pi b \int_{\pi/2}^{\pi} \tilde{\beta} \qquad \mathrm{d}\psi \tag{2.20}$$

We note that all IOPs, just like AOPs, are all spectrally dependent.

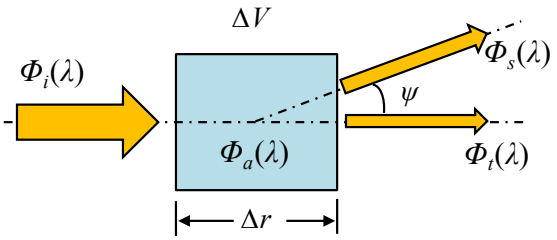

Figure 2.2 Measuring geometry of the inherent optical properties.

2.4. Radiative Transfer

The behavior of photons travelling within the water is regulated by the optical properties of the water components. They are either absorbed, and their energy dissipated as heat, or scattered away, which only changes the photon's traveling path. Some photons coming from other directions may be as well scattered into the original path. The radiative transfer equation (RTE) is formulated to describe the manner in which the radiance varies with the optical path distance along any specified direction. Assuming a horizontally stratified water body with optical properties constant everywhere at a given depth z, with a constant input of monochromatic radiation at the sea surface, the radiance along a path $\hat{\xi}$ is predicted as [*Mobley*, 1994]

$$\cos\theta \frac{\mathrm{d}L(z,\hat{\xi},\lambda)}{\mathrm{d}z} = -c(z,\lambda)L(z,\hat{\xi},\lambda) + \omega_o(z,\lambda)\int_{\Xi} L(z,\hat{\xi}',\lambda)\tilde{\beta}(z,\hat{\xi}',\hat{\xi},\lambda)\mathrm{d}\Omega(\hat{\xi}') + S^*(z,\hat{\xi},\lambda) \qquad (2.21)$$

The first term at right-hand side of Eq. (2.21) represents the diminution as a result of absorption and scattering out of the light beam as the photons travel. The second term describes the augmentation resulting from the scattering into the direction of propagation from photons traveling along other paths $\hat{\xi}'$, i.e. the elastic scattering, in which the energy of the incident photon is conserved and only its direction is changed. The last term in above equation is the contribution of Raman scattering or fluorescence, often known as the source term. The source term could be relatively small in turbid water but may become significant in clear oceanic water [see *Morel*, 1974].

The radiative transfer equation is the basis to investigate the relationships between the IOPs and AOPs. One important derivation is the divergence law for irradiance. It is derived from the direct integration of the radiative transfer equation over all directions [*Mobley*, 1994]. Briefly, integration of the left-hand side of the RTE equation (2.21) yields

$$\begin{aligned}\int_{\Xi}\cos\theta\frac{\mathrm{d}L(z,\hat{\xi},\lambda)}{\mathrm{d}z}\mathrm{d}\Omega(\hat{\xi}) &= \frac{\mathrm{d}}{\mathrm{d}z}\int_{\Xi}L(z,\hat{\xi},\lambda)\cos\theta\mathrm{d}\Omega(\hat{\xi}) \\ &= \frac{\mathrm{d}}{\mathrm{d}z}\left[E_d(z,\lambda)-E_u(z,\lambda)\right]\end{aligned} \tag{2.22}$$

The attenuation term in Eq. (2.21) gives

$$-\int_{\Xi}c(z,\lambda)L(z,\hat{\xi},\lambda)\mathrm{d}\Omega(\hat{\xi}) = -c(z,\lambda)E_o(z,\lambda) \tag{2.23}$$

The elastic scattering term can be transformed to

$$\begin{aligned}&\int_{\Xi}\left[w_o(z,\lambda)\int_{\Xi}L(z,\hat{\xi}',\lambda)\tilde{\beta}(z,\hat{\xi}'\cdot\hat{\xi},\lambda)\mathrm{d}\Omega(\hat{\xi}')\right]\mathrm{d}\Omega(\hat{\xi}) \\ &= \int_{\Xi}L(z,\hat{\xi}',\lambda)\left[\int_{\Xi}w_o(z,\lambda)\tilde{\beta}(z,\hat{\xi}'\cdot\hat{\xi},\lambda)\mathrm{d}\Omega(\hat{\xi})\right]\mathrm{d}\Omega(\hat{\xi}') \\ &= b(z,\lambda)\int_{\Xi}L(z,\hat{\xi}',\lambda)\mathrm{d}\Omega(\hat{\xi}') \\ &= b(z,\lambda)E_o(z,\lambda)\end{aligned} \tag{2.24}$$

Integration of the source term may be parameterized as

$$\int_{\Xi}S^*(z,\hat{\xi},\lambda)\mathrm{d}\Omega(\hat{\xi}) = E^S \tag{2.25}$$

Substituting the integrated terms into the original RTE Eq. (2.21) yields

$$\frac{\mathrm{d}}{\mathrm{d}z}\left[E_d(z,\lambda)-E_u(z,\lambda)\right] = -a(z,\lambda)E_o(z,\lambda)+E^S \tag{2.26}$$

If there were no source term, the above equation can be further reduced to

$$\frac{\mathrm{d}}{\mathrm{d}z}\left[E_d(z,\lambda)-E_u(z,\lambda)\right]=-a(z,\lambda)E_o(z,\lambda) \tag{2.27}$$

We emphasize that the plane-parallel assumption (PPA) has been assumed in the above derivations, where the physical variables depend on one space coordinate only: the vertical depth. Eq. (2.27) may be reformulated in a three-dimensional domain

$$\nabla\bullet \qquad (x,y,z,\lambda)E_0(x,y,z,\lambda) \tag{2.28}$$

According to Eq. (2.27) or Eq. (2.28), the absorption coefficient can be derived from light field measurements. Since Eq. (2.28) was first derived by *Gershun* [1939], it is often called Gershun's law.

It is common to treat the natural water body as horizontally uniform layers in current radiative transfer calculations and optical modeling of the ocean [e.g. *Boynton and Gordon*, 2002; *Gordon and Boynton*, 1998; *McCormick*, 2004; *Mobley and Preisendorfer*, 1988; *Plass and Kattawar*, 1969]. The plane-parallel theory assumes the horizontal gradients in the net irradiance in Eq. (2.28) are very small compared with the vertical gradients [*Zaneveld et al.*, 2001b]

$$\begin{aligned}\frac{\partial E_{net}(x,y,z)}{\partial x} &\ll \frac{\partial E_{net}(x,y,z)}{\partial z}\\ \frac{\partial E_{net}(x,y,z)}{\partial y} &\ll \frac{\partial E_{net}(x,y,z)}{\partial z}\end{aligned} \tag{2.29}$$

The plane-parallel theory may hold when the ocean surface is viewed from a distance, such as a satellite, and the extent of horizontal scales viewed is sufficiently large (at least 70 m for calm sea conditions and larger than 1 km when large swells exist) [*Zaneveld et al.*, 2001b].

For large-scale synoptic observations with satellite sensors, the optical characteristics of wind-ruffled water surfaces are mainly determined by the wave slopes, which are

ascribed to both gravity waves and capillary waves. The wave slope distribution can be determined from the glitter pattern of the reflected sun (Figure 2.3a). The classical glitter measurements [*Cox and Munk*, 1956] show that the upwind and crosswind slopes vary in a random manner, being independently and normally distributed with zero mean and variances

$$\begin{aligned} \sigma_c^2 &= 0.003 + 1.92 \times 10^{-3} U_{10} \pm 0.002 \\ \sigma_u^2 &= 0.000 + 3.16 \times 10^{-3} U_{10} \pm 0.004 \end{aligned} \tag{2.30}$$

where σ_c^2 and σ_u^2 are the crosswind and upwind/downwind components of the mean square slopes, and U_{10} is the wind speed (m s^{-1}) measured at 10 m above the sea surface. Incorporation of sea slope statistics into plane-parallel radiative transfer models yields an ensemble-average light field [e.g. *Mobley and Preisendorfer*, 1988; *Plass and Kattawar*, 1969].

Wave disturbance of the light field is likely significant as far as *in situ* experimental studies in surface waters are concerned. Field optical radiometry often senses the light field in a relatively small horizontal extent, when the geometry of sea waves impacts the temporal and spatial distribution of the underwater light field [*Snyder and Dera*, 1970]. A photograph of the wind waves is given in Figure 2.3b, which was taken in a small wind-wave tunnel (15 cm wide), at fetch 6 m, with a free stream wind velocity of 6 m s^{-1} [*Ebuchi et al.*, 1987, Figure 11].

It is of interest to be able to measure the underwater radiance field under such wavy sea surface and to quantify the influences of such fluctuations of the sea-surface on the resulting underwater radiance field.

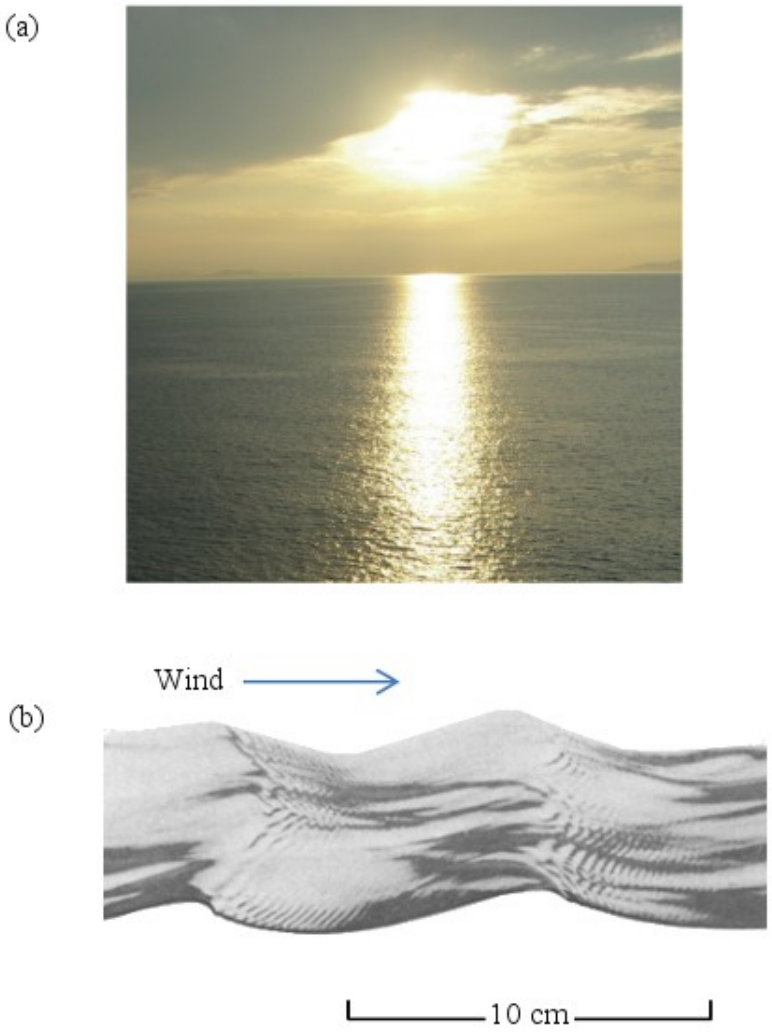

Figure 2.3 Example photographs of sea waves. (a) Elongated low sun glitter reaching to the horizon (ocean) [*Lynch et al.*, 2011, Figure 2]. (b) A close-up photograph of the wind waves and the water surface structures [*Ebuchi et al.*, 1987, Figure 11].

Chapter 3. A High Dynamic Range Camera for Measuring the Full Nonpolarized Radiance Distribution in Near-surface Sea Water

3.1. Introduction

Radiance is the total radiant energy of photons per unit solid angle per unit surface area and per unit time [*Jerlov*, 1976]. The angular distribution of radiance in the upper water column is of fundamental importance for many problems met in aquatic sciences and accurately measuring the underwater radiance distribution has been one of the critical tasks in hydrologic optics [*Jerlov and Fukuda*, 1960; *Johnson and Liljequist*, 1938; *Lundgren and Højerslev*, 1971; *Pettersson*, 1938; *Sasaki et al.*, 1958; *Tyler*, 1958; *Voss and Zibordi*, 1989; *Voss et al.*, 2007; *Whitney*, 1941].

One of the earliest instruments for in-water radiance was a screened photometer designed by *Johnson and Liljequist* [1938] and *Pettersson* [1938]. This apparatus consisted of an irradiance meter (with a horizontal receiving surface) and a movable black plate. The plate was suspended above the irradiance sensor, and moved along the

---

* This chapter is an amended version of a published paper: Wei, J., R. Van Dommelen, M. R. Lewis, S. McLean, and K. J. Voss (2012); A new instrument for measuring the high dynamic range radiance distribution in near-surface sea water; *Optics Express*, *20*(24), 27024-27038. The contribution of the author includes contributions to camera design, characterization and calibration in the lab, data processing and analyses, and writing of this manuscript. The co-authors contributed to conceptual design, instrument design and development, hardware buildup, data processing and manuscript corrections.

vertical to yield a sum of azimuthally averaged radiances over different zenith intervals. This instrument was later modified to measure radiance over azimuthal directions replacing the overhead screen with a cylindrical screen so that the photometer received light from a narrow cone (half angle $\alpha_{1/2} = 7.5°$). The primitive instruments provided the earliest picture of the depth evolution of the underwater radiance field [also see *Whitney*, 1941].

A convenient design for a radiance sensor is the Gershun-tube [*Gershun*, 1939] radiometer. One early development in this approach was the Scripps radiance photometer [*Duntley et al.*, 1955]. For in-water operation, the radiometer was suspended by a cable and rotated so that it measured the radiance in different directions [*Jerlov and Fukuda*, 1960; *Lundgren and Højerslev*, 1971; *Sasaki et al.*, 1958; *Tyler*, 1958]. Spatial scanning with coarse resolutions around 10-30° along both the zenith and azimuthal directions required about 10-20 minutes at only one depth [e.g. *Tyler*, 1958], limiting the conditions under which it could be deployed. As well, the large field of view (FOV), $\alpha_{1/2} = 3.5°$-$7.5°$, results in averaging out many fine features pertinent to the radiance field. A similar instrument has also been deployed by *Aas and Højerslev* [1999].

The first development of a radiance camera system to instantaneously image the radiance distribution underwater was completed by *Smith, Austin and Tyler* [1970]. Their instrument relied on a fisheye lens and a film camera. The fisheye lens projected the incoming hemispheric light onto the image plane (see Figure 3.1), and the radiance was related to the density of the exposed film negative [*Smith*, 1974]. A more advanced radiance camera was built by *Voss and Chapin* [2005], based on solid state cameras (e.g. CCD). The CCD radiance camera measures the full radiance distribution with very low

noise and very high spatial resolution (~0.5°); it has provided the most complete data for the upwelling radiance distribution in various waters [*Voss and Chapin*, 2005; *Voss et al.*, 2007; *Voss et al.*, 2003]. However, as the CCD radiance cameras are based on linear system transfer functions (mathematical functions relating the response of a system to the input), they are prone to saturation when viewing scenes including extremely intense radiation like direct focused sunlight in the near-surface water, or lacking sensitivity when viewing unfocused and/or non-direct sky radiance in the same image. These cameras lacked the dynamic range required for viewing the effects of near-surface wave-focused downwelling radiance.

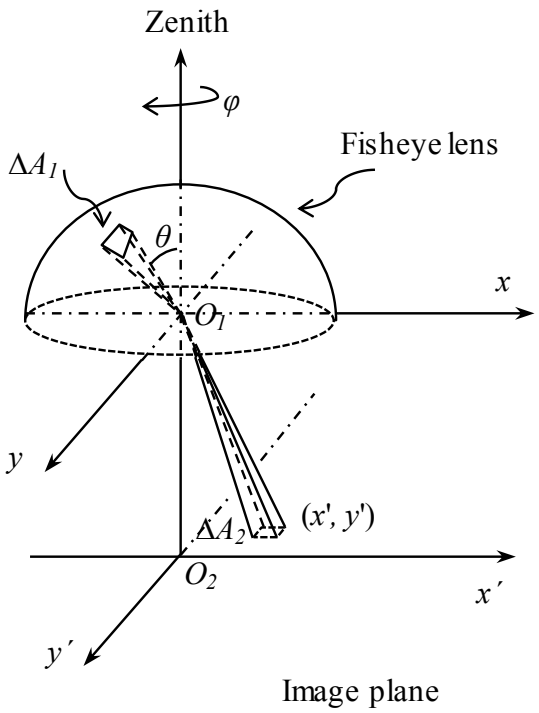

Figure 3.1 Schematic drawing of the geometry for measuring directional radiance. Camera with fisheye lens maps the radiance $L(\theta,\varphi)$ in one hemispheric space onto the image plane, which is defined by pixel (x',y').

The radiance distribution in the sea is a consequence of the refraction of the radiance distribution from the sun and sky at the air-sea interface and the subsequent light absorption and scattering within the water itself. These phenomena result in an anisotropic in-water radiance field. For example, the downwelling radiance distribution varies over a dynamic range of more than 6 decades [*Tyler*, 1958], while the dynamic range for the spherical upwelling light rarely exceeds two decades [*Voss and Chapin*, 2005]. Furthermore, in open ocean areas, the sea surface is rarely a static environment and this results in fluctuations of less than one second in the underwater light field [*Darecki et al.*, 2011]. An ideal instrument to measure the in-water radiance distribution

requires a radiometer that is calibrated against international standards over a wide dynamic range, and that can take synoptic observations at high frequency with fine angular resolution.

The objective of this study is to describe a new high dynamic range (HDR) solid-state camera system (RadCam), capable of measuring the full radiance field at high temporal and angular frequency in the upper ocean.

3.2. RadCam Instrument

The design of the RadCam radiometer is inspired by previous underwater fisheye radiance cameras [*Smith et al.*, 1970; *Voss and Zibordi*, 1989; *Voss and Chapin*, 2005], with the above-mentioned challenges in mind. A high dynamic range sensor was used as the imaging element.

3.2.1. Fisheye Lens and Input Optics

The optical components of the radiance camera are composed of a fisheye lens (Coastal Optics Systems®) and a customized optical relay system. The layout of the optical system is shown in Figure 3.2. The fisheye lens covers a hemispherical field of view and follows an equidistant projection (radius on image is linearly proportional to field angle θ). The assembled underwater camera employs a BK-7 glass dome (not shown in the figure) to protect the lens. The relay uses a pair of achromatic doublet lenses to achieve the desired image magnification. A triplet field lens is also employed to increase the FOV of the relay and to reduce the lens system roll-off. A spectral bandpass filter is inserted

into the relay system, so that the optical system projects light centered at 555 nm, with 20 nm bandwidth on the detector array. The optical system projects a circular image of a hemisphere of the radiance distribution. All optical components except the dome and array are antireflection coated.

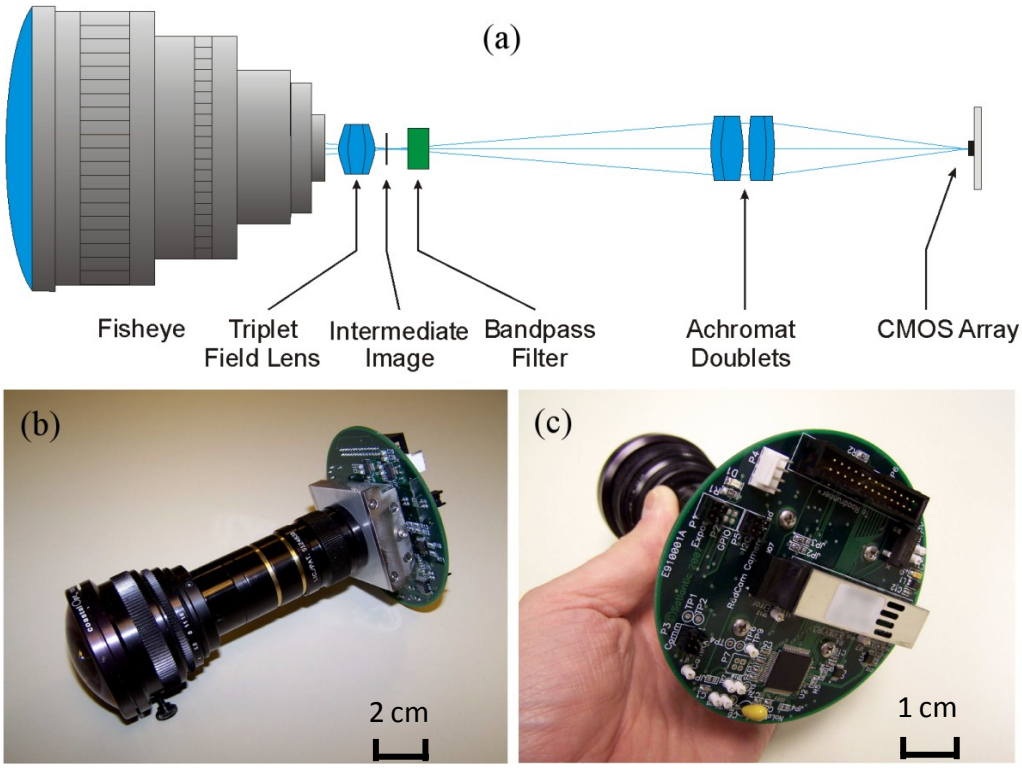

Figure 3.2 Camera components and configuration. (a) Schematic of the optical system including the fisheye lens and optical relay. (b) Picture of the assembled optical system with the CMOS camera. (c) Picture of the customized camera-head electronics. The silver rectangular box in (c) is the fiber transceiver.

3.2.2. CMOS Imager

The imager used in our camera is a Micron® Complementary Metal Oxide Semiconductor (CMOS) image sensor. The CMOS technology allows the incorporation of on-chip electronics with the photo-detectors. The on-chip electronics allow increased functionality, for example, to obtain the high intra-scene dynamic range using a variety of response functions. The CMOS array is also inherently non-blooming, which avoids the artifact created by charges flowing to neighboring pixels when exposed to high light intensities, and capable of measuring radiant flux up to 9 orders of magnitude, which is critical for imaging the full radiance field including the sun. Some shortcomings are also apparent, however, such as increased noise and reduced uniformity; some of which can be minimized and accounted for by a complete radiometric calibration and characterization. The CMOS array has 752×480 pixels, each 6×6 μm in size. It employs a global shutter that prevents smearing of the dynamic scenes. A frame grabber is used to digitize the video signal into a 2D rectangular array of 10-bit integer values.

The circular image captured by the array is represented by a total of $\pi D^2/4$ pixels, where D is the diameter of the captured image described in number of pixels. Since the fisheye lens follows the equidistant projection, the pixel position in the image plane is proportional to the direction of the incident ray [*Miyamoto*, 1964]

$$r = \alpha\theta \tag{3.1}$$

where r is the radial distance of the active pixel from the image center (also in number of pixels), α is a constant, and θ is the field angle of incoming ray relative to the principal optical axis. These geometrical parameters are determined empirically during the initial characterization.

The electronics on the chip surrounding the array are sensitive to the incident light and produce a spatially nonuniform pixel gain. The chip incorporates a shield to reduce this effect, but during calibration we needed to illuminate the whole array with high intensity light and this shield was not sufficient. We overcame this problem by attaching a black metal shield directly on top of the chip. This reduces the effective array size to less than 420 pixels in diameter.

The acquisition speed of the system is greater than 40 frames per second (fps) for the shortest exposure time that we use. However, the recorded frame rate is limited by the logging computer system (particularly the custom software) to 15 frames per second (fps). At the lowest light levels, for example when measuring the radiance distribution at depth under a cloudy sky, the system is limited to about 1 fps due to an extended exposure time.

3.2.3. Camera System

Three types of radiance distribution camera systems have been built with the same configuration of the optical systems and imagers: a water-column profiling camera, a sky camera, and a self-logging camera. All three camera systems are assembled in aluminum housings. They all include a tilt/compass sensor (Advanced Orientation Systems Inc) to record the pitch, roll and yaw of the instrument.

The profiler in Figure 3.3a is equipped with dual cameras, one facing upward and the other one viewing downward. The two cameras together image the full radiance field. This system is designed for free-fall operation [*Waters et al.*, 1990] with two fins installed on the upper end of the housing, symmetric about the camera. Conductivity , temperature and depth sensors (CTD) (Falmouth Scientific Inc) and multichannel OCR-

504I/R radiometers (Satlantic LP) are set up on each fin with the upward viewing instrument measuring the downwelling planar irradiance and the downward looking instrument measuring the nadir radiance. Both are operated at four wavelengths (412, 443, 511 and 555 nm). The instrument buoyancy is adjusted by adding/removing foam from inside the fins so that the package descends at a speed of less than 0.5 m s^{-1}. With this arrangement, the instrument tilt is generally less than 5° except in the first few meters below the sea surface. The fins also help the instrument package trail away from the deployment vessel before data collection, to reduce the shadowing effect of the vessel. A guard cage is used to protect the upwelling camera window. The overall height for the profiler is 115 cm, the width is 46 cm (distance including the two fins), and the weight in air is 26 kg. The depth rating is 200 m. The profiling system communicates with the on-deck computer running logging software via a fiber optic cable. The ancillary data including the downwelling irradiance and upwelling nadir radiance from the OCR-504I/R sensor, CTD data and tilt and heading information are synchronized with the image data and saved in a separate file.

The sky camera in Figure 3.3b images the full sky radiance distribution including the sun without the glass dome. It communicates with the same control computer via a separate fiber optic cable. This camera system is 36 cm in height and 11 cm in diameter, and weights 3.8 kg in air. This camera is designed to work simultaneously with the profiling camera, to provide information on the incident light above the sea surface, but can also operate independently.

The third camera system is a self-logging camera specifically designed for operations on various underwater platforms such as an autonomous underwater vehicle (AUV). An

on-board custom computer controls the camera and internally logs the radiance data where it is downloaded when the system is recovered. This system is 26 cm in height and 23 cm in diameter and the weight in air is about 9.6 kg. The logging camera can also be mounted in a cage as shown in Figure 3.3c and lowered into the water from a boom to make depth profiles in one hemisphere.

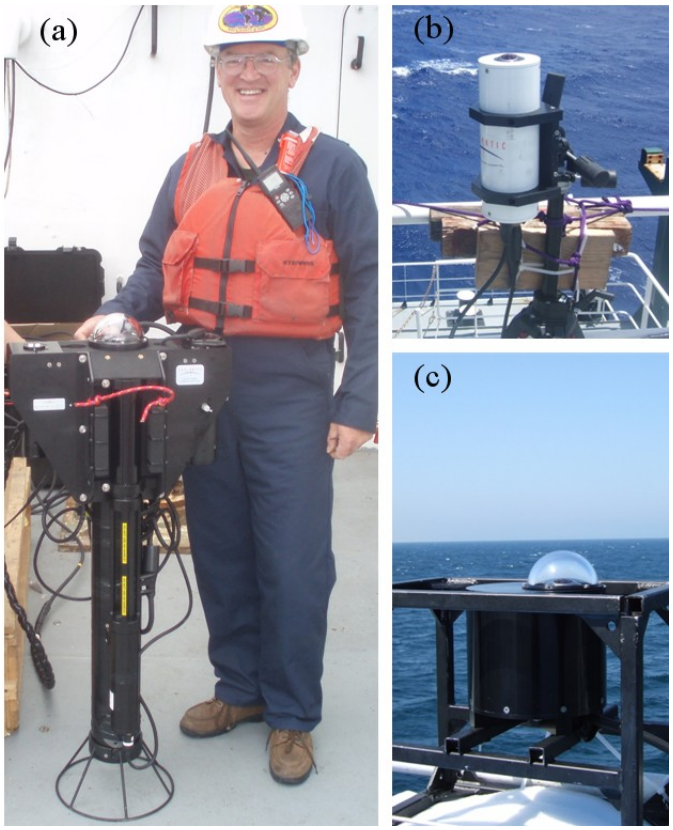

Figure 3.3 Radiance distribution camera systems. (a) Profiling camera. The downwelling camera is on the top and the upwelling camera is at the bottom; OCR-504I/R radiometers are installed on the left wing and the CTD is on the right wing. (b) Sky camera mounted on a tripod. (c) Self-logging underwater radiance camera mounted in a cage. Image courtesy of Satlantic LP.

3.3. Radiometric Calibration and Characterization

The general form of the calibration equation describes the spectral radiance $L(\lambda)$ as a function of the output signal [*Nicodemus*, 1978]

$$L(\lambda) = h\left[s(\lambda)\right] \tag{3.2}$$

where s is the output signal per unit of input, in this case, the radiance. The wavelength dependency will be dropped since only one wavelength is considered in our cameras. The absolute radiance responsivity function $h(s)$ is an essential parameter to be determined in calibrations.

A complete calibration of the sensor requires corrections in several domains be applied to the measurement equation. The system is designed to be nonlinear over the dynamic range of response. Characterizing the nonuniformity of pixel-to-pixel response for the array detector is also critical in the spatial (angular) domain. The modulation transfer function (MTF) of the optical system is another parameter to be determined to make necessary corrections in the system level calibration.

3.3.1. High Dynamic Range (HDR) Response Functions

The first step in the calibration is to define the shape of high dynamic range response functions over the 2^{10} gray scales in the range of camera counts from 0 to 1023. Different combinations of register settings including the shutter widths, vertical blanking and potential barrier limits, etc., were tested with the bare imager (no optical system) illuminated by a power-stabilized 1000 W FEL halogen lamp (Optronic Labs LLC) (Figure 3.4a). The incoming light flux was varied by adding neutral density (ND) filters of various transmittance between the imager and the lamp. The incident radiation was

also changed by moving the imager relative to the light source. For higher incident radiance, a helium-neon laser beam was used to illuminate pixels on the array (Figure 3.4b). Many register settings were tested during the experimentation. For each exposure setting, the pixel responds to the incident light in a characteristic way, and based on this observation, we defined three sets of register setting (Table 3.1). Figure 3.5a presents three example response curves representative of distinctive exposure settings, where the output signals *s* are described as a function of the irradiance. The three response curves cover relatively low, moderate, and high radiance ranges and partly overlap. The moderate and high exposures each permit intra-scene contrasts of more than 6 decades (60 dB) and the total range is over 9 decades (90 dB). Exposure time ranges between 0.02-1.0 seconds. Each curve can be divided into several segments and each segment is fit to a simple model; the goodness of fit is usually better than 0.99. The high-exposure response curve is designed to measure the most intense light, such as the radiance distribution in near-surface sea water, and the exposure time is approximately 0.02 seconds in this case.

Table 3.1 Register settings for three exposures.

Registers	Hi-exposure	Mid-	Low-exposure
Vertical blanking	0x044D	0x044D	0x002D
Shutter width 1	0x01BB	0x01BB	0x01BB
Shutter width 2	0x01D9	0x01D9	0x01D9
Shutter width control	0x0064	0x0264	0x0164
Total shutter width	0x0020	0x0500	0x7FFF
Pixel operation mode	0x0051	0x0051	0x0011
V1	0x001F	0x001F	0x001D
V2	0x001A	0x001A	0x0018
V3	0x0012	0x0012	0x0015
V4	0x001B	0x000A	0x0004
AEG/AGC enable	0x0000	0x0000	0x0000

The pixels on the CMOS array have their own amplifiers. Each active pixel behaves as an independent radiance sensor, receiving photons, converting them to a voltage and transferring the information directly to the output. To account for the potential nonuniformity of the pixel array, a flat-field correction was performed. This calibration first measures the response of each pixel to the same light source (FEL lamp) (Figure 3.4a). The second step involves the use of a helium-neon laser as the light source, with the CMOS imager being mounted on a precision three-axis translation stage (Figure 3.4 b). The array was scanned across the laser beam, to build up a composite calibration image. Neutral density filters were also used in this step to vary the incident light flux. We note that the intensity profile of the laser beam is actually a Gaussian shape. A single pixel on the array was therefore used to scan across the laser beam and determine the beam radius (in pixels) that is suitably uniform to be used for calibration.

(a) The array receives light from the FEL lamp

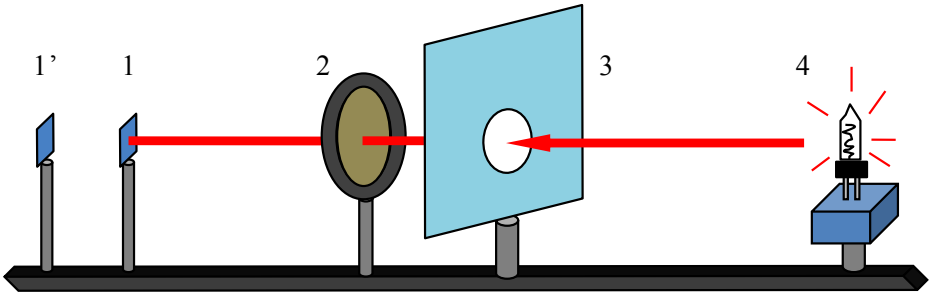

(b) The array receives light from the laser

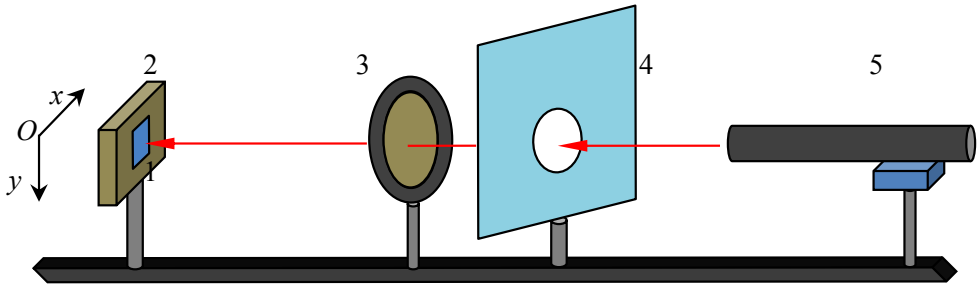

Figure 3.4 Experimental setup for the pixel response determination. (a)The pixel array receives the light emitting from the 1000 W FEL lamp. The major experimental parts consist of 1) the bare imager, 2) neutral density filter, 3) light baffle, and 4) FEL lamp; the imager may be repositioned along the rail to change its distance to the light source. 1') shows the same bare imager mounted at a distance different from that indicated by 1). (b) The pixel array is scanned with the laser beam. The experimental components include 1) the bare imager, 2) translation stage, 3) neutral density filter, 4) light baffle, and 5) helium-neon laser.

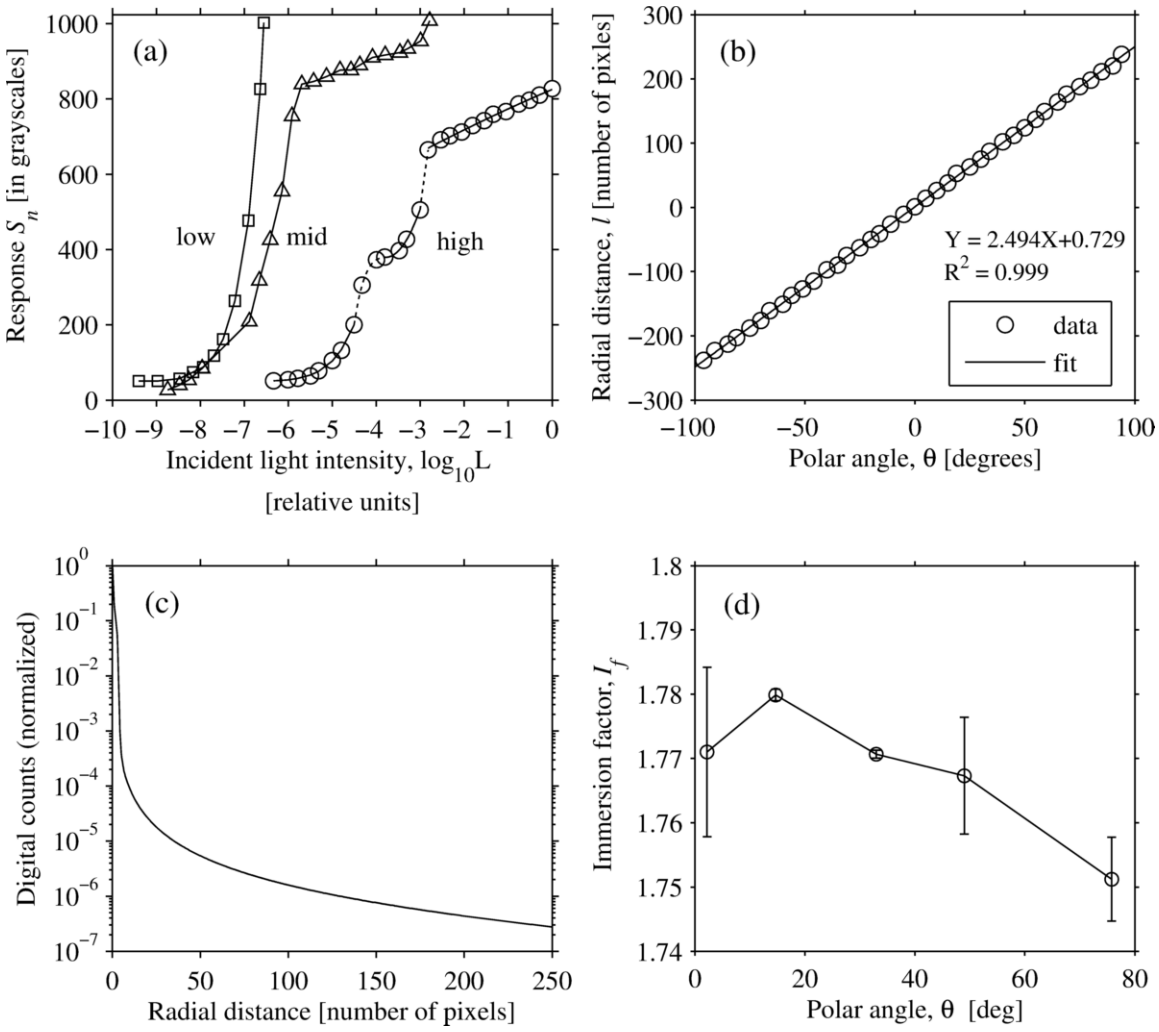

Figure 3.5 Calibration data of the radiance camera. (a) HDR response functions. Example model fitting to the high-radiance exposure data has been demonstrated used solid and dotted lines alternatively. (b) Geometric calibration data. (c) Measured point spread function. (d) Measured immersion factor (of self-logging camera) with viewing directions.

3.3.2. Absolute Responsivity

The purpose of this system calibration is to convert the response curve to absolute responsivity for every pixel. For this calibration, the imager and the optics were assembled together. For the underwater camera, the glass dome was installed as well. Figure 3.6 shows the experimental setup for the system calibration. The integrating sphere was set up on the optical bench and illuminated by an arc lamp, and the light exiting the sphere was used as the light source. The camera was mounted onto a rotation stage with its lens toward the sphere's exit and imaged the light exiting the sphere. The camera's lens was scanned over the full 180° as the camera was rotated. The end result is a bright circular image covering the entire hemispheric field of view. The absolute radiance of the light exiting the sphere was measured with a transfer radiometer (HyperOCR, Satlantic LP), which was calibrated with a NIST-traceable radiometric calibration transfer standard. This image of absolute radiance is then used to scale the relative response curves to an absolute responsivity.

This experimental setup is necessary to achieve the intense radiance required. The typical method for radiance calibration using an FEL lamp and a planar Lambertian plaque [e.g. *Voss and Zibordi*, 1989] does not provide a source with sufficient energy. The roll-off of the optical system describes the attenuation along the entire optical path from the outer glass dome to the detector as well as the change in solid angle. The roll-off in our system is less than 8% at $\theta = 90°$ due to the use of a field lens at the output of the fisheye lens. The system level calibration performed by rotating the camera has calibrated every pixel and in theory has removed the system roll-off.

The beam spreading effect requires the point spread function (PSF) and is described below. This system level calibration is carried out for the other two exposure settings by inserting neutral density filters between the integrating sphere and the arc lamp.

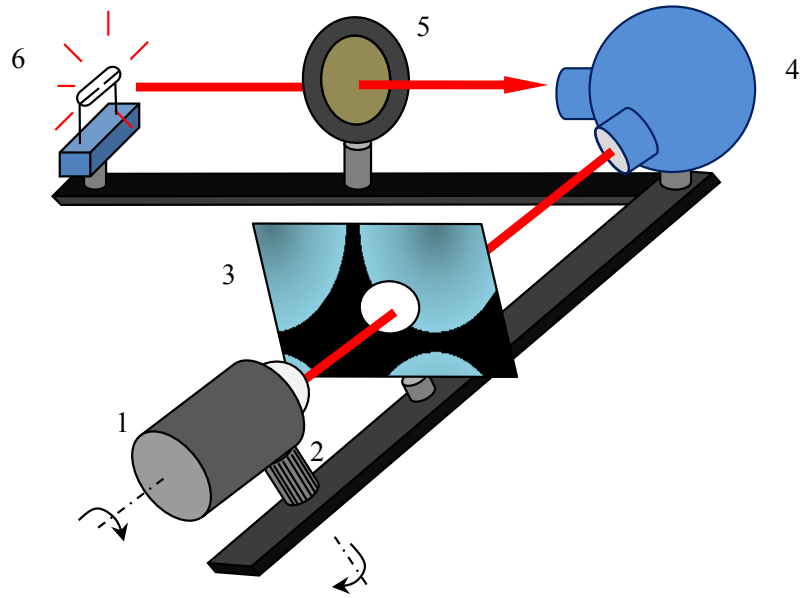

Figure 3.6 Experimental setup for the system calibration. The major components are composed of 1) the assembled camera, 2) rotation stage, 3) light baffle, 4) integrating sphere, 5) neutral density filter, and 6) arc lamp. The camera can be rotated horizontally with the programmable rotation stage, and rolled manually about the principal axis.

3.3.3. Geometric Projection

In order to determine the geometric projection of this optical system, we performed the experiments as described below. The camera was first mounted onto the rotation stage as in previous experiments. A green light-emitting diode (LED) was positioned at the same height and at a distance of at least 1 m from the camera lens. This arrangement allows the LED emitted light to be completely imaged by a single pixel. The scanning was done at 1° steps throughout the hemispheric field of view of the camera and then with the camera head rolled about its principal axis. Two such scanning lines can be used to define the location for the image center and the diameter D with simple trigonometry.

As implied in Eq. (3.1), the radial distance r of the active pixel from the image center (x, y) conforms to the linear relationship, $r = D\theta/\pi$, where θ is the polar direction of the incident ray sensed by the active pixel. This test indicates that the geometrical projection is linear (Figure 3.5b), with an $R^2 = 0.999$. For a system with an image diameter $D = 400$ pixels, the measured radiance field has the nominal spatial resolution of ~0.45° along the radial direction (i.e. the zenith direction in the spherical coordinate). The azimuthal resolution is related to the pixel's radial distance. For example, the resolution is about $\Delta\varphi = 10°$ at polar angle 5° and changes to $\Delta\varphi = 1°$ at polar position 45°. The solid angle $d\Omega(i,j)$ subtended by a pixel area (dA) also varies with its radial distance in the image plane [also see *Voss and Chapin*, 2005] and can be represented as

$$d\Omega(i,j) = \frac{\pi}{l_{ij} D} \cdot \sin\left(\frac{\pi l_{ij}}{D}\right) \cdot dA \tag{3.3}$$

According to Eq. (3.3), the solid angle $d\Omega(i,j)$ for each active pixel is slightly dependent on the radial distance. For example, the $d\Omega$ is about 6.46×10^{-5} sr near the zenith and decreases to 4.77×10^{-5} sr at zenith angle $\theta = 85°$.

3.3.4. Point Spread Function

In the optical system, a portion of the signal of each pixel also likely comes from surrounding areas due to the scattering effect between the optical elements, which will affect the accuracy of the radiometric measurement [e.g. *Du and Voss*, 2004]. The point spread function (PSF) of the optical system was measured to account for this effect, which is also known as the beam spread function (BSF). A beam expander was used to expand the helium-neon laser beam so that the entire camera's dome was illuminated by the incoming light. The imager array was set to operate in linear mode and multiple exposures used to achieve the complete dynamic range needed to measure the PSF out to the largest radii. The point spread function is assumed to be spatially-invariant and is derived by binning and averaging the camera response (in digital counts) as a function of the radial distance from the image center (x, y). The PSF varies up to 6 orders of magnitude in digital counts, from the center of a point source to the 200th pixel (Figure 3.5c). The measured point spread function was applied by an iterative image deblurring approach using the Lucy-Richardson algorithm. This method was chosen because the radiant energy can be conserved during the calculation, which is critical for the absolute radiometric output.

3.3.5. Immersion Factor

When immersed in the sea water, the ambient light enters the camera through the water-glass-air path. The index of refraction of sea water (n_w = 1.34) will impact the absolute responsivity determined in air [e.g. *Zibordi et al.*, 2004b]; an immersion factor that accounts for the change in absolute responsivity must be determined. The experimental procedure of *Voss and Chapin* [2005] was followed. Our experiments show that the self-logging camera has a mean immersion factor of 1.78. An example measurement of the immersion factor is given in Figure 3.5d, where the percent variation is less than 2%. For the profiling camera, the immersion factor was only measured at viewing directions from 69° to 76°, because its body is too long (more than 1 m) to do a similar experiment in a regular tank. Based on our tests, the profiling camera has an average immersion factor of 1.94±0.04 for the downwelling camera and 1.92±0.02 for the upwelling camera.

3.3.6. Polarization Sensitivity

The responsivity of the camera system may be affected by the state of polarization of the light field, and this is important because the natural light field is linearly polarized [e.g. *Waterman*, 1954]. We have tested the polarization sensitivity of the camera by measuring the radiance of a polarized light source. A polarizing filter was inserted between the exit of the sphere and the camera lens in an experimental setup similar to Figure 3.6. The camera imaged the linearly polarized light radiation. The orientation of polarization, θ_p, was varied by rotating the filter, and the polarized light source was also imaged from different camera viewing angles. From the sampled images, the radiance over a total of 7×7 pixels around the center of the bright spot are considered. Our experiment shows that

this electro-optical camera system has a polarization sensitivity of less than 4%, which is calculated as the degree of linear polarization (DOLP), DOLP = (L_{max}-L_{min})/(L_{max}+L_{min}), where L_{max} and L_{min} refer to the maximum and minimum radiance, respectively, over a total rotation of 180 degrees.

3.4. Measurement Uncertainty

The complete calibration equation is obtained by incorporating the calibration parameters

$$L = h[s] \cdot I_f \cdot \rho^{-1} \cdot \overline{\mathrm{PSF}} \tag{3.4}$$

where the absolute responsivity f is fitted to polynomial functions of the sensor response s, $h[s] = P_1 s^n + P_2 s^{n-1} + \ldots + P_{n+1}$, with polynomial coefficients P_n; I_f is the immersion factor; ρ is the spectral response function (SRF); and $\overline{\mathrm{PSF}}$ is a mathematical operator rather than a scalar, representing the introduction of the PSF correction. Uncertainties of the calibration parameters propagate to the radiance measurements.

Uncertainty of $h[s]$ is subject to the quantization noise and errors of the raw sensor response. The temporal variation of the absolute measurement was estimated by continuously imaging the integrating sphere illuminated by the arc lamp as shown in Figure 3.6. The relative uncertainty is calculated as the ratio of the standard deviation of the mean to the mean of the radiance measurements, which has been shown generally to be less than 2% (Table 3.2). The estimate for temporal uncertainty includes contributions from variations in the light source.

The description of the response function $h[s]$ may be incomplete since the available experimental data for establishing the nonlinear fitting models are limited by the

experimental setups. This uncertainty due to insufficient formulation remains unknown, however. One consequence is that the model fittings applied to every pixel will generate residual variations in the flat field, causing the reproducibility variation. We have tested the residual spatial uniformity of radiance measurements over the field of view of the camera in a setup similar to Figure 3.6. The camera was rotated horizontally in steps of approximately 10° from 2° to 86°, while the output light from the integrating sphere was imaged. Groups of 7×7 pixels were averaged for each field angle. The results are listed in Table 3.3, which shows a measurement uncertainty generally less than 10%. This pixel-to-pixel variation is mainly contributed by the variation of the absolute responsivity in the spatial domain.

Dark current can be a major source of noise in CMOS imagers [*Porter et al.*, 2008]. The dark current was accounted for in our radiometric experiments when determining the response curves, for which we related the input radiance to a digital number or count (corresponding to output) that included the dark current value. These calibrations were carried out at room temperature 20±1 °C. When deployed in the sea water, the camera chip temperature will vary over a certain range and we cannot quantify exactly this type of dark current error for now. The sea surface water temperature is less than 32 °C [*Deser et al.*, 2010]; this fact might have resulted in low but unknown dark current errors.

Table 3.2 Uncertainty of the sensor responsivity as determined from the radiance measurements (555 nm).

	Mean radiance ($\mu Wcm^{-2}sr^{-1}nm^{-1}$)	Relative uncertainty (%)
High-exposure	211	0.05-3.11
	89	0.06-1.13
	51	0.24-0.50
	6.9	0.56-1.11
Mid-exposure	5.9	0.84-1.20
	3.47	1.10-1.30
	1.70	0.85-1.56
	0.73	1.09-1.59
	0.31	0.07-0.30
	0.07	0.45-0.98
	0.03	0.48-1.05

Table 3.3 Large scale uniformity determined as the relative uncertainty of radiance measurements (555 nm) in ten different field angles from 2° to 86°.

Mean radiance ($\mu Wcm^{-2}sr^{-1}nm^{-1}$)	Exposure settings	Relative uncertainty (%)
300	high	9.7
180	high	10.2
50	high	0.8
6.5	high	1.4
9.5	mid	3.3
8.6	mid	4.1
4.4	mid	6.0
2.2	mid	3.2
1.1	mid	2.1
0.30	mid	2.9
0.07	mid	13.7
0.04	mid	5.2

The SRF has a full width at half maximum (FWHM) of λ_{FWHM} = 19.8 nm with a standard deviation 0.06 nm. To estimate the uncertainty, we assumed a single line-source falling within nominal band of 546 nm to 564nm. The mean and variance were calculated for this band from the spectral response data. In this case, the relative uncertainty u_{SRF} is 1.4%.

The combined measurement uncertainty involves all contributing components [e.g. *Wyatt et al.*, 1998]. Such an estimate is difficult to make considering the effect of the point spread function. As an alternative, we look at the absolute difference by comparing the camera measurements in the lab to a reference radiometer. The reference sensor is the same HyperOCR radiometer used in the system calibration, which has been calibrated with a NIST-traceable lamp and is accurate to within about 2% [*Voss et al.*, 2010]. In this experiment, the input optics of the two sensors were positioned at a very short distance (~8 cm) to the exit port of the sphere, so that the entire FOV of the instrument was illuminated by the light exiting the sphere. The experiment was carried out with the input radiance spanning 5 orders of magnitude. The lowest radiance we observed was on the order of 0.01 $\mu Wcm^{-2}sr^{-1}nm^{-1}$, and the highest radiance was slightly less than 300 $\mu Wcm^{-2}sr^{-1}nm^{-1}$. The symmetric mean absolute percentage difference (SMAPD) was calculated for these data pairs,

$$SMAPD = \frac{1}{N}\sum_{t=1}^{N}\frac{|A_t - F_t|}{(|A_t| + |F_t|)/2} \times 100\% \tag{3.5}$$

where A_t refers to the values from the reference radiometer and F_t is the RadCam measurement averaged over 20×20 pixels. The radiance measurements at around 100 $\mu Wcm^{-2}sr^{-1}nm^{-1}$ (high exposure, denoted as closed circles in Figure 3.7) gave a difference of 28.7%. The middle-exposure radiance data (denoted as open squares in Figure 3.7) had

a difference of 13.0%. Under low-exposure settings (denoted by closed squares in Figure 3.7), the SMAPD for the radiance measurements was 9.7%. The overall difference is about 16.3%.

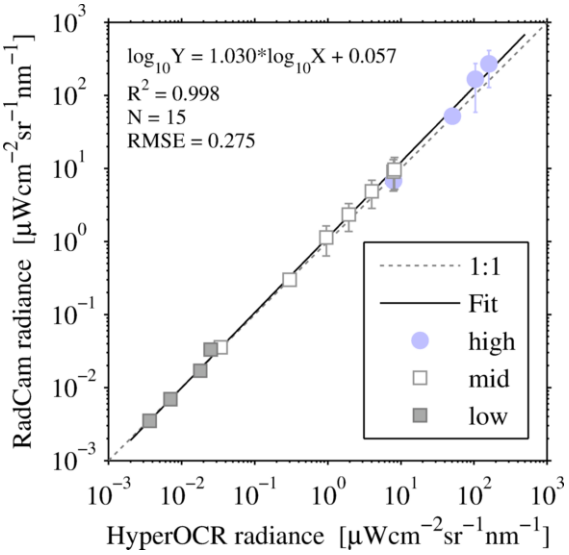

Figure 3.7 Comparison of the radiance measurements (555 nm).The data were collected from the RadCam and the HyperOCR radiometer in the lab. Three exposure settings are tested for different intensities of light source. Note that all these data points have been used for the regression analysis.

The high-exposure experiment described above has merely considered the radiance at the lower end of the corresponding response curve (in this case, less than 300 $\mu Wcm^{-2}sr^{-1}nm^{-1}$). The radiance from the solar disk however could reach as high as 10^6-10^7 $\mu Wcm^{-2}sr^{-1}nm^{-1}$. An experiment was devised to check the camera calibrations using the highest radiance in nature. First, the camera was set up to image the sun directly; and then the measurement was repeated but through neutral density filters of various optical densities. The radiance distribution measured with the ND filters can be corrected for the applied optical density, d, using the fractional transmittance $L_{ND}/L_0 = 10^{-d}$, where L_{ND} and L_0 refer to the radiance measured with and without the filters, respectively. If the responsivity were correctly determined in our aforementioned calibrations, the radiance measurements with and without the ND filters (when accounting for the ND filter) of the sunlight and skylight in this experiment would give the same results. The indirect measurements are compared with the direct measurements in Figure 3.8. Only those pixels less than 5° away from the sun are considered. Two data sets, one from the direct measurements of sky radiance and another from the in-direct measurements of the sky radiance using the ND filters, are fit to a linear function with a coefficient of determination ~0.9 and a slope very close to one.

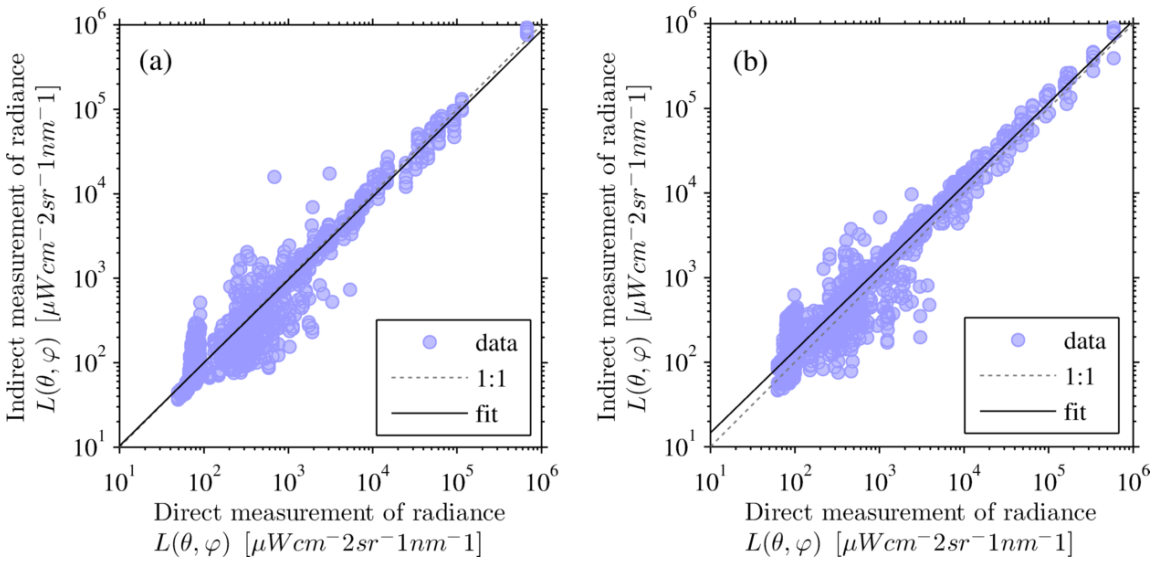

Figure 3.8 Measured radiance distribution (555 nm) under sunny sky. (a) Solar zenith angle θ_s = 40°; data measured on June 11, 2010, 13:36 UTC; the linear fitting equation is $\log_{10}Y = 0.983 \times \log_{10}X + 0.032$, $R^2 = 0.916$, N = 2205. (b) Solar zenith angle θ_s = 23.5°; data measured on June 11, 2010, 15:28 UTC; the linear fitting equation is $\log_{10}Y = 0.974 \times \log_{10}X + 0.190$, $R^2 = 0.927$, N = 1785.

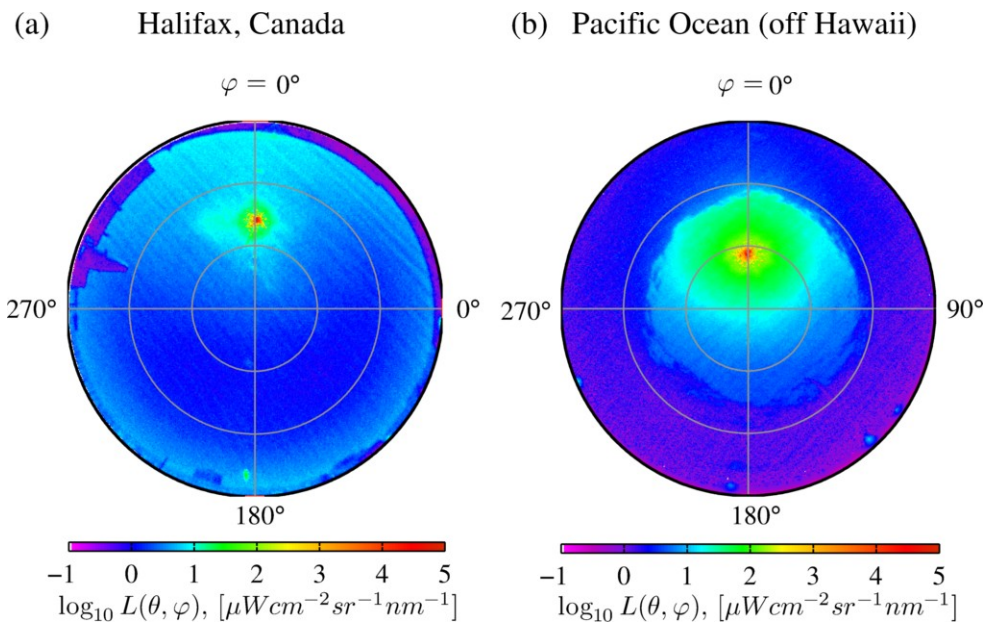

Figure 3.9 Example measurements of radiance distribution (555 nm). (a) The radiance distribution of the whole sky including the sun. The image was shot in Halifax, Nova Scotia, on June 11, 2011, at 13:15 pm UTC (10:15 am local time), at an altitude 65 m above the sea surface. (b) The radiance distribution within sea surface water. The data were collected in the Pacific Ocean (155°58′ W, 19°15′ N) on August 27, 2009, 20:40 UTC, when the sky was sunny and the sea waves were less than 0.5 m high; the sampling water depth was at 5 m (wind speed 1.5 m/s).

3.5. Data Examples

3.5.1. Radiance of the Sky

Figure 3.9a presents an image of the clear sky by the sky camera. The data were captured on the rooftop in Halifax, Canada (44°38.27' N, 63°35.63'W), on June 11, 2010. The image shown has been calibrated to engineering units of $\mu Wcm^{-2}sr^{-1}nm^{-1}$. The azimuthal position is described relative to the sun. The solar zenith angle (SZA) θ_s is 40°. The center of the image corresponds to the zenith (θ = 0°), and the zenith angle linearly increases from the center to the periphery (θ = 90°). The image includes some parts of surrounding obstacles, which are just above the camera horizon. The beam spread effect has been corrected with the measured point spread function. The first feature shown in this figure is that the sky radiance distribution is symmetric about the principal plane (the vertical plane containing the sun; in this case, the azimuth directions in both φ = 0° and φ = 180°). The minimum radiance is in the region opposite to the sun, somewhere between 0° and 90° in zenith angle.

One inherent artifact with the full sky measurement is the lens flare induced by internal reflections and scattering in the lens and relay optics when imaging the sun. As shown in Figure 3.9a, the lens flare is most evident as several artifacts (bright dots) along the solar principal plane. The effect of lens flare is also significant in the circumsolar region (from 0.5° to ~10° relative to the sun). Reflection can also be seen at the bottom of the image.

Another potential problem, which is common for digital cameras, arises when the apparent image size of the object is larger than a pixel, such as the solar disk in our case. As a consequence, the image of the sun usually falls onto several neighboring pixels

instead of just one pixel. Since there is always one maximal pixel value, we take the maximal pixel as the radiance of the solar disk.

During this sky experiment, a second data set was also measured by a sky scanning spectral radiometer (CE-318A, CIMEL Inc, France), which is operated by the Aerosol Robotic Network (AERONET). The CE-318A measures the sky radiance in the almucantar and the principal plane at a few wavelengths but does not operate at 555 nm. We first retrieved four channels of sky radiance at 440, 500, 675 and 870 nm, and then interpolated the sky radiance at 555 nm following an exponential model for the spectral radiance distribution, $\ln L(\lambda_1) = a_1 \times \ln L(\lambda_2) + a_2$, where a_1 and a_2 are the slope and intercept determined from a least squares fit. This product provides an opportunity for an indirect calibration crosscheck for the RadCam measurements. In Figure 3.10, the radiances measured by CE-318A are compared to the RadCam per-pixel measurements. We note that CE-318A has a field of view of 0.6° (half angle) and a solid angle of 3.445×10^{-4} sr, while our camera's mean solid angle subtended by a pixel is much smaller, $\Omega = 6.25\times10^{-5}$ sr. Besides, the CE-318A radiometer and RadCam are calibrated with different standards, and the spectral interpolation at 555 nm for CIMEL measurements introduces errors as well. Therefore, differences between the RadCam and CIMEL would be expected without preference to the source of error. Figure 3.10 also compares the RadCam data to modeled sky radiance, which was derived from an empirical sky radiance model [*Harrison and Coombes*, 1988], the same one as used by Hydrolight® software [*Mobley and Sundman*, 2008]. The important environment parameters (e.g. the air pressure, total ozone, horizontal visibility, wind speed, relative humidity and precipitable water content) were monitored and retrieved from local stations including the

AERONET station in Halifax. All aforementioned problems (including the apparent image size of the sun and model uncertainty) are responsible for the observed discrepancies among the RadCam data, CIMEL data and the modeled radiance.

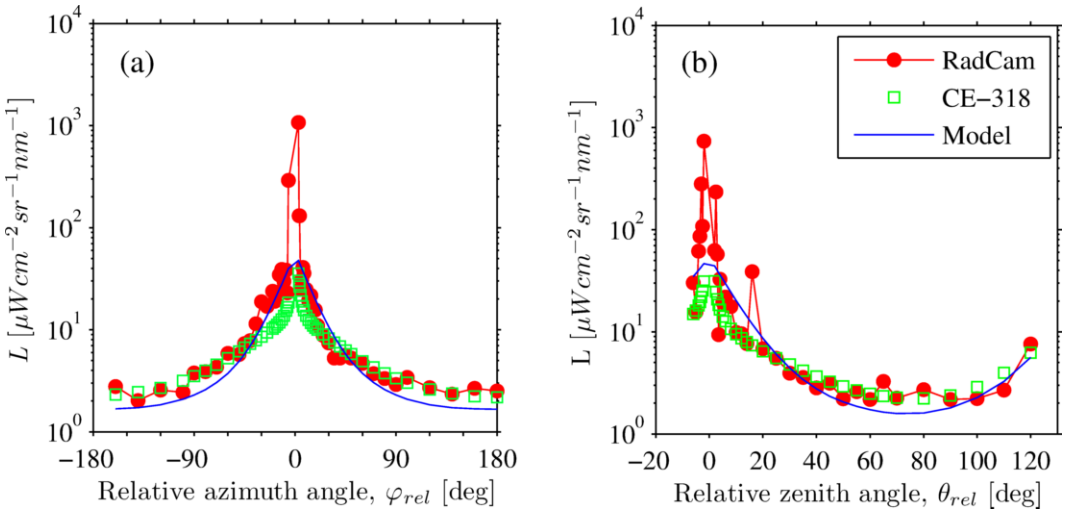

Figure 3.10 Comparison of sky radiance measurements (555 nm). (a) Sky radiance in the almucantar. The data were collected at 13:15 UTC, June 11, 2010, on campus of Dalhousie University, Halifax, with an elevation of 65 m above the sea level. (b) Sky radiance in the principal plane. The data were measured at 13:24 UTC, June 11, 2010, at the same location.

3.5.2. Radiance in the Sea

Example measurements for the full underwater radiance distribution are given in Figure 3.9b. The data were collected in the Pacific Ocean off Hawaii (155°58′ W, 19°15′ N) on August 27, 2009, 20:40 UTC, when the sky was sunny and the sea waves were less than 0.5 m high, the sampling water depth was at 5 m, and the wind speed was 1.5 m/s. For the underwater radiance image, we rarely observe obvious lens flare as in above-water

applications. That is because the radiance of the refracted sun underwater is often attenuated relative to the sun in the air, and the sea water has a larger refractive index than the air which further reduces the multiple surface reflections between lenses. For this example, the downwelling radiance field spans up to 6 orders of magnitude. The upwelling radiance field varies within one order of magnitude (figure not shown).

The OCR-504I/R measures the irradiance and radiance at wavelengths identical to the RadCam. Figure 3.11a illustrates the downwelling irradiance profiles measured by two sensors in the Pacific Ocean under sunny skies and shows no significant differences due to wave-induced fluctuations. The fluctuations seen in Figure 3.11b are mainly caused by the sensor inclinations. The camera measurements are quantitatively compared with OCR-504 data in Figure 3.11c and Figure 3.11d, each of which is composed of more than 2000 data points collected in different locations in the Pacific Ocean. The observed difference is less than measured in the lab: SMAPDs are 14.2% for the irradiance data and 6.2% for the upwelling radiances. We note that these estimated differences have included both the measurement uncertainty and the variance of the spatial distribution of the light field as influenced by sea waves. As the wave focusing effect is more significant for the downwelling light than the upwelling light distribution [e.g. *Stramska and Dickey*, 1998], the real measurement uncertainties for downwelling plane irradiance and upwelling nadir radiance are likely smaller than 14% and 6% respectively.

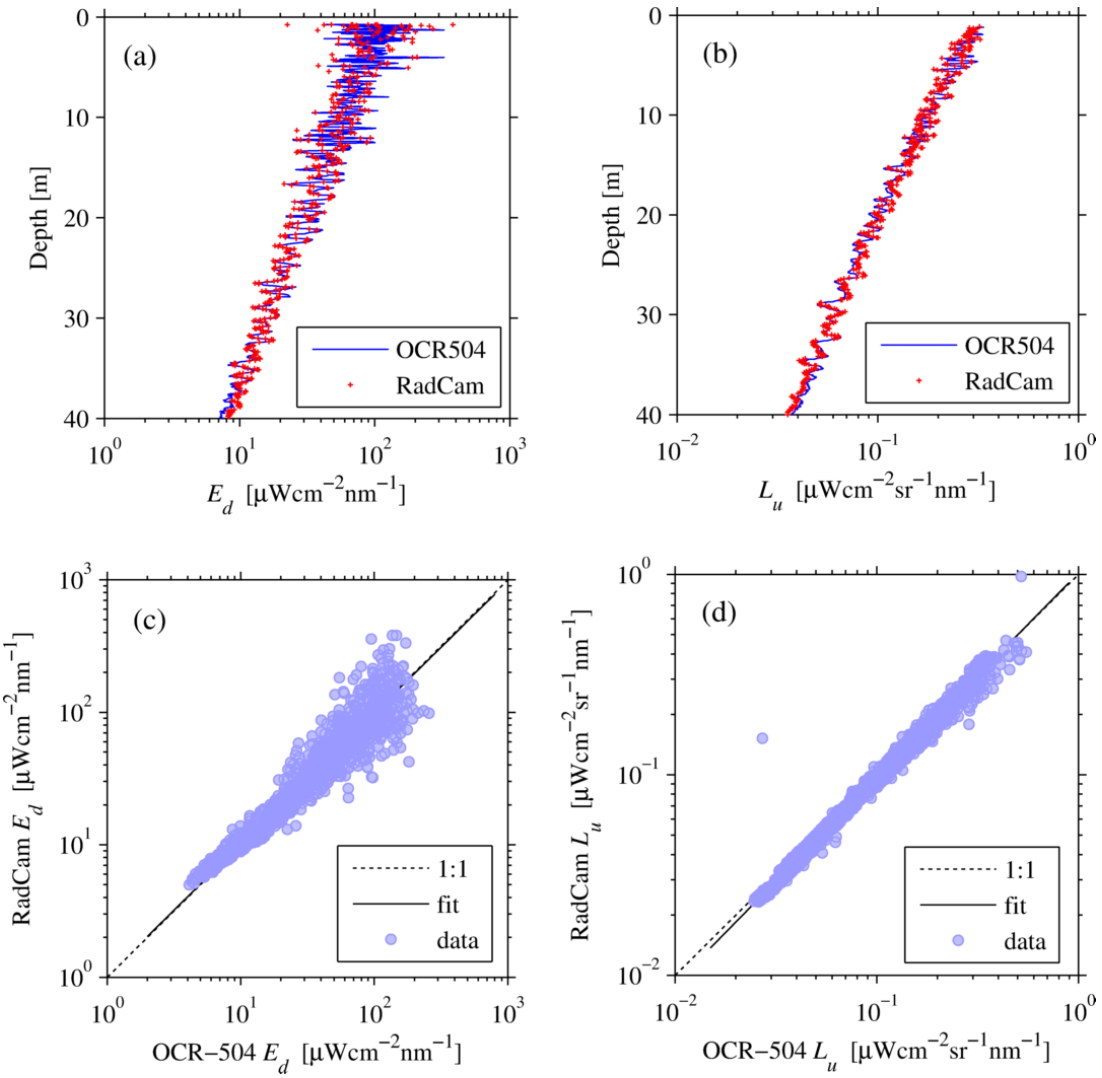

Figure 3.11 Comparison of the camera measurements with the OCR-504I/R radiometer measurements (555 nm) under sunny skies. (a) Example depth profiles of the downwelling plane irradiance E_d. (b) Example depth profiles of the upwelling nadir radiance L_u. (c) Scatter plots of the downwelling plane irradiance retrieved from measured depth profiles; the best fit is given as $\log_{10}Y = 0.992\times\log_{10}X+0.009$, $R^2 = 0.938$, N = 2189. (d) Scatter plots of the upwelling nadir radiance from retrieved depth profiles; the best fit is $\log_{10}Y = 1.025\times\log_{10}X+0.006$, $R^2 = 0.990$, N = 2211.These data were collected from

surface down to 40 m in Pacific Ocean off the Big Island of Hawaii, during August 27 to September 14, 2010.

3.6. Discussion and Summary

RadCam is the first in situ ocean imaging radiometer capable of a response spanning over 6 orders of magnitude in a given instantaneous scene and up to 9 orders with changes in exposure. The high dynamic range measuring capability permits the mapping of the full 4π radiance field in the near-surface water environment. The new camera can operate at a faster rate, up to 15 Hz, than existing oceanographic radiance camera systems [e.g. *Voss and Chapin*, 2005]. This development of a high-dynamic-range radiance camera system represents a fundamental improvement to the radiometry of in-water optical measurements.

Based on the data comparison made in the lab and field, good agreement has been achieved between the RadCam measurements and other reference instruments with an average difference of 14%-16% over the wide dynamic range. Uncertainties in the light source, non-linear high dynamic range response functions, immersion factor, point spread function and the nonuniform spectral response over the 20-nm bandwidth all contribute to the combined uncertainty. Among them, the high dynamic range response functions are fundamental to the instrument development and are probably the principal contributor to the total uncertainty. The upwelling radiance measurement was always collected with low-exposure settings, which showed a small uncertainty of only 6%-10%.

The hi-exposure response function was used to measure the extremely high dynamic range in the downwelling radiance distribution in the upper water column for clear oceanic water such as the Pacific Ocean. The limit of detection of the camera with this exposure setting is ~0.1 $\mu Wcm^{-2}sr^{-1}nm^{-1}$. To measure the radiance field under a cloudy sky, or at great depths of the water column or of the upwelling light field, the mid- or low-exposure setting was switched to reduce the noise at low radiance levels resulted by the high-exposure response function. The limit of detection with the low-exposure setting is better than 0.003 $\mu Wcm^{-2}sr^{-1}nm^{-1}$ (Figure 3.7).

The high dynamic range, geometrically and radiometrically accurate, and multi-angular imaging system provides new possibilities for applications of hydrologic optics. For example, it can be readily deployed to measure the light field in calm or high seas. Data can be directly used for ocean optical modeling and quantification of the optical properties of the water [*Jerlov*, 1976]. The simultaneous measurement of the sky (plus the sun) radiance distribution allows the evaluation of the influence of clouds, sea-surface roughness, and in-water inherent optical properties in shaping the evolution of the radiance distribution with depth.

The newly developed instrument has also shown excellent potential for atmospheric monitoring. In particular, the un-occluded camera system can be employed for all-sky (including the sun) radiance mapping in absolute scales. Such data are requisite in atmospheric radiative transfer modeling, solar radiation, lighting condition and cloudiness monitoring, etc.

There is room to further improve the measurement accuracy when more advanced imaging technology and image-processing technique becomes available. A future design

may also consider multi-spectral resolving capability and polarization effects. Related data processing algorithms are worth investigating as well, in particular, for the high dynamic range image deblurring.

Chapter 4. The Mean Light Field in Three Optically Different Sea Waters: Radiance Distribution as a Function of Water Depth

4.1. Introduction

The optical properties in the first tens of meters of the upper ocean water column, including the apparent optical properties and inherent optical properties, are vital for addressing many problems of the ocean including physics, chemistry and biology [*Cullen et al.*, 1997; *Dickey and Falkowski*, 2002; *Dickey et al.*, 2011; *Johnsen and Sosik*, 2004; *Lewis et al.*, 1990]. A significant source of uncertainty in prediction of the optical properties of the ocean is the geometrical distribution of the radiance field and its variation with respect to the water depth [*Aas and Højerslev*, 1999]; this uncertainty directly affects attempts to use measurements of reflectance and attenuation for diagnoses of ocean constituents. Uncertainties in depth-dependent variations in the radiance distribution, and their sources of variation, propagate as well to the prediction of the performance of new imaging systems.

---

* This chapter is an amended version of a published paper and reproduced by permission of American Geophysical Union: Lewis, M. R., J. Wei, R. Van Dommelen, and K. J. Voss (2011); Quantitative estimation of the underwater radiance distribution; *Journal of Geophysical Research*, *116*(C00H06), doi:10.1029/2011JC0072 75. The contribution of the author of this study includes camera development, deployments at sea, data processing and analyses, model development, and writing of the first draft. The other coauthors contributed to conceptual design, deployment at sea, data analysis and manuscript preparation.

As a fundamental quantity, the radiance distribution and its gradients with depth can be used to derive all other radiometric quantities. In particular, the various irradiances are derived by weighted integration of the radiance field over defined solid angles. The downwelling and upwelling plane irradiances are given as the cosine-weighted integration of the radiance distribution over the upper (downwelling) and lower (upwelling) hemispheres, respectively, separated by a horizontal surface oriented normal to the local gravity vector. Their sum is useful to define the flux of energy across a given depth horizon in the ocean. Scalar irradiances can also be derived from the unweighted integration over various angular domains, which is indispensible for primary production estimates [*Morel*, 1991]. The distribution functions (e.g. the average cosines) are computed directly, as are the various diffuse attenuation coefficients and reflectance [*Mobley*, 1994].

In principle, measurement of the full radiance distribution, and its depth derivatives, permit not only the computation of the above-mentioned apparent optical properties which depend on the angular structure of the radiance field [*Preisendorfer*, 1976], but also all of the important inherent optical properties, which do not depend upon the radiance field. For example, the well-known Gershun's [1939] equation can be directly computed from the vertical distribution of the radiance field and the subsequent integration of the canonical radiative transfer equation (see Eq. (2.28)). The result is a direct evaluation of the absorption coefficient [e.g. *Voss*, 1989a].

Nevertheless, there are very few locations with existing measurements of radiance distribution. Measuring the radiance distribution once received some attention in the mid 20th century in some sea locals [e.g. *Jerlov and Fukuda*, 1960; *Lundgren and Højerslev*,

1971; *Sasaki et al.*, 1958] and the lakes [*Tyler*, 1958]. It is perhaps surprising that there have been few subsequent direct observations until recently [e.g. *Voss et al.*, 2003]. The hemispheric in-water radiance distribution has only been measured quantitatively and in a radiometrically accurate way (e.g. by reference to national standards of radiance, such as NIST) in the observations of Voss and colleagues [*Voss*, 1989b; *Voss and Chapin*, 1992; *Voss and Morel*, 2005] and *Antoine et al.* [2013]. The quantitative measurement of the full radiance distribution has only been realized in a very restricted set of environmental conditions, such as the upwelling radiance distribution at sea surface or the downwelling radiance distribution at deeper locations where the sunlight has been greatly attenuated and would not saturate the imaging array. A significant knowledge gap exists in the upper tens of meters in the water column of the sea, where the hemispheric radiance field measurement is generally absent.

Several models have been proposed for the variation in the upwelling radiance field and the effect of this variation on interpretation of measurements of the ocean reflectance made above the water [*Mobley*, 1989; *Morel and Gentili*, 1993; *Voss et al.*, 2007; *Zaneveld et al.*, 2001a; *Zaneveld et al.*, 2001b]. For example, the often used "Q" factor, the ratio of upwelling irradiance to upwelling nadir radiance, has been shown to be much more variable than previously thought [*Hirata et al.*, 2009; *Morel et al.*, 2002; *Zibordi and Berthon*, 2001]. The average cosine is rarely reported in near-surface waters, but is a critical component in many irradiance-based radiative transfer models [*Gordon*, 2002 and references therein]. Little work has been done to validate models with respect to the full radiance field in the ocean largely because few quantitative measurements exist [*Adams et al.*, 2002; *Mobley et al.*, 1993].

One objective of this study is to render an interpretation of the mean radiance field as a function of the water depth only. We will examine the hemispheric measurements of the angular structure of the light field in the surface water in three sea regions, which are characteristic of different scattering and absorbing properties and nutrient levels. The water body will be treated as vertically stratified but horizontally homogeneous environment, that is in accordance with the plane-parallel theory. The second objective is to characterize the optically different types of sea water in terms of the apparent optical properties and some inherent apparent optical properties based on the radiance distribution measurements.

4.2. Materials and Methods

4.2.1. Experiments

Measurements of the underwater radiance distribution were carried out in three optically diverse environments. The first data set was collected in the Santa Barbara Channel, California, USA (Figure 4.1). This area is a coastal region with moderate phytoplankton biomass and productivity [*Anderson et al.*, 2008], and is an optically complex mesotrophic environment [*Chang et al.*, 2006]. We deployed the RadCam instrument system from the R/V *Kilo Moana* at a station of depth 150 m in September 2008 (34°12.3' N, 119°37.7' W). The second field expedition was completed onboard a 15 m fishing vessel in Bedford Basin (44^{o}42' N, 63^{o}37.8' W), Nova Scotia, Canada, on July 31, 2009. This semi-enclosed fjord-like inlet receives nutrient inputs from the surrounding urban community, and is a typical eutrophic environment [*Strain and Yeats*, 1999]. Our third deployment resulted in data collected during a month-long experiment in the open

Pacific Ocean, southwest of Hawaii, USA from late August to mid-September of 2009, again aboard the R/V *Kilo Moana*. The cruise track followed the drift of the accompanying R/P *FLIP* (floating instrument platform) over approximately 500 km through these clear oligotrophic waters.

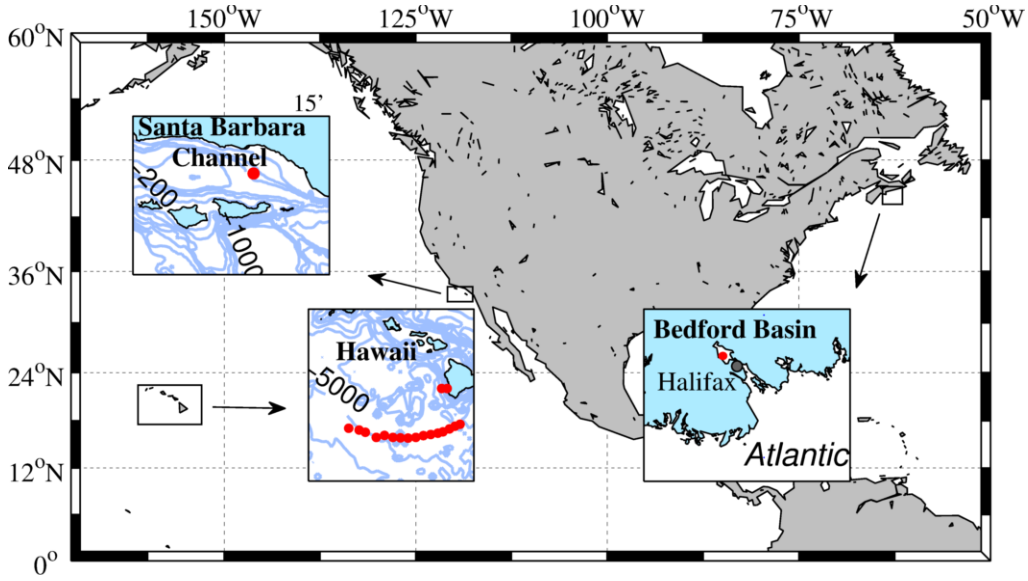

Figure 4.1 Experiment locations in the Santa Barbara Channel, California, the Pacific Ocean, off Hawaii, and the Bedford Basin, Nova Scotia. The stations have been denoted as red dots.

According to *Jerlov*'s [1976] optical classification scheme, the open Pacific Ocean site represents oceanic water Type I with maximum above-water spectral reflectance in the deep violet (near 400 nm), the Santa Barbara Channel site corresponds to Jerlov's oceanic water Type III, with spectral reflectance highest in the green (512 nm) and the Bedford Basin site represents Jerlov's coastal water Type 5 with maximum reflectance at ~550 nm. Based on the bipartite water classification scheme [*Morel and Prieur*, 1977],

the clear water in the Pacific Ocean belongs to Case 1 water, where the water optical properties are dominated by the phytoplankton and associated materials. The study sites in SBC and the Bedford Basin can be classified as Case 2 waters, whose optical properties are impacted by other decoupled materials such as inorganic particles.

A reference camera was set up on the ship's upper deck to monitor the sky radiance distribution including the sun. Another reference irradiance sensor (OCR-504I; Satlantic LP) was also set up to measure above-water spectral downwelling plane irradiance $E_s(\lambda)$. All sensor observations, consisting of the radiance cameras, OCR-504I, CTD and tilt sensor, were synchronized with a GPS time signal to within 5 ms absolute accuracy.

In the Pacific Ocean and the Santa Barbara Channel, the tethered underwater RadCam package was deployed from the stern of the vessel. At least a 50-m distance from the stern was generally achieved before the RadCam instrument package was released and started profiling the water column with a drop rate of ~0.2-0.3 m s^{-1}. With a camera sampling rate of 4 Hz, it took approximately 2 minutes to complete the scanning of the water column to 40 meters depth with a depth resolution of ~5 cm. In the Bedford Basin, the camera was released from a position about 10 meters away from a small boat. A sampling rate of 1 Hz was used and profiles were taken to 20 meters.

During the expeditions in Hawaii and the Santa Barbara Channel, the total absorption coefficient and attenuation coefficient of the water column were measured with the WET-Labs AC-9 meter. The AC-9 meter measures the spectral absorption and attenuation coefficients at nine wavelengths in the visible and near infrared (including 555 nm). Details of the AC-9 calibration of temperature, salinity, and scattering error corrections are described by *Twardowski et al.* [1999]. Briefly, the absorption measurement used a

reflective tube with a diffuser in front of the detector to collect most of the scattered light in the cell. The attenuation measurement was made with a 0.93° acceptance for scattered light. Field, purified-water, blank calibrations were carried out within 2 days of in situ measurements. Corrections for time lags, the temperature and salinity dependence of pure water absorption and attenuation, drift, and absorption scattering error were applied in post-processing.

According to the field AC-9 measurements, the surface water in the Pacific Ocean is the optically clearest of the three sites with the smallest optical attenuation coefficient and scattering coefficient (c(555nm) = ~0.1 m^{-1}, b(555nm) = ~0.037 m^{-1}). These two coefficients are much larger at the experiment site in the Santa Barbara Channel (c(555nm) = ~0.49-0.66 m^{-1}, b(555nm) = ~0.46-0.65 m^{-1}). Historical AC-9 measurements in the Bedford Basin show a wider range of beam attenuation coefficient and scattering coefficient (c(555nm) = ~0.30-1.6 m^{-1}, b(555nm) = ~0.3-1.4 m^{-1}) (http://bbomb.ceotr.ca).

During the experiments in Hawaiian waters and in the Santa Barbara Channel, the water column was also profiled with a 911 plus CTD package. The chlorophyll fluorescence was also measured by a SeaPoint fluorometer. The profiles of chlorophyll concentration were derived from the calibrated fluorescence measurements.

4.2.2. Radiance Data Processing and Analyses

The solar zenith angle, θ_s, is calculated from the geophysical coordinates and the time of observation [*Reda and Andreas*, 2004]. In the Pacific Ocean experiment, θ_s was generally limited to < 30° while the water column was profiled. For the Santa Barbara Channel experiment, θ_s was between 40° and 50°. In the Bedford Basin, the depth profiles were

retrieved when the solar zenith was at $\theta_s = 43°$. The relative azimuth was computed from the astronomical calculations based on the location and time, and the measured compass heading of the instrument onboard the RadCam instrument package.

The sky conditions are classified based on the all-sky radiance observations. Ideal, completely clear skies are rarely met at sea. Rather there often exist some clouds in the mid-zenith angles to the horizon. For the following computations, these situations were treated as clear skies as long as the sun was not directly blocked. Since the radiance distribution profile was usually retrieved during a very short period, no quantitative efforts were made to identify variations in the sky conditions.

The absolute responsivity, immersion factor and the point spread function were applied to the processing of the underwater raw radiance data. The calibrated radiance distribution was subject to inclination correction through the trigonometric transform, which is three-axis correction for the roll, pitch and heading (yaw).

Irradiances were derived from the measured radiance distribution based on integration schemes. For example, the plane irradiance, E_d, and E_u, can be calculated as

$$E_d(z) \text{ or } E_u(z) = \sum_{i=1}^{i=I} \sum_{k=1}^{j=J} L(i, j, z) \cos\theta_{ij} \Omega_{ij} \tag{4.1}$$

where Ω_{ij} is the solid angle subtended by pixel indexed by (i, j), which corresponds to a location with central zenith angle θ_{ij}, and $L(i, j, z)$ is the corresponding radiance recorded by pixel (i, j) at depth z by a camera. The solid angles Ω_{ij} and zenith angles θ_{ij} represented by each pixel were determined by the projection geometry of the camera (see Eq. (3.3)). The scalar irradiance, E_{od} and E_{ou}, can be derived as

$$E_{od}(z) \text{ or } E_{ou}(z) = \sum_{i=1}^{i=I} \sum_{k=1}^{j=J} L(i, j, z)\Omega_{ij} \tag{4.2}$$

With the radiance and irradiance fields being determined, the average cosine (Eq. (2.8) to Eq. (2.10)), reflectance (Eq. (2.12)) and the *Q* factor (Eq. (2.11)) were computed.

The diffuse attenuation coefficients for the horizontally averaged light field at specific depths were estimated by the integration method [*Zaneveld et al.*, 2001b]. It was originally designed to derive the K_d from the irradiance depth profiles which usually have fluctuations due to the sea waves. It is assumed that the light field has an exponential profile, $\overline{E_d(z)} = \overline{E_d(0)}\exp(-K_d z)$, where the bar denotes the mean irradiance at specific depth. Integration of the irradiance $E_d(z)$ from a depth z_0 where the fluctuations in irradiance due to the sea waves are small, to successively shallower depth z is

$$E(z) = \int_{z_0}^{z} E_d(z)\mathrm{d}z = \frac{\overline{E_d(0)}}{K_d}\left[\exp(K_d z_0) - \exp(K_d z)\right] \tag{4.3}$$

It is obvious that integrated irradiance $E(z)$ also varies as an exponential function of water depth z. This integrated irradiance can be numerically computed by subdividing the space into small bins along the vertical and allowing the $E(z)$ to represent the irradiance in the immediate neighborhood. For profiles such as those obtained in Hawaiian waters, integration of irradiance starts at z_0 = 40 m, and proceeds from 40 to 39 m, from 40 to 38 m, from 40 to 37 m, and so on, to obtain $E(39)$, $E(38)$, $E(37)$, etc. And K_d can calculated by least-square fitting an exponential to $\Delta E/\Delta z$. The depth z_0 is set to 25 m and 15 m in the Santa Barbara Channel and the Bedford Basin respectively. This integration method is also applied to the determination of the diffuse attenuation coefficients of the directional radiance profiles and other irradiance profiles.

4.2.3. Simulations of the Radiance Distribution

The underwater radiance distribution is also simulated with the Monte Carlo model. For efficiency, we have adopted the backward Monte Carlo (BMC) scheme [*Collins et al.*, 1972]. In implementing the BMC, the photons are traced from the radiance sensors to the light source. The geometric distance travelled by a photon is described as $l = -\ln(rand)/c$, where *rand* stands for a random number of the uniform distribution, and c is the beam attenuation coefficient. The fate of each photon is governed by its random encounter with absorbers and scatters. And the probability of the scattering occurrence is dictated by the single scattering albedo ω_o. For example, if a random number of the uniform distribution is smaller than the scattering albedo, the photon will be scattered. If otherwise it is absorbed, the fate of the photon comes to an end and the tracing of the photon is terminated. In the model, the phase function is transformed to a form equivalent to the cumulative density function. A new random number is generated and used as the probability to define the scattering angle ψ. The scattered photon is continuously traced until upon the sea surface. If the incident angle is larger than $\theta_{cr} = 48.6°$, the photon is subject to total internal reflection and the tracing iscontinued. Otherwise, the local sea surface reflectance ([0, 1]) is compared with a newly generated random number. If the reflectance is smaller than the random number, the photon escapes the water. Depending on its travelling direction in the air, the photon can be weighted by the radiance in the corresponding sky element to which the photon is heading. A general introduction to the Monte Carlo method is given elsewhere [e.g. *Kirk*, 2004; *Leathers et al.*, 2004].

In our model the radiance sensors have a very small field of view (half angle $\alpha_{1/2} = 0.25°$). The water body is assumed homogeneous and infinitely deep. The optical

absorption coefficient and scattering coefficient at 555 nm are taken as averages from the direct measurements by the WET-Labs AC-9 meter. The averaged Petzold's scattering phase function [*Mobley et al.*, 1993] is adopted in the model. The air-sea interface is simulated by a Gaussian model [*Cox and Munk*, 1954], which depends on the wind speed above the sea surface (see Eq. (2.30)). The wind speed is assumed about 1.5 m s^{-1} above the sea surface. The radiance distribution of the skylight and sunlight is taken from the measurements by the sky radiance camera in the Pacific Ocean. For each model run, there are 74 radiance sensors evenly arranged in both the principal plane and the vertical plane, with a spatial resolution of 5°. In each direction, there are a total of 10^7 photons being released and traced.

4.3. Results

4.3.1. Hemispheric Radiance Fields

Figure 4.2 illustrates typical radiance distributions at near-surface depths in the clear waters off Hawaii. Each panel presents the hemispheric radiance field defined in polar coordinates. The coordinate's origin corresponds to either the zenith direction ($\theta = 0°$) for the upper hemisphere ($0° \le \theta \le 90°$) or the nadir direction for the lower hemisphere ($90° \le \theta \le 180°$). The zenith angle along the image edge in both hemispheres is equal to $\theta = 90°$, i.e., the horizon. The zenith angle changes linearly from the origin to the horizon. The relative azimuth angle is labeled along the horizon; the direction of the sun (i.e. φ=0˚) is at the top of the figure. Each pixel gives the directional radiance in a specific direction (θ, φ). The radiance field in each hemisphere has an angular resolution $\Delta\theta$ of 0.45° along

the radial direction. Along the azimuthal direction, however, the angular resolution depends on the radial position. For example, the $\Delta\varphi$ increases from 0.35° when $\theta = 10°$ to 2.5° when $\theta = 80°$. The sea surface area resolved as in the radiance map depends on water depth as well as the radial position. In Figure 4.2, the sea surface resolution ΔA near the zenith direction is about 2 cm^2. Away from the zenith direction, the surface resolution becomes coarser.

Figure 4.2a gives an example for the downwelling radiance distribution under sunny skies. In the near-surface radiance field a clear Snell's window is evident, which is defined as a conic region with $\theta = 48.6°$. The Snell's extinction boundary generally divides the hemisphere into light refraction region ($\theta < 48.6°$) and internal reflection zones ($\theta > 48.6°$), with wave-focused photons adding large contributions near the surface and scattered photons playing a more important role with depth. The all-sky radiance is therefore concentrated within the Snell's window. It is noted that, however, the boundary is often disrupted by surface waves even for the calmest of sea states. For these conditions, the Snell's window is roughly symmetric about the zenith.

Another prominent feature with the downwelling radiance field is the refracted glitter pattern of the sun, i.e., the glitter as seen from beneath the surface [*Cox and Munk*, 1956]. Depending on the surface roughness, the refracted sun splits into several or many irregularly distributed image fragments. For example, many pixels in Figure 4.2a have measured radiances higher than 1000 $\mu Wcm^{-2}sr^{-1}nm^{-1}$; these numbers exceed those in the all-sky radiance distribution measured above the surface. The refracted solar images in a given scene constitute an instantaneous glitter pattern which varies considerably with the

passage of individual waves, with the location of the glitter often translated away from the 0° in azimuth as a result of surface waves.

Figure 4.2b shows an interesting example for the upwelling radiance field. The data are close to the same depth horizon as in Figure 4.2a in the Pacific Ocean. The upwelled radiance field takes a more uniform appearance than its downwelling counterpart. The intra-scene dynamic range spans only two orders of magnitude in surface waters by comparison with six in the corresponding downwelling scene. Some alternating bright and dimmer light beams are evident which converge to a point corresponding to the instrument's shadow in the anti-solar direction. The self-shaded shadow is not evident for these clear waters, but is common to all downward looking sensors [also see *Smith*, 1974; *Voss and Chapin*, 2005]. According to *Gordon and Ding*'s [1992] self-shading model, our measurement could underestimate the nadir radiance $L(\theta = 180°)$ by < 5 % as a result. The bright and dark light patterns are most evident at lower wind speeds (1.5 m s^{-1} in this case). The brightening on the horizon near the direction of the sun is a consequence of scattering from the solar beam and adjacent sky.

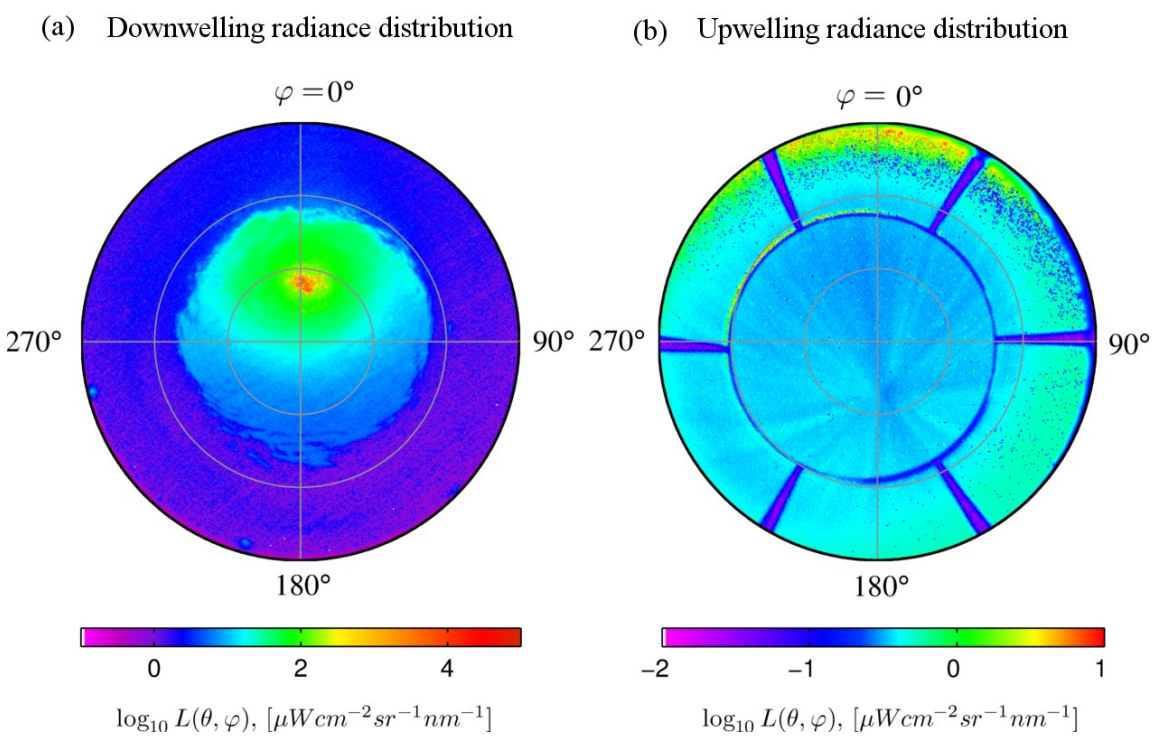

Figure 4.2 Example image of underwater full radiance distribution (555 nm) under clear skies. (a) Downwelling radiance distribution. (b) Upwelling radiance distribution. The data were collected at 2 m depth beneath the sea surface beside the Big Island of Hawaii (155°58′ W, 19°15′ N), on August 27, 2009, at 20:40 UTC; the wind speed was 1.5 m/s and the solar zenith angle was 30°.

Figure 4.3a and Figure 4.3b show the downwelling and upwelling radiance fields under overcast skies in the Santa Barbara Channel but at a higher wind speed (5 m/s). In this case, the scene dynamic range is much lower so a different color scale is used for better presentation. The wavy patterns observed are a result of the ruffled sea surface [e.g. *Hubbard et al.*, 2006]. No clear-cut Snell's window is observed. The instrumental shading effect cannot be easily identified.

Some artifacts are present in our measurements. The telemetry cable is often seen in the upper hemisphere, screws are recorded at the horizon, and the guard framework is evident in the upwelling image. The effects are minor for the downwelling image considering the highly anisotropic light distribution. The blocking of light by the guard framework for the upwelling field will cause an underestimate for the scalar irradiance, but no more than 5%, an error that can be reduced to less than 1% by simple interpolation across the affected pixels.

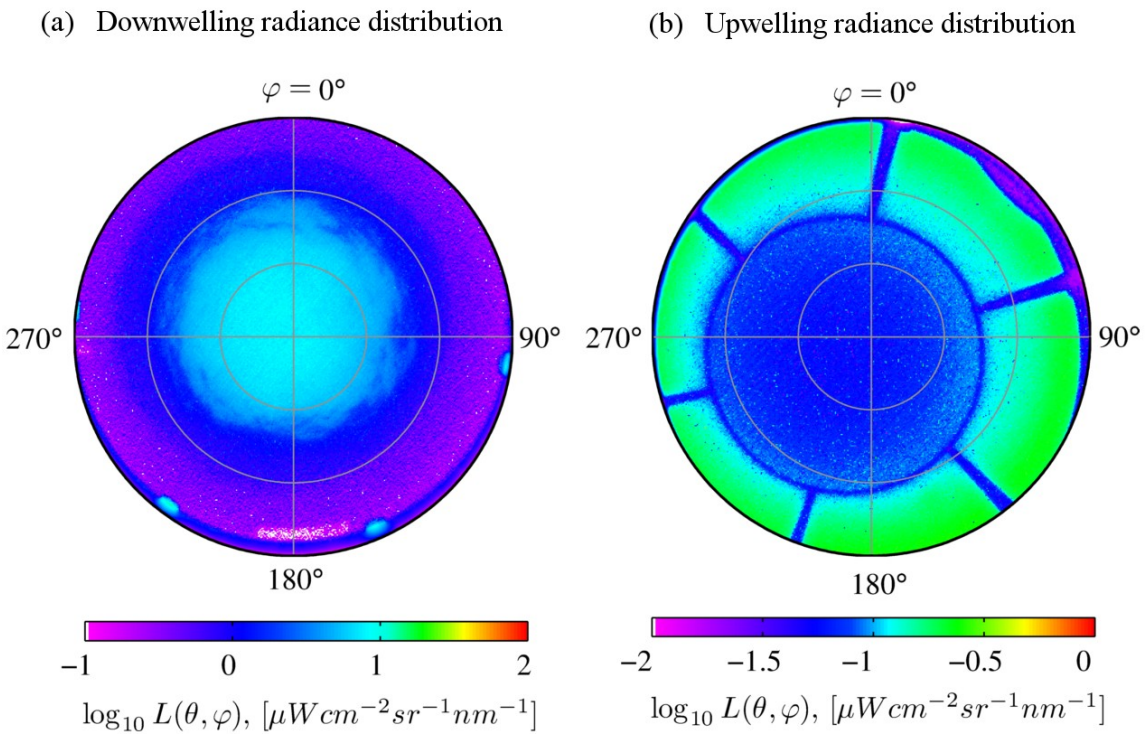

Figure 4.3 Example image of underwater full radiance distribution (555 nm) under overcast skies. (a) Downwelling radiance distribution. (b) Upwelling radiance distribution. The data were recorded from a depth of 1.75 m in the Santa Barbara Channel, California, on September 13, 2008, at 17:40 UTC; the wind speed was 5 m/s.

4.3.2. Depth Evolution of Radiance Distribution

Figure 4.4 depicts the depth progression of radiance in selected directions in the three environments sampled. The respective solar zenith angles are given Table 4.1. The radiance profiles in Figure 4.4a have spatial resolutions in the vertical of ~10 cm, corresponding to temporal resolution of 0.25 seconds. The profiles in Figure 4.4b and Figure 4c have different resolutions. They represent profiles at different zenith angles, but in the principal plane, that is $\varphi = 0^o$ (the vertical plane containing the sun in air). Note that the values plotted are relative radiances, and furthermore, the individual profiles within each figure have been offset along the abscissa for clarity in presentation.

Fluctuations are found with all radiance profiles. The magnitude of the fluctuations generally decreases with water depth (increased variance at depth for $\theta = 180°$ is due to instrumental noise, not environmental variance). A near-surface maximum of radiance is sometimes observed for the downwelling radiance (e.g. $L(\theta=0°)$ and $L(\theta=45°)$) in Figure 4.4a and Figure 4.4b. According to the wave focusing theory [*Stramski and Dera*, 1988; *Zaneveld et al.*, 2001b], this location corresponds to the focal points of waves. The upwelling radiances are less affected by the waves. As pointed out by *Jerlov and Fukuda* [1960], the observed maxima can be generated as well in the absence of surface waves by refraction and scattering in the ocean interior. For directions close to the refracted glitter pattern, the radiance values might vary by several orders of magnitude within a very short period of time (Figure 4.4b, $\theta = 45°$).

Except for the fluctuations, it follows from Figure 4.4 that below the depth of the local maximum, the decrease of radiance in the Pacific Ocean waters can be represented by the exponential law of $\exp(-zK_L)$. In complex waters of the Bedford Basin, a

noticeable biphasic variation is found; it is associated with an intense sub-surface layer of phytoplankton. A comparison of the diffuse attenuation coefficient for the directional radiance, K_L, is summarized in Table 4.1. K_L is directionally specific, dependent on the sky conditions, and is also a function of water inherent optical properties. In most cases, the zenith radiance diminishes more slowly than the upwelling nadir radiance; a systematic relationship remaining to be explored.

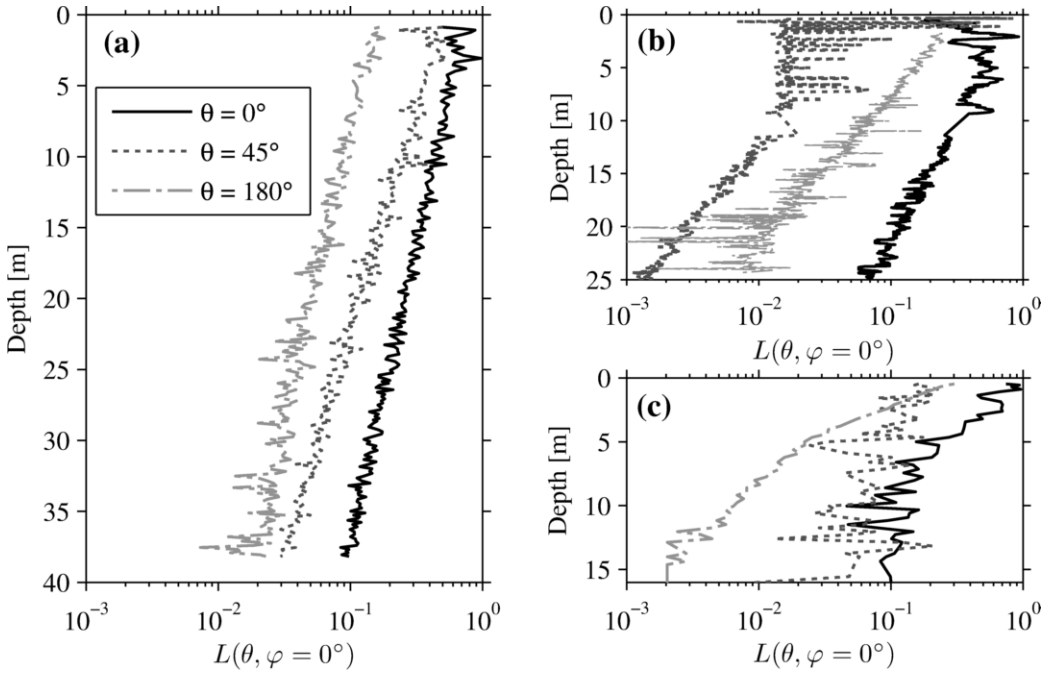

Figure 4.4 Depth profiles of relative radiance for different zenith angles in the plane of the sun under sunny skies. (a) Pacific Ocean; depth resolution is 10 cm. (b) Santa Barbara Channel, California; depth resolution 5 cm. (c) Bedford Basin, Nova Scotia; depth resolution 20 cm. The directional radiance has been arranged along the abscissa axis to attain a clear comparison.

Table 4.1 Comparison of the diffuse attenuation coefficients (unit: m^{-1}) at 555 nm for the directional Radiance $K_{L(\theta,\varphi)}$ in the principal plane (φ =0°).

	Pacific Ocean		Santa Barbara Channel			Bedford Basin	
	Clear sky	Cloudy	Clear sky		Cloudy sky	clear sky	
	0-40m	0-40m	0-5m	10-25m	0-25m	0-5 m	5-15m
0°	0.040	0.059	0.053	0.101	0.121	0.433	0.108
45°	0.059	0.0909	-	0.135	0.124	0.480	0.205
180°	0.055	0.057	0.306	0.305	0.127	0.627	0.097
θ_s	30°	26°	45°	45°	44.5°	43°	43°

The depth evolution for the angular radiance distribution in the principal plane is given in Figure 4.5. All the plots are chosen from the hemispheric radiance distributions which have a glitter pattern or a maximum radiance aligning with the ideally refracted sun's direction (φ = 0°). The most evident feature of the data is the high transparency of the Pacific Ocean water with the highest intra-scene dynamic range radiance. The maximum radiance has only been slightly shifted towards the zenith from 5 m to 45 m. Other conspicuous features can be identified after a close inspection. The peaks for the maximum radiance are usually broad, with high-radiance-value spikes scattered around the maxima associated with the glitter pattern. In the coastal regions, where the sea water is more turbid, the radiance diminishes much faster with depth. The research vessel we used is occasionally captured in the fine radiance structure below the sea surface. An example is given in Figure 4.5b where either the reflective ship's hull or reflective clouds near the horizon generates a refracted bump at θ = 40° in the 1-m radiance distribution curve.

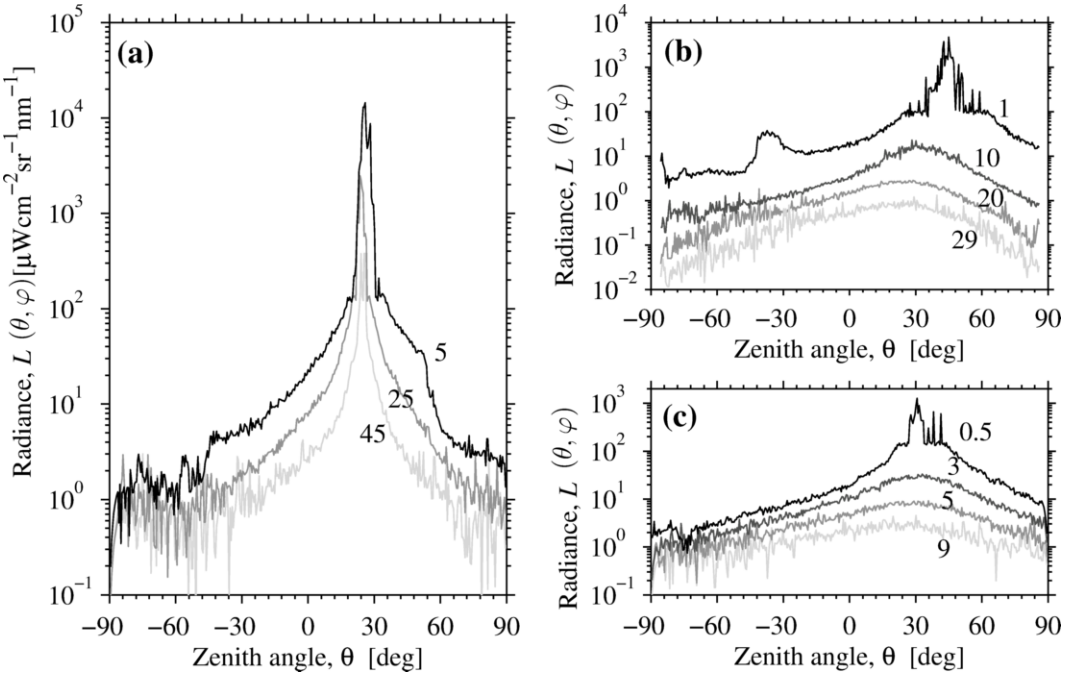

Figure 4.5 Radiance distribution (555 nm) in the principal plane as measured in three waters. All radiance values presented are in absolute units; each curve represents a different depth denoted by the adjacent value (meters). The positive angles refer to the directions at the same azimuth with the sun. The anti-solar directions are denoted by negative angles. (a) Data in the Pacific Ocean, off the Big Island of Hawaii, on August 27, 2009, 20:40 UTC, sunny and a little hazy sky, wind speed 1.5 m/s; (b) Data in the Santa Barbara Channel, California, on September 10, 2008, 23:00 UTC, clear sky, wind speed 7 m/s. (c) Data in the Bedford Basin, Nova Scotia, on July 31, 2009, 19:00 UTC, clear sky, wind speed 6 m/s.

4.3.3. Irradiance Distribution

An application of the radiance distribution is the derivation of the scalar irradiances (E_{od} and E_{ou}) and the vector irradiances (E_d and E_u). Four families of irradiance depth profiles are plotted in Figure 4.6. These data show that the E_{od} depth variations are similar to the E_d profiles, and the E_{ou} profiles behave similarly to the E_u profiles. But the downwelling light may vary with depth quite differently than the upwelling light, depending on the water homogeneity. The rate of decline of the downwelling irradiance is primarily determined by the diffuse attenuation coefficient, while the single-scattering albedo (b/c) plays an additional role for vertical changes in upwelling irradiance.

The diffuse attenuation coefficients are strongly affected by the non-uniform distribution of chlorophyll in these waters, where the subsurface chlorophyll maximum layers were observed at 120 meters, 15-25 meters and 5-7 meters in the Pacific, Santa Barbara Channel, and Bedford Basin respectively (Table 4.2). We found that a relation of $K_u \leq K_d \leq K_{net}$ holds for the clear Pacific Oceanic water, and of $K_{net} < K_d < K_u$ for the complex coastal water of the Santa Barbara Channel. *Hirata* [2003] suggested similar relationships between diffuse attenuation coefficients from a theoretical perspective. His conclusion is now confirmed in light of our field observations. The relative enhancement of the upwelling field and the depression of K_u as a result of Raman scattering in clear ocean waters contributes to the observed inequality as well.

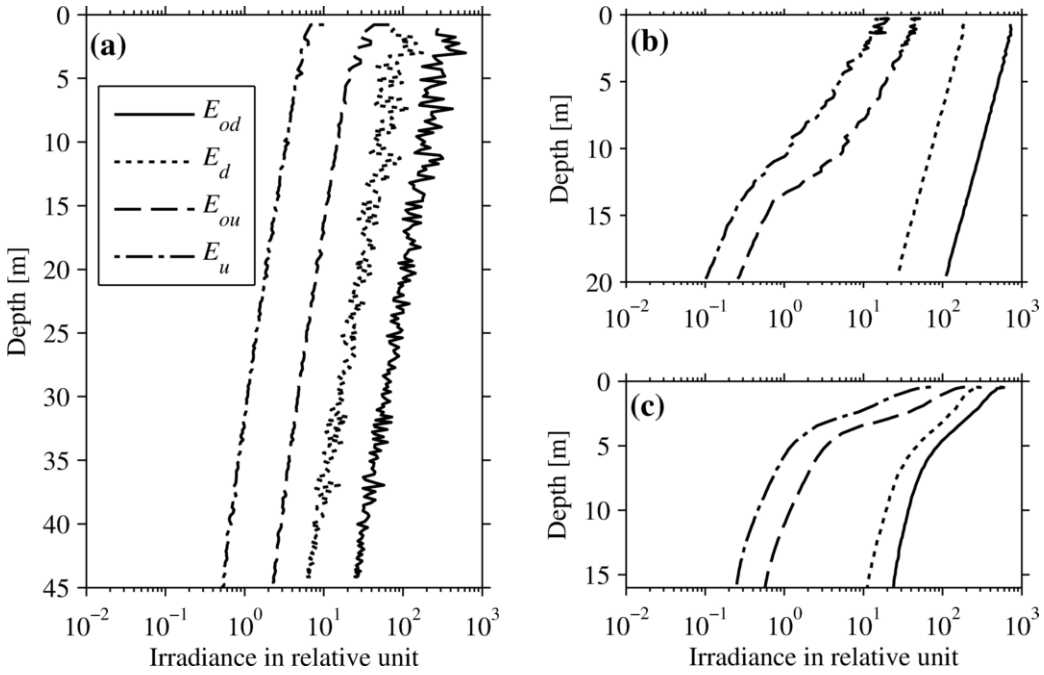

Figure 4.6 Irradiance varying with water depth as derived from the radiance distribution measurements (555 nm). Only the relative values are given for a clear comparison. (a) Data in the Pacific Ocean off the Big Island, Hawaii; collected on August 27, 2009, 20:40 UTC. (b) Data in the Santa Barbara Channel, California; obtained on September 13, 2008, 17:30 UTC. (c) Data in the Bedford Basin, Nova Scotia; measured on July 31, 2009, 19:00 UTC.

Table 4.2 Optical properties in three surface waters as derived from the radiance distribution measurements (555 nm).

Optical property	Pacific Ocean (0-40 m)		Santa Barbara Channel (0-10 m)		Bedford Basin (0-5 m)
	clear sky	cloudy sky	clear sky	overcast sky	clear sky
K_d, m^{-1}	0.064	0.070	0.133	0.112	0.209
K_{od}, m^{-1}	0.062	0.069	0.133	0.106	0.272
K_u, m^{-1}	0.058	0.057	0.167	0.086	0.828
K_{ou}, m^{-1}	0.061	0.063	0.144	0.074	0.716
K_{net}, m^{-1}	0.064	0.070	-	0.113	0.153
K_o, m^{-1}	0.061	0.069	-	0.104	0.338
a, m^{-1}	0.050	0.057	-	0.075	0.131
$\bar{\mu}_d$	0.812±0.030	0.831±0.010	0.655±0.006	0.731±0.017	0.523±0.024
$\bar{\mu}_u$	0.460±0.005	0.452±0.031	0.376±0.048	0.418±0.025	0.286±0.053
$\bar{\mu}$	0.782±0.033	0.807±0.012	-	0.667±0.023	0.412±0.083
R	0.013±0.003	-	0.111±0.017	-	0.162±0.104
$Q(0^-)$, sr	3.379±0.187	3.607±0.235	4.087±0.199	4.660±0.256	4.478±0.533
θ_s	31°	26°	53°	44°	43°
1st optical depth, m	16.5	14.3	7.5	9	4.8
$\overline{Chl}$, mg/m	0.04	0.04	0.86	0.78	7.17
Time (UTC)	20:25pm Aug-27-2009	20:50pm Sept-04-2009	23:00pm Sept-14-2008	17:30pm Sept-13-2008	19:00pm Jul-31-2009

* The average chlorophyll concentration within the first optical depth is estimated from CTD casts made board R/V *Kilo Moana* in the Pacific and the Santa Barbara Channel; the chlorophyll concentration in the Bedford Basin is based on online data (http://www2.mar.dfo-mpo.gc.ca/science/ocean/BedfordBasin).

4.3.4. Distribution Functions

Figure 4.7 describes the measured average cosines at around 5 m depth as a function of the solar zenith angles in surface sea waters. The downwelling average cosine, $\bar{\mu}_d$, in clear oceanic waters can be approximated by a linear function of the cosine of the solar zenith angle θ_s. The best model fit for $\bar{\mu}_d$ in the Pacific Ocean is given as $\bar{\mu}_d = 0.812 \times \cos(\theta_{sw}) + 0.100$, $R^2 = 0.84$, N = 34, where θ_w refers to the refracted solar zenith angle within water which is related to the solar zenith angle θ_s by the Snell's law. The upwelling average cosine is only weakly dependent on the solar angle. The average cosines at the same depth, from the Santa Barbara Channel and the Bedford Basin, have lower values than the clear oceanic waters. Due to the limited number of observations, no statistics have been computed for these two environments.

The nadir value for the ratio of upward irradiance to upward radiance (Q; sr) increases across the progression from clear oligotrophic waters to turbid coastal environments. Our measurements of the upwelling radiance field return a Q value for nadir radiance of 3.38 ± 0.19 sr near the sea-surface for clear-sky days in the oligotrophic Pacific, increasing to 4.09 ± 0.20 sr in Santa Barbara Channel to 4.48 ± 0.53 sr in the eutrophic Bedford Basin. The distribution functions are tabulated in Table 4.2.

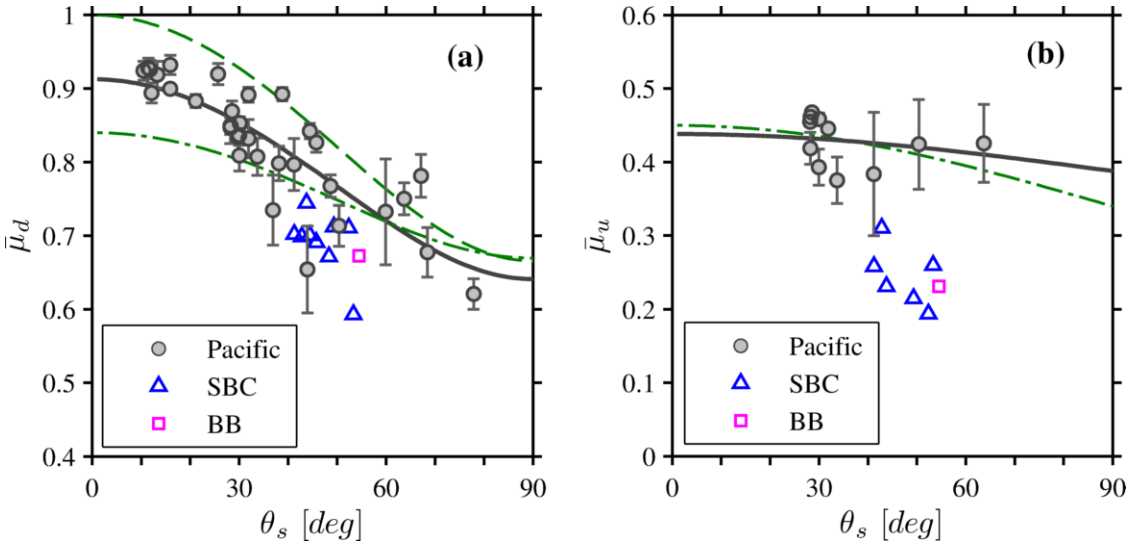

Figure 4.7 Average cosine for green light (555 nm) measured at a depth of 5 m as a function of the solar zenith angle θ_s in three waters. (a) Downwelling average cosine. (b) Upwelling average cosine. The best fit solid line for $\bar{\mu}_d$ in Pacific Ocean is $\bar{\mu}_d = 0.812 \times \cos(\theta_{sw}) + 0.100$, $R^2 = 0.84$, N = 34; θ_{sw} refers to the refracted solar zenith angle within water. The best fit for $\bar{\mu}_u$ in Pacific Ocean is found as $\bar{\mu}_u = 0.050 \times \cos(\theta_s) + 0.388$, $R^2 = 0.046$, N = 11. The dashed line in left graph shows a model, $\bar{\mu}_u = \cos(\theta_{sw})$ appropriate only for collimated beam at normal incidence. The model proposed by *Aas and Højerslev* [1999] is shown for a comparison and denoted by dot-dash line.

4.3.5. Inherent Optical Properties

We demonstrate in this section the retrievals by inversion of some inherent optical properties from the radiance distribution data. Figure 4.8a gives the absorption coefficients in Pacific Ocean. The derived absorption coefficients are found to be lower than in situ measured absorption coefficients by about 10-25% within the 0-40 m water column. In the Santa Barbara Channel, the downwelling and upwelling radiance distribution were measured separately in time, so did not give an accurate estimate for $\bar{\mu}_d$. We started the inversion with the following expression [*Hirata and Højerslev*, 2008], $K_d(z)\bar{\mu}_d \approx a(z)+b_b(z)$, where b_b represents the backscattering coefficient and this expression holds for surface waters where $E_{od} >> E_{ou}$ holds. Figure 4.8b shows the results for (a + b_b - a_w) in the Channel. The noticeable three-sectional variation of the derived absorption is principally a consequence of the variable K_d estimations, for that the E_d profiles were actually measured separately as three segments, when the water inherent optical properties in the Santa Barbara Channel might have varied to some degree. For the Bedford Basin experiment, there was no alternate measurement of water inherent optical properties available for a direct comparison. We computed an average absorption coefficient of 0.131 m^{-1} for 1-5 m water. Historical AC-9 measurements in this region give an absorption coefficient of 0.107 – 0.138 m^{-1}, from November 2008 to early June of 2009 (John Cullen, unpublished data).

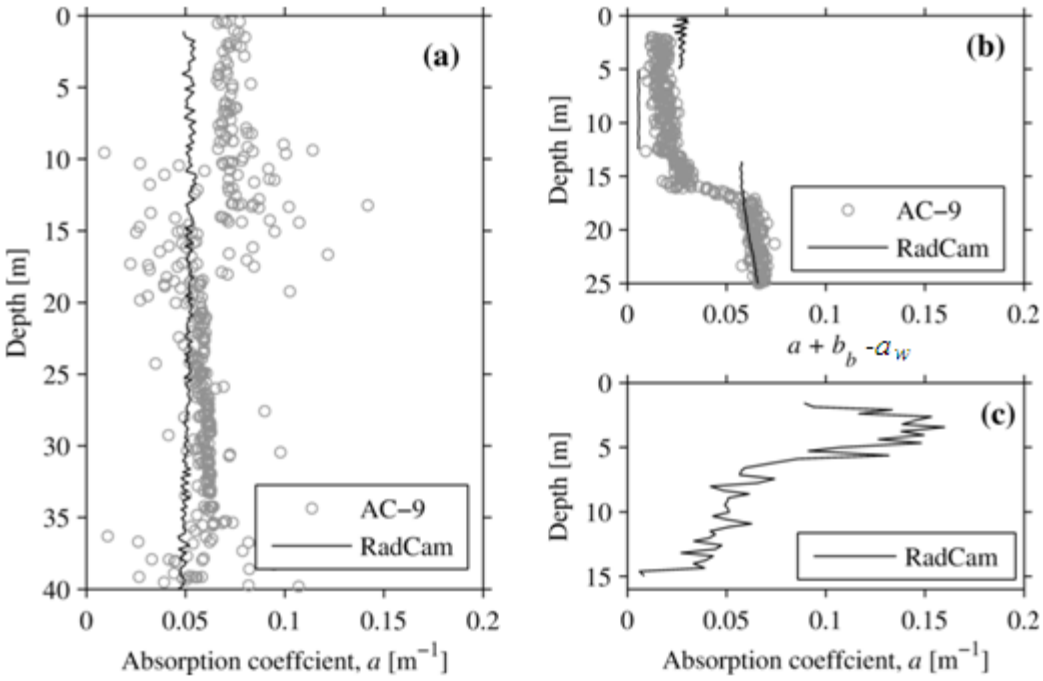

Figure 4.8 Estimation of the inherent optical properties (555 nm) from the radiance distribution data in various waters. (a) Pacific Ocean, on August 27, 2009, 20:37 UTC; (b) Santa Barbara Channel, California, on September 15, 2008, 17:35 UTC; (c) Bedford Basin, Nova Scotia, on July 31, 2009, 19:00 UTC. The AC-9 data are overlaid in (a) for the absorption coefficient only, and in (b) for the sum of absorption coefficient and the backscattering coefficient.

4.3.6. Model-Data Comparison of the Radiance Distribution

For the radiance distribution in the vertical plane, we compared the measurements with Monte Carlo model simulations in this section. For the Pacific waters, the model used an absorption coefficient of 0.06 m^{-1}, and a scattering coefficient of 0.04 m^{-1}, which are the average of the field measurements from water depths 5-40 m. The hemispheric radiance distribution chosen for comparison had a very small glitter pattern and the refracted sun is close to its theoretical position for plane sea surface. Both the simulated and measured radiance distributions are given in Figure 4.9. The simulations represent 74 directional radiances in each vertical plane with a spatial resolution of 5°. The measurements in each vertical plane are composed of about 800 data points in total, corresponding to 800 directions. The simulations generated in relative units are scaled such that they represent the absolute radiance and their upwelling nadir radiance remains equal to the measured upwelling radiance. Qualitative consistence is observed between two data sets. Arange of radiance variation of 5 decades was found for each in the principal plane. The model also predicts very similar fine features to the measured radiance distribution. It is justified to expect this good agreement since the light field in surface water is largely the result of refraction of the sky radiance distribution, which we have already measured at the same time and used in our model. It is also possible that the surface waves have contributed to the observed model-data discrepancy. And the errors with sky radiance measurements and instrument glare may have also propagated into the simulated underwater radiance distribution as well.

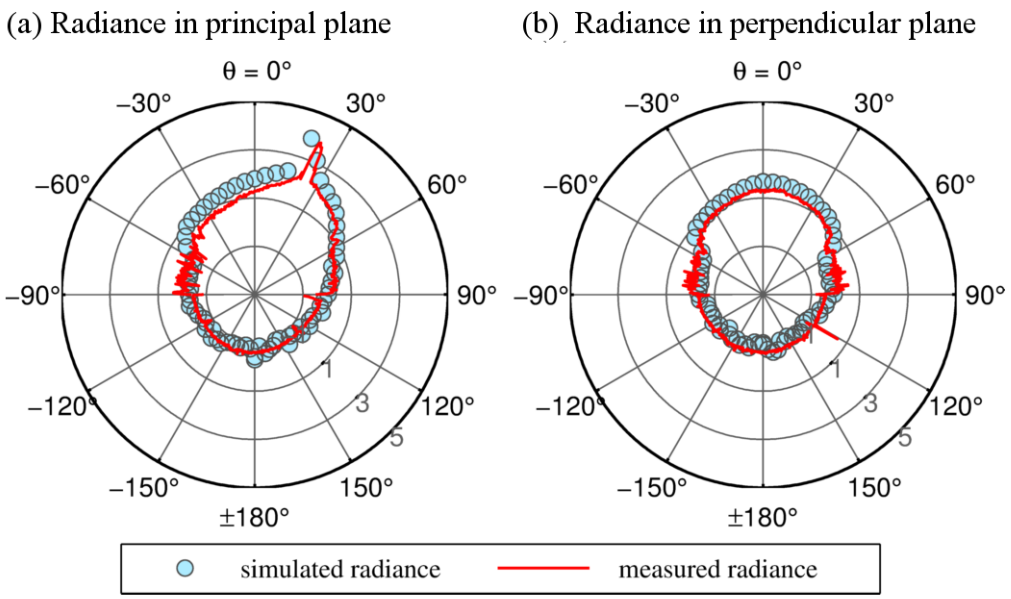

Figure 4.9 Model-data comparison of the radiance distribution at 555 nm. (a) Radiance distribution in the principal plane. (b) Radiance in the perpendicular plane. All the radiance values have been logarithmically transformed to $\log_{10}L(\theta,\varphi)$. The radiance measurements were obtained at a water depth of 5.8 m off the Big Island, Hawaii, on August 27, 2010, at 20:40 UTC. The modeled radiance is normalized to the measured nadir radiance. Both are represented in logarithmic scales. Solar zenith angle is 29° in air. The zenith angles have been labeled. The 0° represents the zenith; and the ±180° points to the nadir. In the principal plane, the positive angles refer to the azimuth direction of the sun, i.e. $\varphi = 0°$ with negative angles corresponding to the antisolar direction, $\varphi = 180°$. In the perpendicular plane, positive angles and negative angles are directions along $\varphi = 90°$ and $\varphi = 270°$, respectively. A radiometer with half angle $\alpha_{1/2} = 0.25°$ is simulated in the model.

4.4. Discussion

A new exploration of the underwater light field and optics is presented with the radiance distribution measurements. The data set collected permits diagnoses of the variations in both apparent optical properties and inherent optical properties (Table 4.2), and the validation of forward models of radiative transfer in the sea.

The radiance distributions given in Figure 4.2 and Figure 4.3 represent the first near-surface simultaneous observations of the full radiance distribution. For the downwelling fields, the clear waters of the Pacific yield very high dynamic ranges as a result of the low attenuation and the relative strength of the absorption coefficient relative to the scattering coefficient in these waters; this allows the radiance from the refracted sun to enter into a limited angular range. The resulting radiance distribution (Figure 4.5) is therefore strongly peaked, approaching the theoretical limit in cross-section across the solar plane when absorption dominates the attenuation coefficient [*Preisendorfer*, 1959]. This is in contrast to the measurements from more turbid coastal and eutrophic waters that had higher scattering albedos that resulted in a flattening of the field; dynamic ranges were more than two orders of magnitude smaller at comparable optical depths in the Santa Barbara Channel relative to those in the open Pacific.

For the clear Pacific waters and for Santa Barbara Channel, almost all of the dynamic range in the downward direction and all of the information regarding the above-water radiance distribution is contained within the well-defined Snell's cone. This is particularly evident for calm sea states where the edge of Snell's cone is sharply defined and where there is little radiance in the region between the edge of Snell's cone and the horizon. For the highly scattering eutrophic waters, Snell's cone is not evident.

For the upwelling fields, the dynamic range is much reduced, and a much more uniform field is seen for all water types, again consistent with theory and other observations [see *Voss et al.*, 2007].

At greater depths, the downwelling field becomes more uniform; the rapidity with which this occurs varies with the relative importance of scattering in the medium. The angle of greatest radiance migrates towards zenith. For the upwelling field, the proportionate change in the relative distribution is small. The depth progression of the radiance distribution is generally consistent with previous analyses [*Jerlov and Fukuda*, 1960; *Lundgren and Højerslev*, 1971; *Tyler*, 1960], except that the dynamic fine structures have been revealed in the hemispheric radiance map. The radiance near the refracted sun is subject to great variability related to dynamics of the sea surface wave slopes [*Mullamaa and Nikolayev*, 1972]. With increasing depth the radiance varies to a lesser degree in terms of the wave disturbance. It is noted that *Tyler*'s [1960] instrument had a half angle of 3.3° and his measurement of the radiance variance is close to our estimations. We emphasize that the size of the refracted glitter pattern could impact the mean and variance of directional radiance. For example, an increasing wind speed and solar zenith angle will give a more diffuse pattern [*Preisendorfer and Mobley*, 1985], and as a consequence, the radiance will experience large variability in many directions. Under overcast skies, the wave effects are most pronounced near the extinction boundary of Snell's cone (Figure 4.3).

Based on *Gordon and Ding* [1992], a maximum self-shading error of 5% and 3% is found possible with the upwelling nadir radiance and upwelling plane irradiance data, respectively. Previous analyses of the full radiance distribution have been based on time-

averaged fields made with multiple observations of radiance at fixed angles [e.g. *Lundgren and Højerslev*, 1971; *Tyler*, 1960]. Our data focus on the near-surface light field, and have not reached the asymptotic radiance field [*Preisendorfer*, 1958b]. The asymptotic light field has only been occasionally reported from previous field observations [e.g. *Lundgren and Højerslev*, 1971] which in theory is only achieved at optical depths greater than ~10 [see *Berwald et al.*, 1995; *Højerslev and Zaneveld*, 1977].

The instrument calibrations and data validations suggest a combined uncertainty of less than 15% in the measured radiances. Since the imager sensor uses a non-linear responsivity function, the radiance at highest and lowest ends of the curve could be subject to larger errors. The discussions above have, however, included both the measurement uncertainties and the light field variability induced by environmental conditions.

The radiance distributions are used to calculate diffuse attenuation coefficients, as well as the average cosines. The average cosine for the downwelling light field shows a relationship with solar angle similar to that observed and described by *Aas and Højerslev* [1999]. The fitted line in Figure 4.7 deviates from the simple cosine model, which is suitable for collimated light only. *Aas and Højerslev* [1999] reported a similar trend for $\bar{\mu}_d$ in the western Mediterranean; their data were measured at wavelengths of 465-474 nm.

To compare this result with the bidirectional reflectance model [*Morel et al.*, 2002], we derived a water column average chlorophyll concentration, $\overline{Chl}$ = 0.04 mg/m^3, for the first optical depth (~16.5 m for light at 555 nm in Pacific region). Morel's model predicts a Q factor of 3.42±0.21 sr, nearly identical to our observation. *Zibordi and Berthon* [2001]

suggest that the Q factor relates to the diffuse attenuation coefficient, and using their approach, we computed the Q factor of 4.84 sr for the Bedford Basin, which compares to our observation of 4.48 sr.

The radiance distribution data have been combined with the Gershun's law to derive the absorption coefficient in clear waters [*Jerlov and Nygård*, 1968; *Lundgren and Højerslev*, 1971; *Voss*, 1989a]. Computation of the absorption coefficient in surface waters (Figure 4.8) exhibits certain discrepancies with direct measurements based on the AC-9 instrument. The "errors" could be from the uncertainties of the measurement and data processing as discussed above, but likely derive to large extent from the missing source terms, especially Raman scattering, in the radiative transfer equation [see *Voss*, 1989a]. On the other hand, there are usually large uncertainties associated with the direct measurement of absorption coefficient itself [*Leymarie et al.*, 2010]. For example, a significant source of error in the comparison of the inverse algorithms with direct measurement stems from the different spatial scales measured; Gershun's law predicts the bulk absorption coefficient over volumes of order 1 m^{-3}, while the in situ spectroradiometer like the AC-9 meter measures the optical properties for a very small volume of water, after it has been pumped into the instrument. All these issues together contribute to the uncertainties in the data-data comparison (Figure 4.9).

4.5. Summary

A complete description of the full radiance distribution in downwelling and upwelling hemispheres has been made in a range of near-surface sea environments. The estimation of the mean radiance field is generally consistent with previous investigations but

provides additional information on the temporal fine structure of the light field near the sea surface. The high-resolution radiance observations permit diagnosis of the variability of the optical properties including the irradiance, all the apparent optical properties and the inherent optical properties in various water bodies. A good agreement is obtained for the radiance measurements and data from other more traditional sources. The measurements shown in this study are generally presented as a function of depth, and have overlooked the uncertainties in the time domain, such as the wave-induced light field variability.

Chapter 5. Variability in the Underwater Light Field: Wave Disturbance of the Radiance Distribution in Ocean Surface Water

5.1. Introduction

The radiance distribution in the upper ocean is strongly influenced by the transmission of light through the sea surface and subsequent absorption and scattering within the water [*Jerlov*, 1976]. For example, the radiance at depth z in optically deep, homogeneous and source-free water can be approximated by the classic canonical equation for radiance [*Mobley*, 1994]

$$L(\theta,\varphi,z) = L(\theta,\varphi,0^-)\exp\left(-cz\sec\theta\right) + \frac{L^*(\theta,\varphi,0^-)\exp(-Kz)}{c-K\cos\theta}\left\{1-\exp\left[-\left(c-K\cos\theta\right)z\sec\theta\right]\right\} \quad (5.1)$$

where $L(\theta,\varphi,0^-)$ ($\mu Wcm^{-2}sr^{-1}nm^{-1}$) is the radiance just below the sea surface, L^* ($\mu Wcm^{-2}sr^{-1}nm^{-1}$) is the path function, which is the radiance per unit length in the direction of the line of sight (θ,φ), generated by radiant energy scattered into the line of sight from all directions, and c and K are the beam attenuation coefficient and diffuse attenuation coefficient respectively. Other sources include inelastic scattering contributions such as

---

* This chapter comprises a coauthored manuscript: Wei J., M. R. Lewis, C. J. Zappa, and R. Van Dommelen (2013); Wave disturbance of the underwater radiance field; *Applied Optics*, in preparation. The contribution of the author of this study includes study design, data processing and analyses, and writing of the manuscript. The coauthors contribute to and help with the radiance data collection, wave data processing and many rounds of manuscript corrections.

Raman scattering and fluorescence, as well as true sources such as bioluminescence. The depth evolution of the light field and its dependence on other environmental factors has been the fundamental problem in hydrologic optics [*Bannister*, 1992; *Hirata et al.*, 2009; *Kattawar and Plass*, 1976; *Kirk*, 1994; *Mobley*, 1989, 1994; *Morel and Gentili*, 2004; *Plass et al.*, 1976; *Spinrad et al.*, 1994], for which the average light field is treated under plane sea surface or plane-parallel environment.

The radiance distribution in the upper ocean varies over a range of time scales. The evolution of the solar position contributes to daily and annual variations. Changes in the inherent and apparent optical properties, such as c and K respectively in Eq. (5.1), contribute as well to both hourly and seasonal changes in the light field. The sea surface waves are responsible for much faster fluctuations in the underwater radiance which occur from seconds to as short as milliseconds [*Darecki et al.*, 2011; *Sabbah and Shashar*, 2006]. Considering all of these variations, prediction of the wave disturbance on the underwater radiance distribution is a daunting problem.

Wave disturbance has made it extremely difficult for accurate estimation of the mean radiance distribution through in-situ observations. For example, the most cited aquatic radiance data was reported to be noisy due to the wave disturbance [see *Tyler*, 1958] even though the experiment was carried out under the most ideal conditions in which the water surface was only slightly roughened by wind, and the water was optically homogeneous, which reportedly were found only on one or two days per year in the experimental area [*Duntley*, 1959]. On the other hand, the effects of wave disturbance as recorded in the measured radiance distribution may provide diagnostics of the surface wave field [e.g. *Hubbard et al.*, 2006; *Stotts and Karp*, 1982]. For marine biologists, there is increasing

evidence that the fast fluctuating radiation impacts the growth rates of phytoplankton [*Greene and Gerard*, 1990; *Stramski et al.*, 1993; *Walsh and Legendre*, 1983] and the activity of fish and animals [*McFarland and Loew*, 1983; *Sabbah et al.*, 2012].

The phenomenological fluctuations in the wave-disturbed radiance start from the boundary condition. The downwelling radiance directly below the random sea surface can be approximated by a simple equation [*Mobley*, 1994; *Walker*, 1994]

$$L(\theta_w, \varphi_w, 0^-, t) = n_w^2 \cdot L(\theta_a, \varphi_a, 0^+, t) \cdot \tau(\hat{\xi}_a \bullet \tag{5.2}$$

where the subscripts w and a refer to the water and air respectively, n_w is the refractive index of the sea water, $\hat{\xi}_a$ is the incident direction of light corresponding to (θ_a,φ_a), $\hat{n}$ is the normal to the sea surface, and τ is the light transmittance. Figure 5.1 illustrates the effects of the wavy sea surface on the underwater light field. Under the mirror-like plane of an undisturbed sea surface, an upward-looking viewer receives the transmitted light after refraction within the Snell's window and the internally reflected light outside the Snell's window (Figure 5.1a). When the sea surface is ruffled by waves, the underwater light field distribution adapts to the instant topography of the sea surface and is contributed by varying sky elements (Figure 5.1b). The internally reflected light may be present within Snell's window, and the transmitted sunlight may be also observed beyond the critical boundary of the Snell's window. The scales of waves, such as wave height and wave length, are important in altering the light distribution.

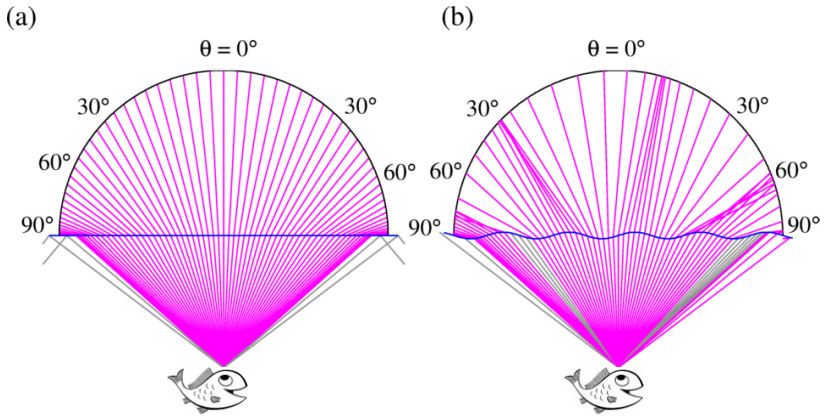

Figure 5.1 Schematic of the light refraction and internal reflection. (a) Viewing geometry under plane sea surface, which only considers the light refraction (denoted by magenta lines) within Snell's window and some internally reflected light (denoted by gray lines) beyond Snell's window. The incident light is evenly arranged from zenith angle 0° to 90°; the transmitted light subtends a conic region with the critical boundary at 48.6°. (b) When the sea surface is present with waves, an upward-looking viewer (with the same viewing geometry) sees a different downwelling light field.

Understanding variations in the radiance distribution requires sufficient sampling of the directional radiance from as many directions as possible and under various environmental conditions. The earliest attempts emerged in the 1970s, when Russian scientists first launched a series of experiments in the Black Sea [*Mullamaa and Nikolayev*, 1972; *Nikolayev and Yakubenko*, 1978; *Yakubenko and Nikolayev*, 1978; *Yakubenko et al.*, 1974]. The fluctuations of "brightness" were actually dealt with in their studies, not the radiance. There have been few subsequent efforts devoted to this optical phenomenon until recently. *Stramska and Dickey* [1998] reported on the upwelling nadir

radiance variation as a result of surface waves. *Sabbah and Shashar* [2006] measured the fluctuations of radiance from the zenith directions of 30°, 70° and 90° on a coral reef off the pier. *Darecki et al.* [2011] developed a porcupine system with thirteen radiance sensors assembled together to simultaneously measure the multiple radiance time series. The shortage of the field observations has led to obvious gaps in the knowledge base, and sometimes resulted in controversial conclusions. For example, two studies have given literally opposite observations about whether the maximum or minimum variation of radiance occurs in the direction of the refracted sun [*Darecki et al.*, 2011; *Nikolayev and Yakubenko*, 1978].

Theoretical study of the radiance fluctuations is rarely carried out, possibly because a complete representation of the sea surface directional wave spectrum is involved and the incurred computing cost is overwhelming [e.g. *You et al.*, 2011]. In the foreseeable future, field experimentation will likely remain an indispensible source to gain insights into the dynamic light field.

This study examines the wave disturbance of the measured radiance field in the near-surface sea water. The time-resolved hemispherical radiance field measurements are obtained from the RadCam radiance camera system. The first objective is to characterize the downwelling radiance fluctuations at shallow depths which have normally been avoided in the past because of the extremely high dynamic range in the downwelling radiance field ($\sim 10^6$) but which can now be resolved with the new camera system. The second objective is to gain insights into variations in the spatial structure of the dynamic radiance field. We wish to test the hypothesis that it is the wave slopes that primarily

determine the underwater radiance fluctuations so that it will be possible to relate the wave slopes to the measured underwater radiance variability.

Specifically, we shall explore several aspects of the phenomenon including the amplitude, periodicity and probability distribution of the fluctuating radiance signals. Attempts are also made to interpret the radiance fluctuations with reference to fluctuations of the integrated irradiance field and the downwelling average cosine. The emphasis is laid on the analysis of radiance field fluctuations within the top several meters under sunny skies.

5.2. Materials and Methods

Field experiments were carried out in relatively clear coastal water of the Santa Barbara Channel (SBC), California between September 12 and 17, 2008, and in clear oceanic water of the Pacific, south of the Big Island of Hawaii from September 3 through September 8, 2009. The environmental conditions for both field experiments are summarized in Table 5.1. A general characterization of the metrological and physical conditions for both regions is given by *Dickey et al.* [2012].

The study area in the Pacific Ocean is located in an open region of 300-500 km southwest of the Big Island, Hawaii which belongs to the optical Case 1 water class [*Morel and Prieur*, 1977], with the diffuse attenuation coefficient K_d(555nm) around 0.06 m^{-1} in the surface water. The northeasterly or easterly trade winds were persistent during the field experimentation. The sea state was moderate to high, and the significant wave heights (mean of the one third of the highest waves) were between 1.8 m and 2.4 m.

During the Santa Barbara Channel experiment, one station (34°12.3' N, 119°37.7' W) was examined with water depths of 150 m. The Santa Barbara Channel can be classified as optical Case 2 water, which is more complex and generally more turbid in terms of the light attenuation properties (Table 5.1). The wind direction was consistently eastward during the observations. The wind speed was relatively smaller than that in the Hawaiian study; the significant wave heights were found to be 0.75 m and 1.7 m.

Table 5.1 Environmental conditions during the field observations.

Station No.	Wind speed [m s^{-1}]	Wind direction [deg]	Significant wave height, H_s [m]	Soalr zenith angle, θ_s [°]	Soalr azimuth angle φ_s [°]	Depth [m]	K_d * [m^{-1}]	c * [m^{-1}]	b * [m^{-1}]
243†	10.6	83	-	27.5	109	4.5	0.067	0.097	0.031
246†	9.9	84	2.2	29.0	253	5	0.068	0.105	0.037
249†	9.2	86	1.8	32.5	254	13	0.069	0.108	0.040
267†	8.6	89	2.3	30.6	109	2.5	0.074	0.101	0.033
650-1‡	7.6	268	-	45	234	0.9	0.125	0.665	0.652
650-2‡	7.8	268	0.8	47	237	1.8	-	-	-
650-3‡	8.7	270	-	50	240	2.3	-	-	-
650-4‡	8.8	270	-	51	242	3.9	-	-	-
750‡	7.3	266	1.8	44.8	233	1.1	0.107	0.492	0.460
953‡	7.2	266	0.8	47.1	235	1.8	0.110	0.601	0.577

† Data from the Pacific Ocean; the optical properties are averaged over 0-40 m.

‡ Data from the Santa Barbara Channel; optical properties are averaged over 0-15 m.

* Wave length at 555 nm.

5.2.1. Radiance Measurements

The radiance time series $L(\theta,\varphi,t)$ was measured in both experiments under clear skies using the newly designed high dynamic range radiance camera. The radiance field in the 2π space is mapped onto the array and represented by a total of ~120000 pixels, forming a circular image with the diameter $D \approx 400$ pixels. Along the radial (or zenith) direction, the pixels perceive the incident radiation in about 200 specific directions (~0.45° apart). The solid angle Ω subtended by each pixel is a function of the radial distance (see Eq. (3.3)). The field of view for each pixel is very small, and slightly decreases with increasing viewing zenith angle θ. For example, the pixel at zenith angle $\theta = 0°$ subtends a solid angle of 6.76×10^{-5} sr, which approximates a conic space of half apex angle $\alpha_{1/2} = 0.25°$. At the viewing direction $\theta = 80°$, the solid angle decreases to 4.77×10^{-5} sr and the equivalent field of view $\alpha_{1/2}$ is about 0.23°. The radiance camera system currently measures the radiance at one waveband (555 nm, FWHM 20 nm).

The primary radiance data sets were retrieved from deployments onboard R/V *Kilo Moana* in the two experiments. To measure the time series radiance at a fixed depth, the profiling camera system was tethered to a float (diameter ~25 cm). The float was kept about 50 m away from the stern of the vessel before the sampling was started, to reduce the shadowing effect and reflection of the vessel's hull. The camera's integration time was about 0.02 s within the surface waters, with the sampling frequency at 8.7 Hz. The instrument inclination and heading direction together with the water depth were simultaneously recorded by a two-axis tilt sensor and a solid state compass respectively. For our measurements, the nominal sensor depths were usually less than 5 meters. We

report the mean of the senor depths as the measurement depth. Each radiance time series spans about four minutes.

The secondary data sets of radiance time series were obtained with the self-logging camera on the research platform of R/P *FLIP*, which was located about two miles away from R/V *Kilo Moana* at sea. This radiance camera was mounted in a cage and lowered into the water from the boom to record the time series.

A sky radiance camera was also set up on R/V *Kilo Moana* to monitor the sky during the underwater deployments. Only the clear-sky conditions were chosen in the following study, that is, there were no observed clouds near the sun during underwater deployments. The simultaneously measured downwelling irradiance right above the sea surface, E_s, varied less than 5% (the ratio of the standard deviation to the mean of the irradiance).

The radiance distribution data were calibrated to absolute units of $\mu Wcm^{-2}sr^{-1}nm^{-1}$. The calibrations included the inclination and heading corrections, whose uncertainties are less than 1°. No further effort was made to extrapolate for the missing radiance values at directions closest to the horizon during the geometrical correction since those radiance values were usually very small and made an almost negligible contribution to the downwelling irradiance field. The time-resolved radiance distribution $L(\theta,\varphi,t)$ was used to derive the time series of the downwelling plane irradiance, $E_d(t)$ (unit: $\mu Wcm^{-2}nm^{-1}$), following Eq. (4.1). Similarly, the time series of downwelling scalar irradiance, $E_{od}(t)$ ($\mu Wcm^{-2}nm^{-1}$), using Eq. (4.2). In these two equations, $L_{ij}\cos\theta_{ij}\Omega_{ij}$ and $L_{ij}\Omega_{ij}$ represent the directional components for the weighted plane irradiance and unweighted scalar irradiance, respectively. The time series of average cosine can be derived as the ratio of the downwelling plane irradiance to the scalar irradiance

$$\bar{\mu}_d(t) = \frac{E_d(t)}{E_{od}(t)} \qquad \text{(dimensionless)} \tag{5.3}$$

5.2.2. Analysis of Light Field Variation

The data volumes of the time series measurements of the radiance distribution are overwhelmingly large. In the course of each deployment, for example, the radiance time series was recorded in 120000 directions at high frequency; the 4-minute long time series of radiance distribution measurements resulted in storage requirements for 2 Gigabytes. For the convenience of presentation, only analysis of the time series of radiance in specific directions was chosen for further presentation. In this study, we analyzed ~500 directional radiance time series for each deployment. These directional radiance sequences were retrieved every 5° apart in both zenith (0-90°) and azimuth directions (0-360°). Furthermore, these selected directions were constrained to the range of 0-70° in zenith angles; beyond the critical direction of 70°, some radiance data were possibly lost due to camera's inclination and related geometrical corrections.

The probability distribution function (PDF) of the radiance fluctuations was examined. The original radiance sequence was normalized to its mean, $L_n = L/\bar{L}$. Then the histogram for the normalized radiance was derived with the choice of Scott's bin width [*Scott*, 1979], $W_{\text{scott}} = 3.49\sigma_L N^{-1/3}$, where σ_L is an estimate of the standard deviation for the normalized radiance, and N is the total number of data points. The experimental histogram was further normalized to get the empirical probability density function for the considered radiance time series. To find out which theoretical model describes the empirical data, four theoretical distribution functions were considered, including the

normal distribution, lognormal distribution, Weibull distribution and extreme value distribution (EVD). These models usually give a reasonably good description for fluctuations in irradiance [e.g. *Gernez et al.*, 2011; *Rørslett et al.*, 1997]. The mean and the standard deviation required by the normal and lognormal functions were estimated from the empirical data. The parameters in the Weibull and EVD models were determined according to the maximum likelihood estimates [*Aldrich*, 1997]. To assess the quality of fitting theoretical models to the experimental data, the symmetric mean absolute percentage difference (SMAPD) was calculated according to Eq. (3.5). For each directional radiance time series, the SMAPD was computed for all four theoretical models. We chose the model with the least SMAPD as the best descriptor for the observed light field fluctuations.

The second quantity examined is the dispersion of the radiance time series data. A dimensionless number, known as the coefficient of variation (CV), is computed as

$$CV(\theta,\varphi) = \frac{\sigma_{L(\theta,\varphi)}}{\bar{L}(\theta,\varphi)} \tag{5.4}$$

where the coefficient of variation CV and the standard deviation σ_L are functions of the viewing direction, and $\bar{L}$ is the mean of the radiance time series $L(t)$.

The dominant frequency is the third quality for the characterization of the radiance fluctuations. The periodogram was first estimated based on the fast Fourier transform (FFT). It was then smoothed using the Parzen spectral window [*Priestley*, 1981]. The width of the window was taken to be one eighth of the record length, $N/8$. The spectral analysis partitioned the variance of the radiance sequence into its frequency-dependent components. The Nyquist frequency was 4.35 Hz. The dominant frequency f_p was

determined as the frequency where the variance was the maximum in the computed power spectral density (PSD).

One-way analysis of variance (ANOVA) was used to test whether there were significant differences between the dominant frequencies of directional radiance in different directions.

The PDF, variance and periodicity were also computed for the irradiance and average cosine time series using the same methodology detailed above.

5.2.3. Monitoring of Other Environmental Conditions

The sea waves were measured in our study using the Riegal linear scanning laser altimeter deployed on the research platform of R/P *FLIP*, at locations about two kilometers away from the camera deployments from R/V *Kilo Moana*. The laser altimeter measured the distance to the ocean surface from the fixed boom height and provided the wave spectra and wave statistics including the significant wave height and wave frequency. The laser altimeter sampled at a frequency of 50 Hz. The measurement accuracy is ±25 mm and the measurement resolution is ±25 mm. The sea surface height spectra were computed via a fast Fourier transform. The dominant or peak wave frequency, f_p, is the frequency corresponding to the frequency band with the maximum value of spectral density in the nondirectional wave spectra.

The wave slope spectra were also computed from the measured wave height spectra based on the linear dispersion relationship for deep waters [*Cox and Munk*, 1956]

$$S_{xy}(f_i) = \frac{(2\pi f_i)^4}{g^2} S_{\zeta\zeta}(f_i) \tag{5.5}$$

where $S_{\zeta\zeta}(f_i)$ is the wave height frequency spectrum, f_i is the frequency and g (unit: m s^{-2}) is the gravitational acceleration. The dominant frequency of the wave slopes was determined as the frequency with maximum variance in the spectra.

We calculated the solar zenith angle (SZA), θ_s, from the geophysical coordinates and the time of observation [*Reda and Andreas*, 2004]. In Pacific Ocean, θ_s was generally limited to < 30° while the water column was profiled. For the Santa Barbara Channel experiment, θ_s was between 40° and 50°.

In the following, we present specific results and findings from the primary data sets, which were collected under relatively large surface waves, together with a synthesis of all available radiance data from our experiments.

5.3. Results

5.3.1. Example Data of Wave-disturbed Radiance Distribution

The per-pixel radiance distribution is first illustrated in Figure 5.2a based on the measurement made under a relatively plane sea surface off the Scripps Institution of Oceanography pier. The image center corresponds to the zenith (θ = 0°). The zenith angle increases linearly toward the peripheral of the image, where the zenith angle is 90°. The azimuth angle is given relative to the position of the sun with the top of the image corresponding to the sun's azimuth angle, i.e. φ = 0°, and the azimuth angle increments clockwise. The bright circular region in the central part of the image roughly represents the Snell's window or Snell's cone. The above-water scene including the sky and the pier

is refracted into Snell's window. The region beyond the critical boundary at $\theta_{cr} = 48.6°$ is much dimmer, largely representing the internal reflections. The measurement under an ideally plane sea surface like this example is reminiscent of the mean light field as assumed in plane-parallel theory.

An example downwelling radiance distribution measured below a disturbed sea surface is presented in Figure 5.2b. This radiance distribution is representative of the light field under relatively large sea waves in the Pacific Ocean. In contrast to the level sea surface case, the wave-disturbed radiance field shows no definite boundary for the Snell's window. Rather, some dark bands (low radiance) and bright bands (high radiance) appear alternatively, near the otherwise clear Snell's boundary. The dark area likely represents the total internal reflection and/or shadows of wave facets. The relatively bright bands are a result of refracted transmission of skylight. Note that the radiance images are specially chosen for this demonstration, where the refracted sun is approximately aligned with the initial azimuth ($\varphi = 0°$). More generally, the brightest light spot(s) may or may not lie in the initial azimuth direction as the sun is refracted by the wavy sea surface.

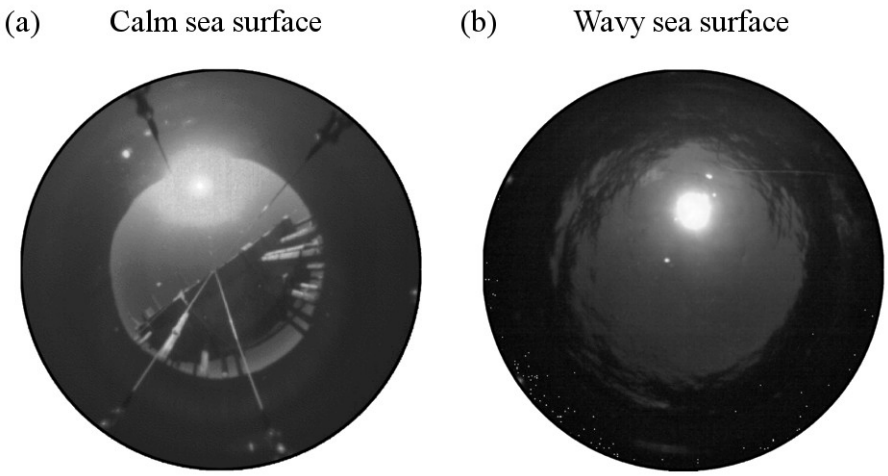

Figure 5.2 The radiance distribution in near-surface sea water under clear skies. (a) Smooth sea surface. This image was taken at the Scripps Institution of Oceanography Pier, La Jolla, California, on January 25, 2008. (b) Wavy sea surface in the Pacific Ocean off Hawaii (17°38.5' N, 156°34.7' W). The image was captured on September 3, 2009, 20:40 UTC; 4.4 m below sea surface; solar zenith angle θ_s = 27.5°, azimuth angle φ_s = 108.9° (relative to the true north); wind speed U_{10} = 10.6 m s^{-1}, wind direction 83°; significant wave height 2–3 m.

The radiance images have a nominal spatial resolution of the sea surface which is determined by the sensor position below sea surface, the viewing direction, the subtended solid angle of the pixel, and the sea surface topography being sensed. As a first approximation, the sea surface patch nominally resolved by an active pixel (i, j) can be estimated as

$$A_{ij} = \Omega_{ij} \cdot \left[\frac{z}{\cos\theta_{ij}} \right]^2 \tag{5.6}$$

where z is the sensor depth and Ω_{ij} is the corresponding solid angle. The image in Figure 5.2b represents the radiance distribution at a depth of about 4.4 m, and by Eq. (5.6) the

pixel viewing the Zenith receives light through a sea surface area of $A \approx 9$ cm^2, roughly as a square with side length of 3 cm. In the zenith angle of 60°, the pixels actually look at $A \approx 36$ cm^2. These length scales are much larger than capillary waves, whose wavelengths Λ are shorter than 1.73 cm [*Young*, 1999].

Figure 5.3 demonstrates four subsets of time series, each describing the fluctuating radiance in one specific direction. These data are extracted from the same data sets as Figure 5.2b in the Pacific Ocean, where the surface waves were about 2.5 m high and the sky was free of cloud. The zenith angle of the sun after the specular refraction in water was at $\theta_{sw} = 20°$. Radiance $L(\theta = 0°)$ refers to the light coming from the zenith (Figure 5.3a). Figure 5.3b, Figure 5.3c and Figure 5.3d describe the fluctuating radiance along the principal plane of the Sun at differing zenith angles. The directions $\theta = 45°$ and $\theta = 60°$ bracket the critical boundary of the Snell's window. Visual assessment indicates two pronounced features in these radiance sequences. One is the large amplitude variations in the direction of the refracted sun; the radiance in directions of $\theta = 0°$, $\theta = 20°$, $\theta = 45°$ and $\theta = 60°$ has the maxima to minima ratios of about 15, 700, 25 and 10, respectively. In contrast, the same ratios for the downwelling plane irradiance time series and the downwelling scalar irradiance time series are only about 10 and 9 respectively (not shown in the figure). The second feature is that these fluctuations are periodic, with superposed high frequency variability.

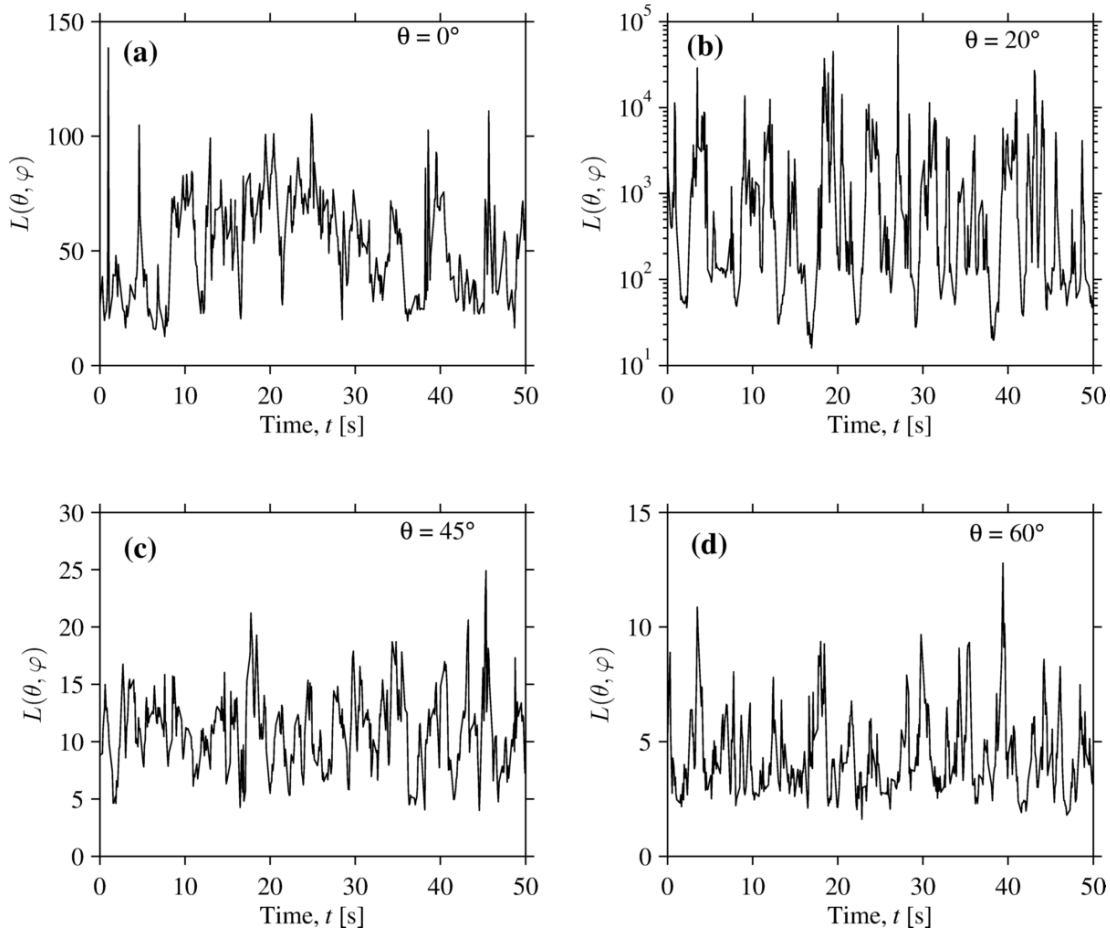

Figure 5.3 Time series of the directional radiance fluctuations (555 nm; $\mu Wcm^{-2}sr^{-1}nm^{-1}$) induced by surface waves under clear skies. The data sequences were selected from the principal plane $\varphi = 0°$ and in different zenith directions, of (a) $L(\theta = 0°)$; (b) $L(\theta = 20°)$ in log scales; (c) $L(\theta = 45°)$, and (d) $L(\theta = 60°)$. The raw data were collected at water depth of 4.4 m (±0.17 m), on September 3, 2009, 20:40 UTC, in the Pacific Ocean (17°38.5'N, 156°34.7'W), with solar zenith angle $\theta_s = 27.5°$. They are from the same data set as Figure 5.2b.

5.3.2. Probability Distribution of Fluctuating Radiance

The probability distribution for the same four radiance time series is shown in Figure 5.4. The directions and the skewness (Sk) and kurtosis (Kt) for each data sequence are given in each subplot. The data are asymmetrical about the mean and skewed towards higher radiance values. The skewness and kurtosis are particularly large in the direction close to the refracted sun ($\theta = 20°$). Among the four candidate models, the lognormal function is the best descriptor for the radiance measurements with SMAPDs of less than 16%. We have estimated the SMAPDs for all the radiance in 72×15 directions and found that more than 90% of the probability distributions of radiance fluctuations can be predicted by the lognormal model with SMAPDs less than 20% (Table 5.2). This phenomenon applies to all our radiance time series measurements from the Santa Barbara Channel and the Pacific Ocean off Hawaii.

For comparison, Figure 5.5 presents the example PDFs for the downwelling plane irradiance and scalar irradiance data (see Eq. (4.1) and Eq. (4.2)). One noticeable feature is that the skewness and kurtosis for the integrated irradiance data are far smaller than those of radiance in Figure 5.4. As with radiance, our measurements of the plane irradiance and scalar irradiance can both be best described by the lognormal function (Figure 5.5). For example, the SMAPDs of 31%, 16%, 23% and 73% are determined between the candidate models (Weibull, lognormal, normal and extreme distribution) and the empirical distribution of plane irradiance data in the Pacific Ocean, respectively (Figure 5.5a). SMAPDs of 20%, 8%, 17% and 80% are found between four model-data comparisons for the scalar irradiance (Figure 5.5b). Our measurements in the Santa Barbara Channel indicate that the lognormal model is applicable to both the radiance time

series (figure not shown) and the irradiance time series (Figure 5.5c and Figure 5.5d). Specifically, SMAPDs of 10%, 21%, 9% and 188% are found when fitting the downwelling plane irradiance (Figure 5.5c), and SMAPDs of 114%, 19%, 17% and 558% are found for the scalar irradiance model fitting (Figure 5.5d).

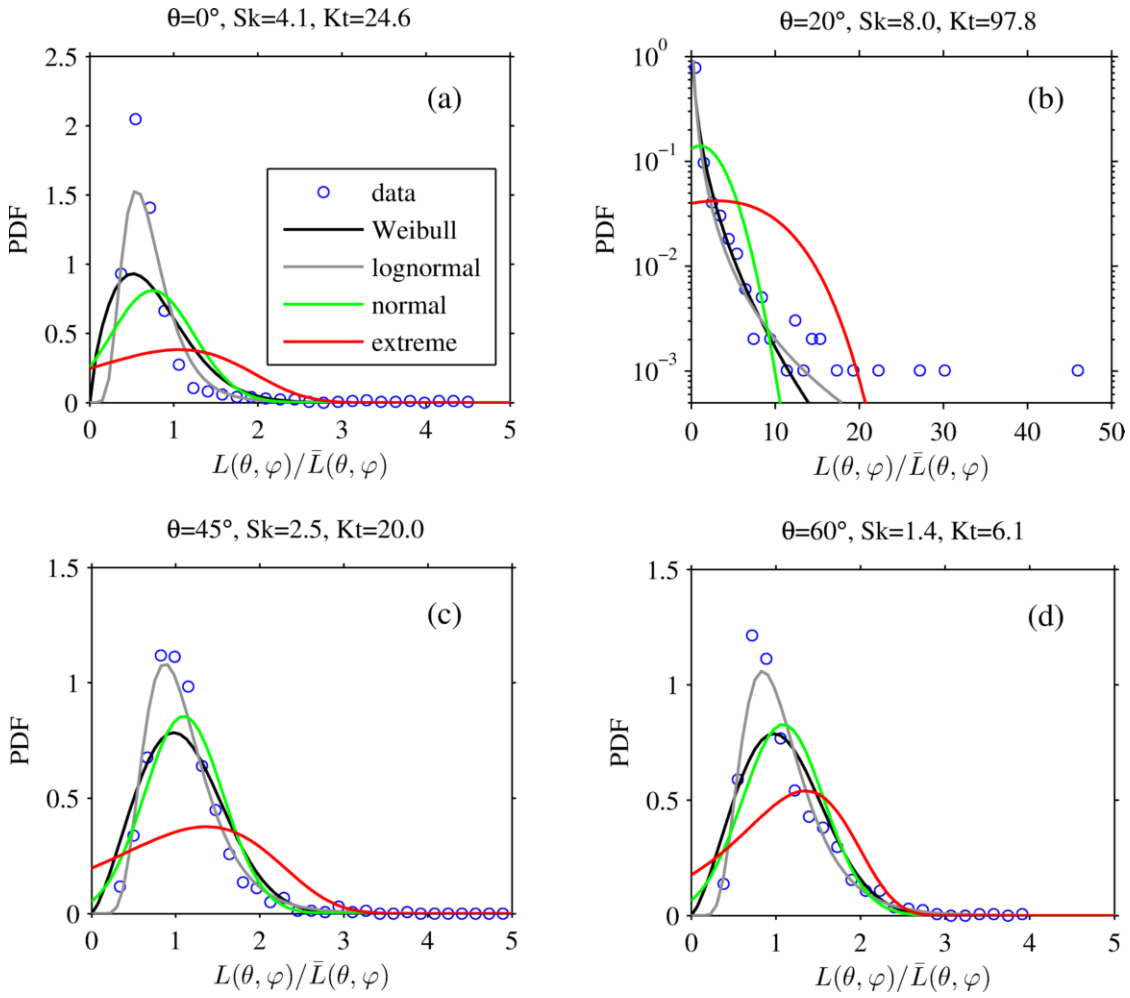

Figure 5.4 Probability distributions of directional radiance data (555 nm) under clear skies. Four radiance sequences are selected from the same half vertical plane of $\varphi = 0°$, but in different zenith directions θ. The four data sets correspond to the four subplots of Figure 5.3; and a total of 1000 data frames are used for each fitting. Four subplots use the same legends as shown in (a), where the empirical probability distribution data are denoted as open circles.

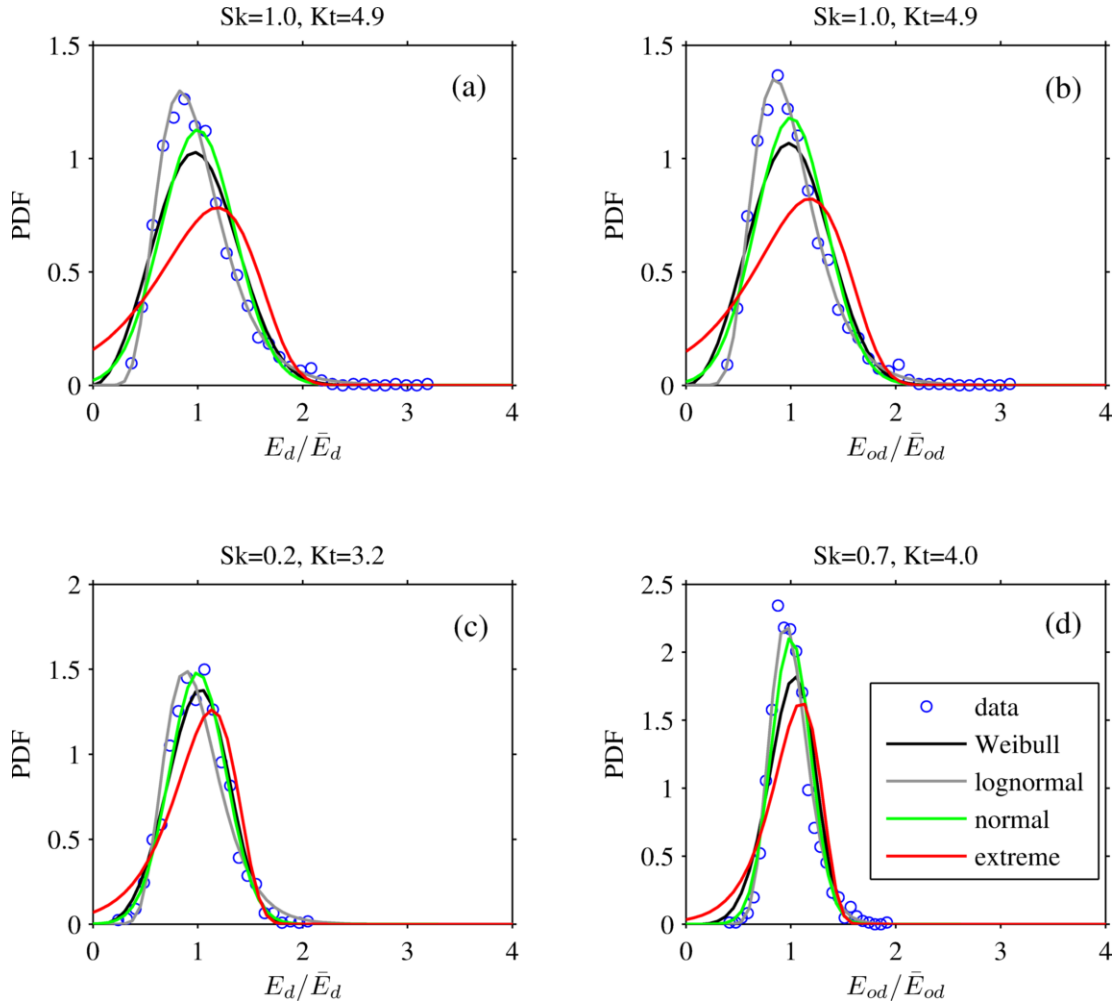

Figure 5.5 Probability distribution of irradiance (555 nm) fluctuations under clear skies. Example data (a) and (b) are from the Pacific Ocean; same data are used as Figure 5.3; water depth 4.4 m; solar zenith angle θ_s = 27.5°. Examples in (c) and (d) represent the case in the Santa Barbara Channel (September 15, 2008, 22:10 UTC); water depth 1 m, solar zenith angle θ_s = 44°. All subplots use the same legends as shown in panel (d), where the empirical probability distribution data are denoted as open circles.

Table 5.2 Mean absolute percentage errors between the modeled and measured directional radiance and integrated irradiance (at 555 nm).

Experiment site	Light field measurement	Probability distribution function			
		Weibull	Lognormal	Normal	EVD
Pacific Ocean (September 3, 2009, 20:40 UTC)	$L(0°,0°)$	10%	9%	8%	14%
	$L(20°,0°)$	3%	2%	6%	7%
	$L(45°,0°)$	36%	16%	26%	123%
	$L(60°,0°)$	15%	11%	12%	35%
	E_d	31%	16%	23%	73%
	E_{od}	19%	8%	17%	8%
Santa Barbara Channel (September 15, 2008, 22:10 UTC)	$L(0°,0°)$	7%	6%	8%	8%
	$L(20°,0°)$	5%	4%	8%	7%
	$L(45°,0°)$	5%	4%	7%	6%
	$L(60°,0°)$	8%	8%	7%	9%
	E_d	10%	21%	9%	188%
	E_{od}	114%	19%	17%	558%

5.3.3. Amplitude of Radiance Fluctuations

The coefficient of variation is illustrated as a function of the viewing zenith angle and azimuth angle in Figure 5.6. Figure 5.6a describes the variance of the radiance field in the open ocean off Hawaii, when the solar zenith angle is relatively high ($\theta_s = 27.5°$). Figure 5.6b illustrates the variance of the radiance field observed in the coastal water of the Santa Barbara Channel, at relatively low sun elevation ($\theta_s = 44°$) where the wind vectors differs as well.

The first feature to be noted is that the CVs vary over a wide range; they can be as low as 10%, and can also reach 1000% and higher. In contrast, the corresponding downwelling irradiance field only varies to a relatively small degree. We have calculated the CV = 36% for this Pacific Ocean downwelling plane irradiance data set and CV = 18% for the SBC downwelling plane irradiance data.

The second feature is the anisotropy of the relative variance distribution. The most variable radiance, with extremely high CVs, is clustered around the specularly refracted sun. For the Pacific Ocean measurement, the specular refraction of the sun is at $\theta_{sw} = 19.7°$ and $\varphi_{sw} = 0°$ (Figure 5.6a); for the Santa Barbara Channel data, the sun's position underwater after specular refraction is at $\theta_{sw} = 29.7°$ and $\varphi_{sw} = 0°$ (Figure 5.6b). This characteristic distribution pattern of extremely high CVs is simplified as the extreme-CV pattern (ECP), within which the CVs are higher than 200%. Figure 5.6a shows that the ECP with small SZA is largely within the Snell's window and only slightly elongated along the wind direction. The relatively large-SZA observation in Figure 5.6b generates an ECP running across the critical boundary of the Snell's window, which is obviously aligned with the wind direction.

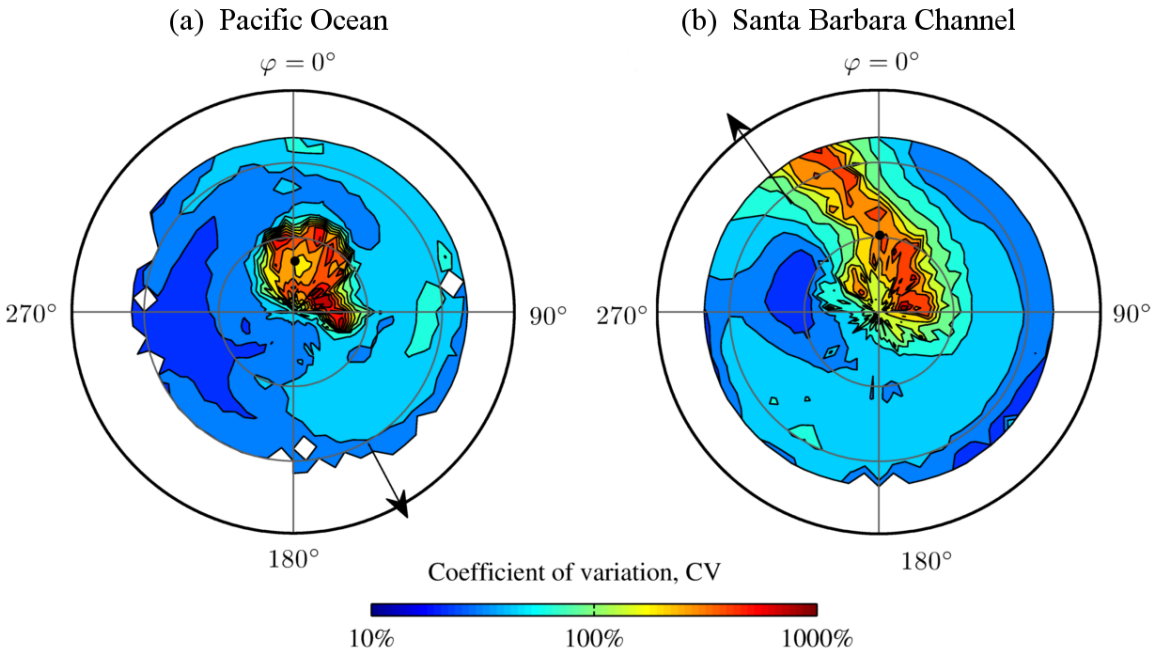

Figure 5.6 Contours of the coefficient of variation for the directional radiance (555 nm) under clear skies. (a) Pacific Ocean water off Hawaii; same data as Figure 5.2b, with θ_s = 27.5°, wind speed U_{10} = 10.6 m s^{-1}, wind direction 83° (relative to the true north). (b) Santa Barbara Channel, California (September 15, 2008, 22:10 UTC); θ_s = 44°; water depth 1 m; wind speed 7.2 ms^{-1}, wind direction 266°; significant wave height 1 m. The black arrows refer to the direction that the wind is blowing towards relative to the sun's azimuth (φ = 0°). The black dot indicates the location of the refracted sun θ_{sw} within plane-parallel water.

Within the ECPs, the coefficients of variation follow a bi-model pattern (BMP). This phenomenon is most obvious in the anatomy of CVs in Figure 5.7, in which the radiance time series is examined every 1° apart in the principal plane. The minimum CV is approximately located in the same direction with the specularly refracted sun underwater. The maxima of CVs are found in the proximity of the ECP's outermost boundary of CV = 100%. The width of the ECP (zenith difference of the boundaries in the principal plane) is generally less than 30°.

The spatial pattern of the maximum radiance is given in Figure 5.8, which describes the locations or possibilities of the occurrence of the maximum radiance in the hemispheric space. The maximum radiance is not always in the specular transmission direction of the sun below the wavy sea surface as predicted. A qualitative estimate about the possibility of occurrence of the brightest radiance can be made by the area density of the points. They tend to show up in directions other than the specular transmission direction of the sun, and to radiate further away from those directions. Comparison of the two subplots in Figure 5.8 suggests that the spatial pattern is associated with the solar zenith angle and the wind direction. When the sun is high (small SZA), the points are largely confined within the Snell's window (Figure 5.8a). The spatial pattern is not circular in shape; rather, it is slightly stretched along the wind direction. When the sun is lower (larger SZA), the distribution is very much elongated along the wind direction and can spread across the critical boundary of the Snell's window (Figure 5.8b).

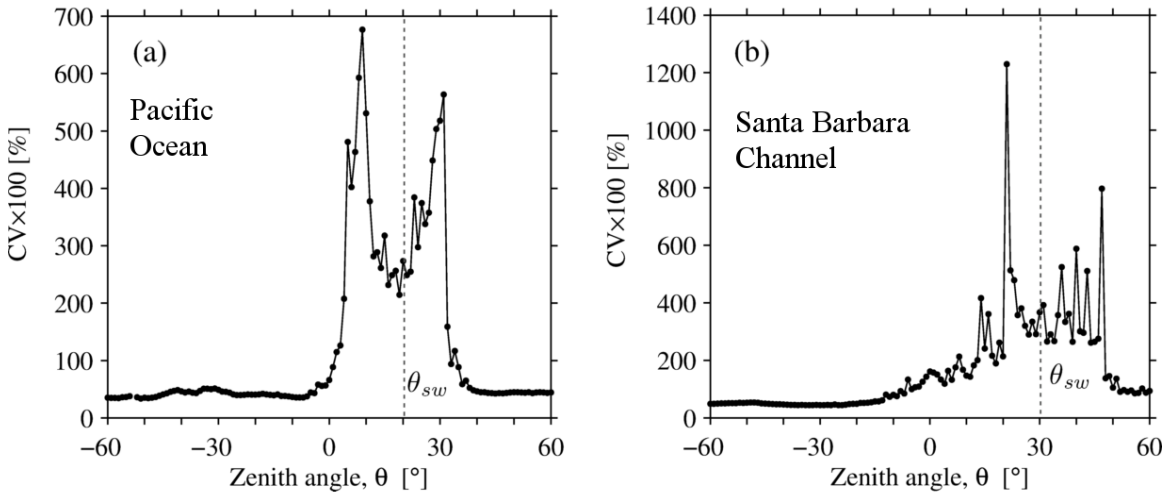

Figure 5.7 Coefficients of variation of directional radiance (555 nm) in the principal plane. (a) Pacific Ocean; the same data as Figure 5.6a. (b) Santa Barbara Channel; the same data as Figure 5.6b. The positive angles refer to the directions facing the sun in the principal plane (φ = 0°, denoted as solid dots). The negative angles identify the directions opposite to the sun (φ = 180°) in the perpendicular plane. The vertical dot lines identify the refracted sun's zenith underwater, $\theta_{sw} \approx 20°$ for the Pacific Ocean data and $\theta_{sw} \approx 30°$ for SBC data.

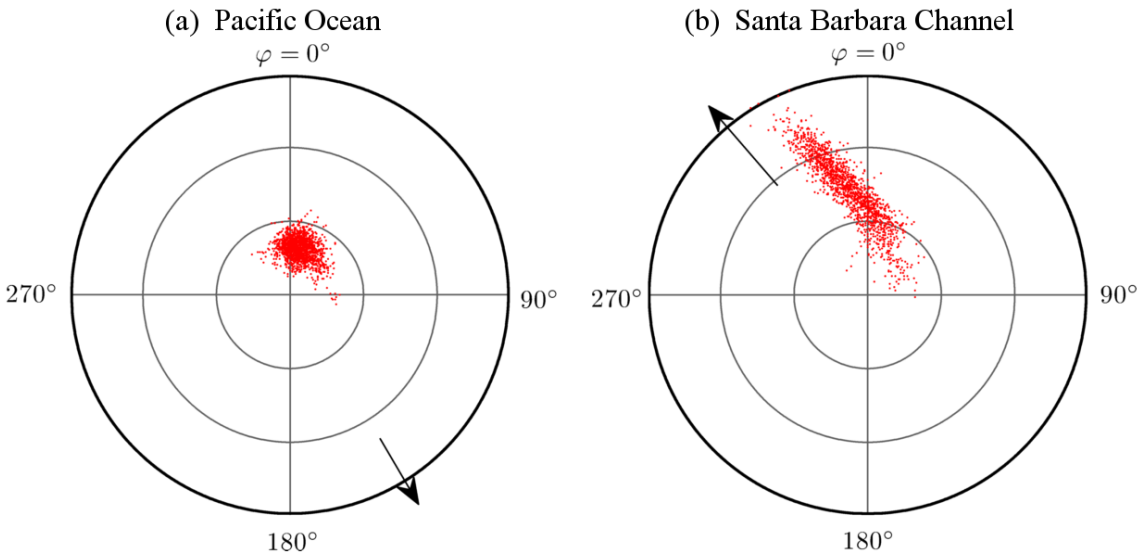

Figure 5.8 Distribution of the locations of the maximum radiance (555 nm) in the image plane. (a) Pacific Ocean example, the same data as Figure 5.6a. (b) Santa Barbara Channel, same data as Figure 5.6b. The black arrows refer to the directions the wind is blowing towards relative to the sun's azimuth ($\varphi = 0°$). The cross symbol "×" denotes the location of the refracted sun within plane-parallel water.

5.3.4. Periodicity of Radiance Fluctuations

The dominant frequency of the radiance fluctuations is not isotropic in the hemispherical space (Figure 5.9). A characteristic annular distribution pattern can be defined: for viewing directions of $\theta < 30°$, the radiance varies at lower frequencies; for directions of $30° < \theta < 60°$, the radiance fluctuates faster. This phenomenon is found in most of our observations at shallow depths; mean values and standard deviations were calculated and are illustrated in Figure 5.10.

ANOVA analysis shows that the difference in the mean of the dominant frequencies in two above-mentioned subregions is significant (Table 5.2); there is only one exception with the experiment numbered "249" (The 3rd data group in Figure 5.10), which was taken at great depths (13 m).

Figure 5.11a compares the dominant frequencies between the radiance fluctuations and the sea waves. The dominant frequencies of the sea wave heights are smaller than those of the radiance field. The dominant frequencies of the wave slopes are only slightly higher than those of the radiance fluctuations within the regions of 30°-60° (Figure 5.11b). For either case, variation in the radiance correlates with the wave field positively ($p < 0.05$). The dominant frequencies of the radiance fluctuations are much faster than the downwelling plane irradiance and scalar irradiance fluctuations (Figure 5.11c and Figure 5.11d).

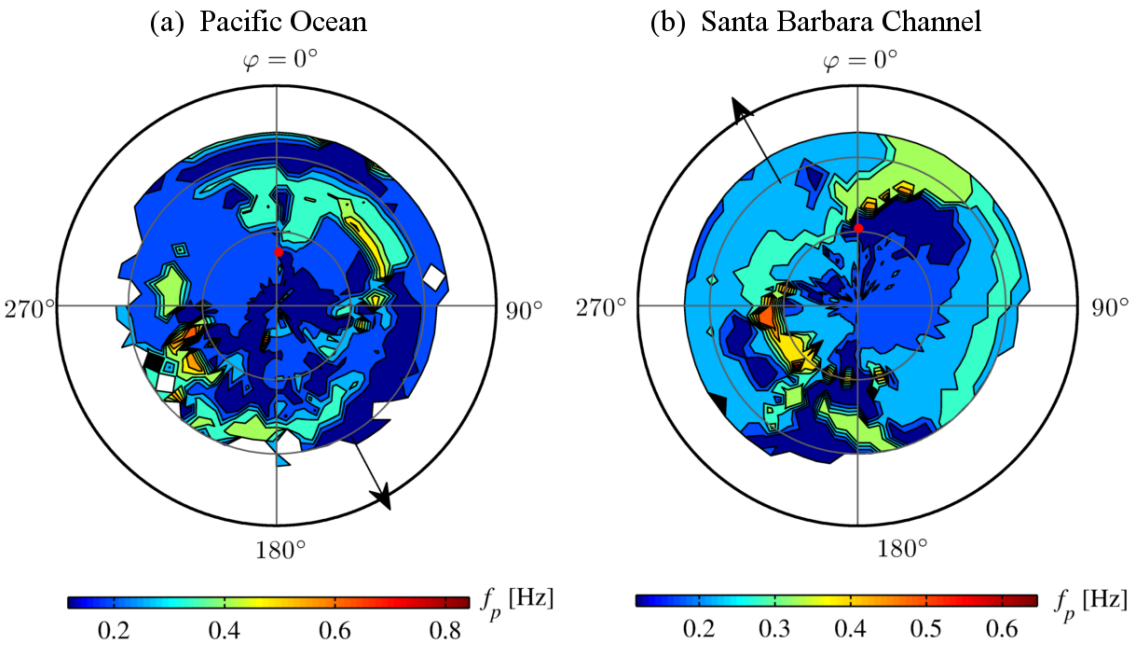

Figure 5.9 Contours of the dominant frequency of fluctuating radiance (555 nm) under clear skies. (a) Pacific Ocean water off Hawaii; same data as Figure 5.6a ; the mean frequencies of $\theta < 30°$ and $30° < \theta < 60°$ are 0.21±0.07 Hz and 0.28±0.12 Hz, respectively. (b) Santa Barbara Channel; the radiance field (same as Figure 5.6b); the mean frequencies of $\theta < 30°$ and $30° < \theta < 60°$ are 0.21±0.06 Hz and 0.26±0.08 Hz, respectively. The black arrows refer to the directions the wind is blowing towards relative to the sun's azimuth (φ = 0°). The red dot indicates the location of the refracted sun within plane-parallel water.

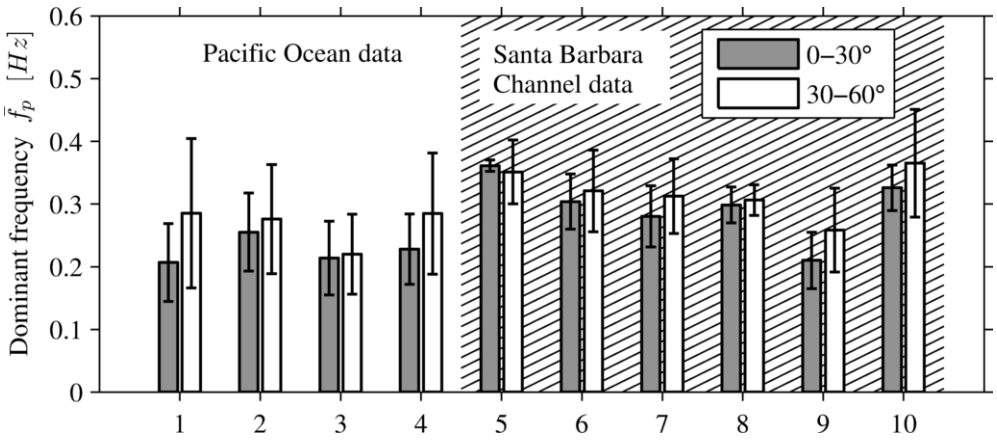

Figure 5.10 Box plot of the mean dominant frequencies for the sub-regional directional radiance. Each data group represents the frequencies for directions of from zenith directions $\theta = 0°$ to 30°, and from $\theta = 30°$ and 60°, respectively. The error bar describes the standard deviation of the dominant frequencies in each sub-region. All data groups correspond to the data described in Table 5.1.

.

Table 5.3 Analysis of variance for the dominant frequencies in two subregions of viewing directions of from 0° to 30° and from 30° to 60°.

Station No.	SS_{total}	MS	df	*F*-ratio	*p*
243†	5.944	0.871	526	96.5	0
246†	2.866	0.053	492	9.26	0.0025
249†	1.668	0.004	442	1.09	0.296
267†	3.415	0.393	484	62.9	<0.001
650-1‡	0.794	0.014	582	10.7	0.001
650-2‡	1.831	0.042	582	13.5	<0.001
650-3‡	1.873	0.150	582	50.8	0
650-4‡	0.422	0.008	582	11.9	<0.001
750‡	2.227	0.338	582	104.3	0
953‡	2.755	0.222	582	50.9	<0.001

† Data obtained in the Pacific Ocean off Hawaii in 2009.

‡ Data obtained in the Santa Barbara Channel, California in 2008.

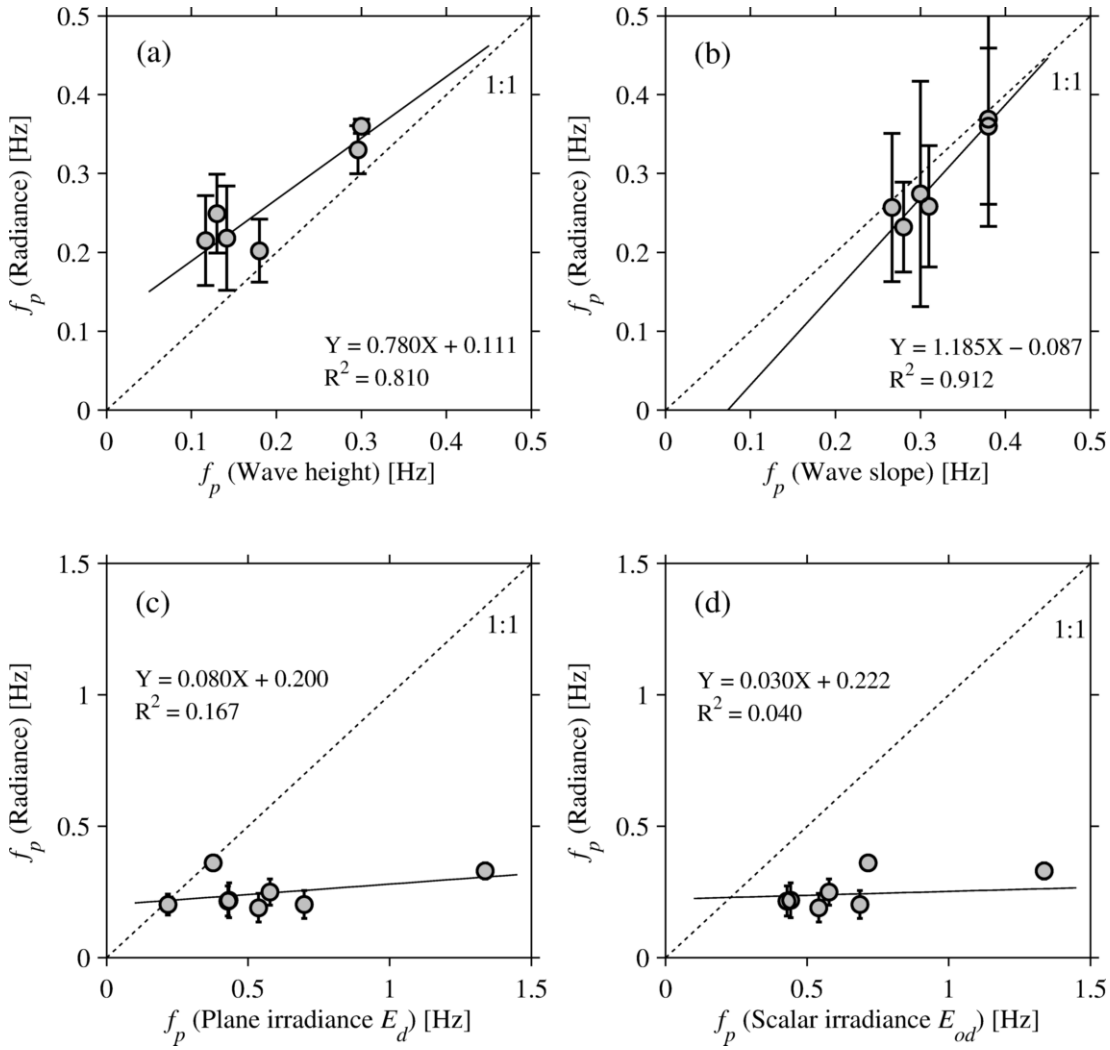

Figure 5.11 Comparison of the dominant frequencies of fluctuating radiance with other parameters. (a) Wave height field. (b) Wave slope field. (c) Downwelling plane irradiance. (d) Downwelling scalar irradiance. The data were obtained from the Pacific off Hawaii in 2009 and the Santa Barbara Channel in 2008. The dominant frequency of radiance for each deployment is evaluated by averaging over the directions between 0° and 30° in zenith angle, except for (b) which has employed the mean value for directions between 30° and 70°.

5.3.5. Downwelling Average Cosine

The average cosine is the average value of the cosine of the polar angles of all the photons contributing to the downwelling radiance field. In Figure 5.12a, the coefficient of variation of the downwelling average cosine is plotted as a function of the solar zenith angle. These observations represent the light field within the first 5 meters below the sea surface. Some data measured with the self-contained radiance camera from R/P *FLIP* over short duration are also included. A slowly increasing trend with the solar zenith angle is discernible. The coefficient of variation for the average cosine barely exceeds 5% within the near-surface sea water environment. These data are satisfactorily fitted with a function of CV = $-0.084 \times \cos\theta_{sw} + 0.098$, $R^2 = 0.443$, $p < 0.001$, N = 34, where θ_{sw} is the solar angle in water estimated by the Snell's law as $\theta_{sw} = \text{asin}(\sin\theta_s/1.34)$. According to our measurements, the standard deviation of the downwelling average cosine increases with SZA (Figure 5.12b); it can be fitted with the following function, STD = $-0.047 \times \cos\theta_{sw} + 0.060$, $R^2 = 0.298$, $p < 0.003$, N = 34. This SZA-dependency can be well accounted for by its two contributors: the mean value of the downwelling average cosine which decreases with the solar zenith angle (Figure 4.7) and the variance of $\bar{\mu}_d$ which generally increases with the solar zenith angle (Figure 5.12b).

The dominant frequency of the downwelling average cosine correlates with the radiance and the sea waves positively and significantly with $p < 0.05$ (Figure 5.12b, Figure 5.12c and Figure 5.12d).

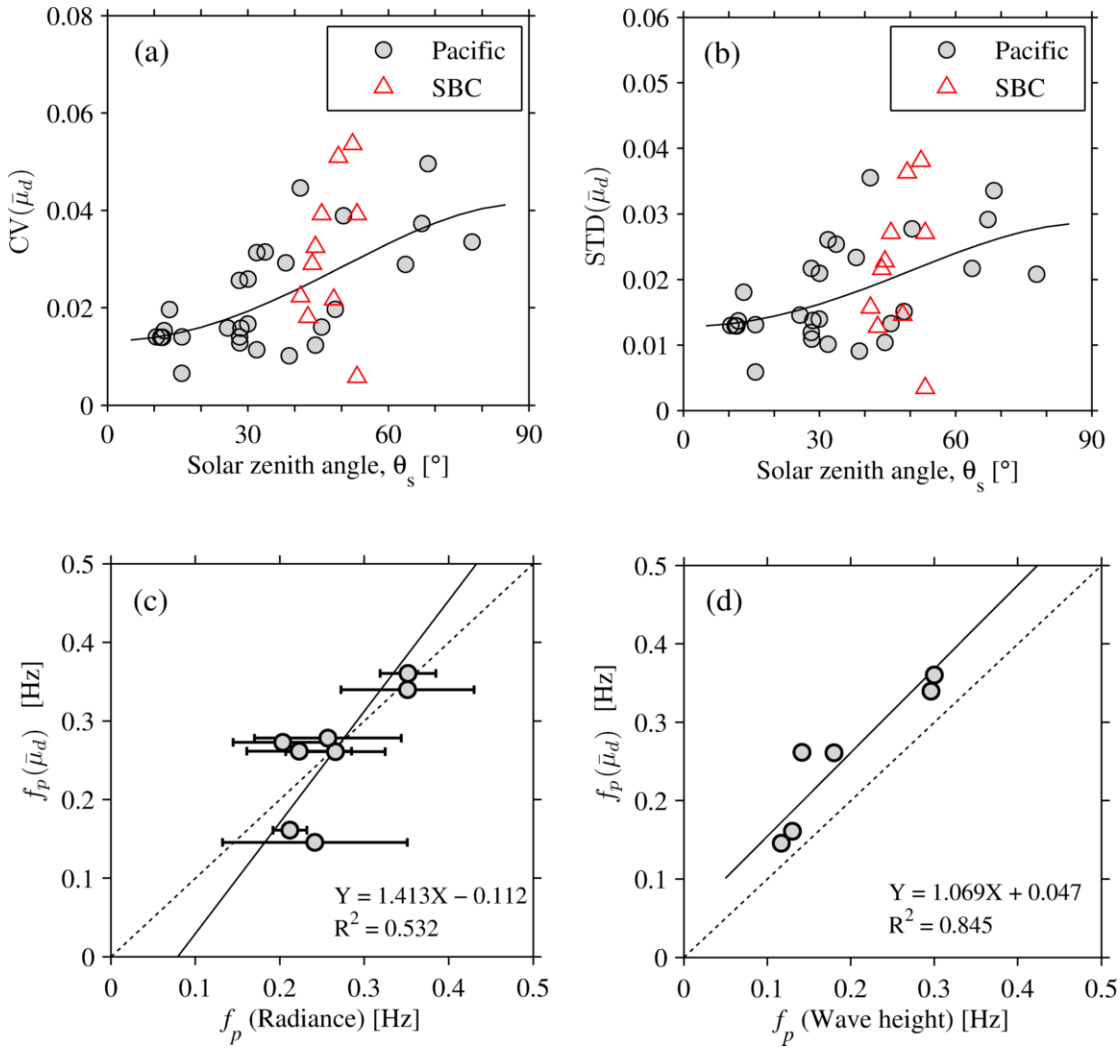

Figure 5.12 A summary of the variation of the downwelling average cosine (555 nm) under clear skies. (a) Coefficients of variation for the time series of downwelling average cosine as a function of the solar zenith angle θ_s. The curve represents a model fitting (see details in the text); the SBC data (represented as "Δ") are not involved in this fitting. (b) Standard deviation of the average cosine versus solar zenith angle. The curve represents a model fitting (see details in the text), which excludes the SBC data. (c) Dominant frequencies between radiance and the average cosine; the same radiance data as Figure 5.11a are used. (d) Dominant frequencies of the downwelling average cosine versus the wave height.

5.3.6. Depth Evolution of Radiance Variability

Figure 5.13 and Figure 5.14 illustrate the depth evolution of the radiance field variability based on radiance time series measurements at Station 650 in the Santa Barbara Channel (see Table 5.1). Four deployments were performed within 35 minutes; during the experiment a slight increase in the wind speed, significant wave height and solar zenith angle were observed.

At every measurement depth the distribution pattern of extreme CVs (>100%) for the radiance field is largely stretched along the wind direction and clustered around the direction at θ_w (Figure 5.13a). Overall, the coefficient of variation of the radiance variability decreases with water depth. An exceptional increase is recorded at depth of 2.3 m, where the radiance variability becomes more intense in some directions and the extent of ECP also becomes wider. One possible explanation is that this location is close to the focal depth of the incident light. The spatial distribution of the viewing directions where the hemispherical radiance is the maximum (Figure 5.13b) is very similar to the extreme CV patterns, including the orientation and extent.

Figure 5.14 summarizes the periodicity of the light field variability with water depth. The variation of the dominant frequency of the radiance (for viewing directions between 0° and 30°, and between 30° and 60°) with water depth is not as significant as the downwelling average cosine and the downwelling plane irradiance. In particular, the dominant frequency of plane irradiance decreases with depth until it coincides with that of the radiance field; this observation is in agreement with Figure 5.11c.

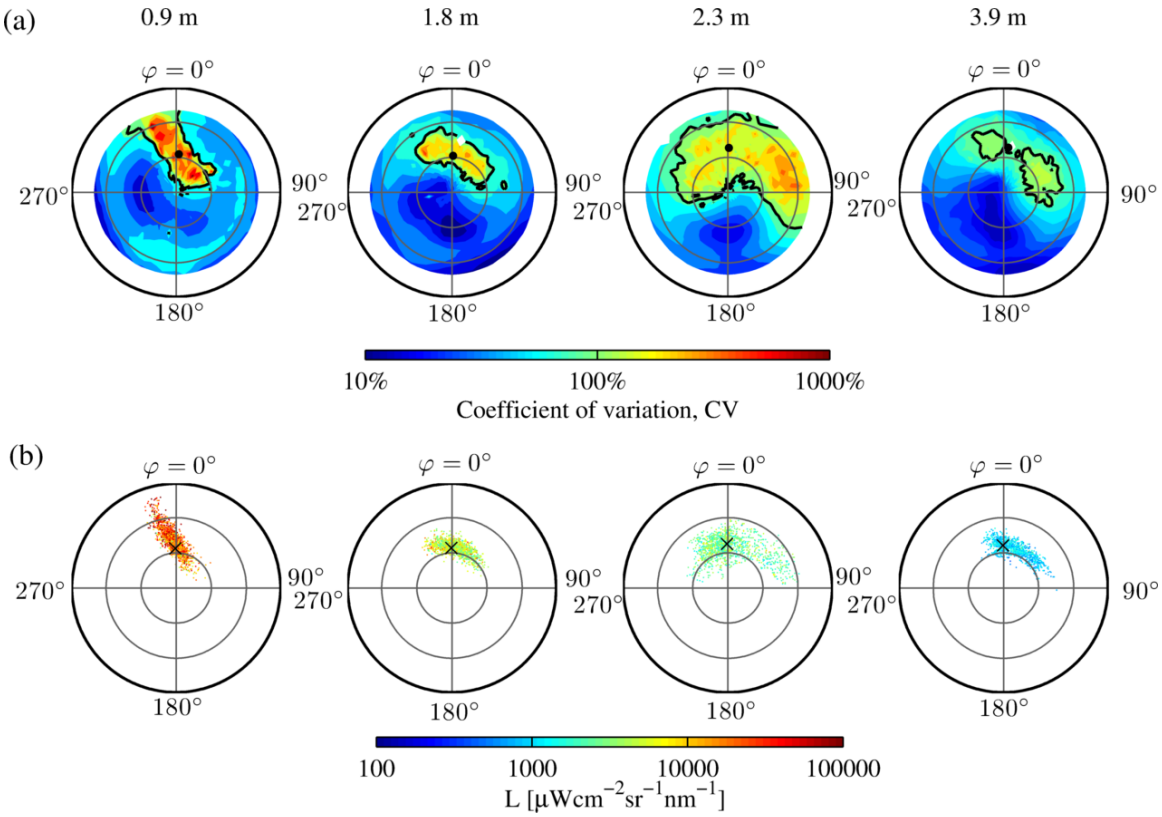

Figure 5.13 Evolution of the radiance field variability with water depth. (a) Coefficient of variation for the radiance field. The contour at level CV = 100% is highlighted by thick lines; the solar zenith in water θ_w is marked with a black dot. (b) Distribution of locations of the maximum radiance derived from 1000 data frames, where the solar zenith in water θ_w is marked with a black cross. The radiance variability at four measurement depths are derived from experiment 650-1, 650-2, 650-3 and 650-4, respectively, as described in Table 5.1.

.

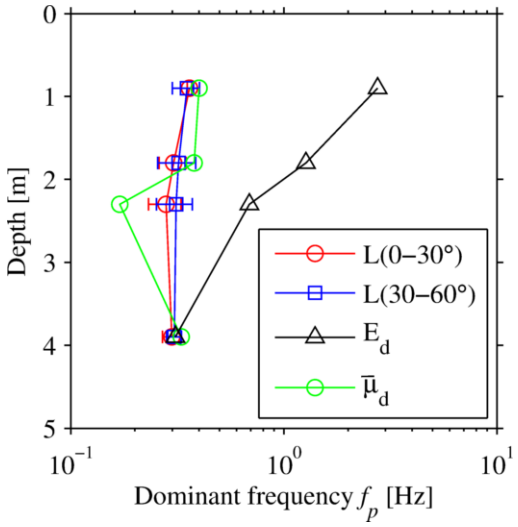

Figure 5.14 Depth evolution of the dominant frequency of the light field variability. The same data sets as Figure 5.13 are used.

5.4. Discussion

The wave disturbance of radiance distribution is obvious in the spatial structure of the radiance field (Figure 5.2), where the dark bands in the vicinity of the critical boundary principally represent the internal reflections and/or shadows of neighboring wave facets. Quantification of the measured radiance fluctuations shows that the variability of the radiance distribution below the sea surface is substantial. The amplitude and periodicity of radiance fluctuations depend on the viewing directions (Figure 5.6 -Figure 5.9), and the wave-disturbed radiance distribution is correlated to the surface wave field (Figure 5.8, Figure 5.11 and Figure 5.12).

The presented data are highly resolved with respect to angle (0.25° FOV half angle), which, to our best knowledge, exceed all previously reported measurements [*Darecki et al.*, 2011; *Mullamaa and Nikolayev*, 1972; *Nikolayev and Yakubenko*, 1978; *Sabbah and*

Shashar, 2006]. This small receiving angle is probably still insufficient to fully resolve the smallest capillary waves (wavelength $\Lambda < 1.75$ cm) according to Eq. (5.6), which together with the gravity waves may contribute to the observed variations in the radiance distribution.

For example, the small gravity waves generate parasitic capillary waves on their forward face due to their large curvature and vortices [*Ebuchi et al.*, 1987; *Fedorov and Melville*, 1998; *Hwang*, 1999; *Longuet-Higgins*, 1963, 1995]. These capillary waves are generally phase-locked with these steep gravity waves [*Hwang*, 2002]. Both may be further modulated by the background longer waves. The periodic structure of the mean square slopes (over wavelength range 0.004-0.104 m) along the profile of background waves is obvious [*Hwang*, 1999]. The observed systematic frequency deviations between the radiance field and the wave field (Figure 5.11c and Figure 5.11d) are partly due to the modulation phase shift. Apart from this frequency discrepancy, our observations have shown that the average frequencies of radiance fluctuations and the dominant frequencies of sea waves are positively correlated [also see *Sabbah and Shashar*, 2006].

The identified angular maxima in the coefficient of variation (Figure 5.6) are suggestive of the highest dispersion of the radiance data in the hemispheric space. At these shallow depths, these most intense fluctuations of directional radiance are most probably related to the "refracted" glitter spots of the sun, analogous to the well-known upward-reflected glitter of the sun on the sea surface. The number of the sun's refracted glitter spots appearing in the images is random, largely determined by the sea surface slopes [e.g. *Cox and Munk*, 1956]. The alignment of the extreme CV patterns with the wind directions implies such a connection between the wave field and the light field.

According to *Cox and Munk* [1956], the glitter pattern of the refracted sun shrinks as the sun rises and expands when the sun sets. Two examples in Figure 5.6a and Figure 5.6b represent the high-SZA case and the low-SZA case, respectively. The bi-model pattern of the coefficient of variation in the principal plane (Figure 5.7) and the elongated pattern in the horizontal plane are specific examples of the anisotropic directionality. The bi-model pattern derived from our full radiance field measurements confirms a recent report [*Darecki et al.*, 2011]. The mean radiance in the direction of specular refraction of the sun is supposed to be the highest of all [*Jerlov*, 1976], which brings down the dispersion of the radiance observations. Away from the direction θ_w, the mean underwater radiance drops sharply; so occurrence of the intense radiance impulses would tend to enhance the data dispersion.

For the log-normal distribution, the coefficient of variation is positively proportional to the variance [*Limpert et al.*, 2001], $CV = (\exp(\sigma^2) - 1)^{1/2}$. The extreme CV pattern of the radiance field therefore also quantifies the distribution of its absolute variance. The finding of a best-fit lognormal model for the downwelling plane irradiance in near-surface water is generally in agreement with *Gernez et al.* [2011].

The observed annular periodicity difference in the radiance field (Figure 5.9 and Table 5.3) is generally consistent with everyday experience of a swimmer when looking at the water surface from underneath. A tentative explanation is the effect of the internal reflection off the wavy surface. As shown in Figure 5.1, the internal reflection occurs both within and beyond the average Snell's boundary when the plane sea surface is ruffled by waves, which adds to the radiance variability in these directions. Since the slopes of surface waves are rarely greater than 30° [*Cox and Munk*, 1956], a first estimate

for the extent of the Snell's boundary is between viewing directions of 18.6° and 78.6° [*Sabbah and Shashar*, 2006]. With the decrease of SZA, the sun tends to be refracted into positions closer to the critical boundary. When the waves pass by, both the sun and the Snell's window can be dynamically translated according to the sea surface topography. The variance of the average cosine will consequently be enlarged (Figure 5.12b).

The radiance fluctuations evolve with the water depth [also see *Sabbah and Shashar*, 2006; *Yakubenko and Nikolayev*, 1978]. According to Eq. (5.6), the nominal sea surface area intercepted by the radiance sensor increases with water depth. Within the first 30 m below sea surface, the effective surface area is still in the range of several decimeters, where the capillary waves and short gravity waves dominate. But the number of glitter spots might have been strongly reduced due to scattering along the path from the sea surface to greater depths. In another words, the variance patterns like the bi-modal patterns found at shallower depths would probably not exist at greater depths. This may explain why the historical luminescence data of *Mullamaa and Nikolayev* [1972] and *Nikolayev and Yakubenko* [1978] showed maximum CVs in directions other than the refracted sun. Their data were retrieved from depths of ~10-17 m in waters much more turbid than the SBC and the Pacific waters in our experiments.

The instrumental deployment scheme described in my study was unable to exactly restraint the light sensor at a fixed position, and the instrument package thus deployed beneath the sea surface was not an immobile platform. The sensor movement in the spatial domain could result in Doppler smearing of wave number and frequency of many oceanographic processes [*Rudnick and Cole*, 2011]. Mobility of a light sensor may have an effect on the recordings of the underwater light field fluctuations for both its

magnitude and frequency [*Yakubenko et al.*, 1978]. For example, the tethering float on the sea surface does not merely move up and down as the wave trains pass by but more likely describes a circle, though not precisely closed [*Sverdrup et al.*, 1942]. This kind of spatial shift and its resulting velocity cannot be exactly determined but are reasonably small considering the dimension of the dominant surface waves and the fast sampling rate of the camera. Another type of drift of the tethered instrument package is associated with the free drift of the vessel, which is dragged by both the ocean currents and wind stressing. In the North Pacific Gyre experiment (off Hawaii), it was found that the vessel drifted westwards at a speed of ~36 cm s^{-1} [*Zappa et al.*, 2012]. The resulting frequency shift in the underwater radiance fluctuations can be approximated by the following relationship [*Yakubenko et al.*, 1978],

$$f_{\max}^{V} = f_{\max}^{0}\left|1-\frac{2\pi f_{\max}^{wave}}{g}V\right| \qquad \text{(Hz)} \tag{5.7}$$

where $f_{\max}^{V}$ (Hz) is the dominant frequency determined by a light sensor moving at a horizontal speed V (m s^{-1}), $f_{\max}^{0}$ (Hz) is the dominant frequency determined by an immobile sensor, and $f_{\max}^{\text{wave}}$ (Hz) is the dominant frequency of the sea surface wave spectrum. For $f_{\max}^{\text{wave}}$ varying between 0.1 and 0.4 Hz and V = 0.36 m s^{-1}, the measured frequency of radiance fluctuations $f_{\max}^{V}$ will be smaller than the true frequency $f_{\max}^{0}$ by 2%-9%. This fact explains the lower frequency of measured radiance fluctuations than that of the surface waves in Figure 5.11b.

The instrument drift may have also affected and reduced the magnitude of the radiance fluctuations recorded in our experiments, but most likely to a very small extent [*Yakubenko et al.*, 1978].

The different behavior of the dominant frequencies of irradiance and radiance fluctuations (Figure 5.14, Figure 5.11c and Figure 5.11d) may be due to different contributing mechanisms. Many factors and mechanisms can contribute to the observed light field fluctuations, including light focusing by the wavy sea surface, differential light attenuation associated with the sea surface elevation and light transmittance at the surface, etc [*Snyder and Dera*, 1970; *Stramski and Dera*, 1988]. Among all these factors, the wave focusing effect is dominant in the dynamic process of irradiance fluctuations. To the first order, the radiance sensor receives light from a small sea surface patch. The radiance fluctuations may be more sensitive to the variations of the sea surface elevations. Quantitative information of the wave height's role in radiance field variability is unavailable, however. According to our results, the closeness of the dominant frequency between the radiance field (Figure 5.11a and Figure 5.11b) and surface waves and the slow variability of the dominant frequency of the radiance field with depth (Figure 5.14) suggest that the radiance fluctuations are a more direct indicator of the surface wave field than irradiance.

A possible inversion of the wave slopes from the spatial distribution of the maximum radiance (e.g. Figure 5.8) is implied. An inversion scheme for the wave slopes may be applied to the refracted sun's glitter pattern as follows

$$\begin{cases} \sin\alpha \tan\beta = \dfrac{-n_w \sin\mu \sin\nu}{n_w \cos\mu - \cos\theta_s} \\ \cos\alpha \tan\beta = \dfrac{-n_w \sin\mu \cos\nu + \sin\theta_s}{n_w \cos\mu - \cos\theta_s}, \end{cases} \tag{5.8}$$

where the wave slope β is the ascent of the slope and α is the azimuth of the ascent of the slope (clockwise from the sun); μ and v are the zenith angle and azimuth angle of a glitter

spot as recorded in the radiance image. The geometry assumed in Eq. (5.8) is the same as *Cox and Munk* [1956]. Test runs give the mean square slopes (MSS) much higher than the theoretical predictions from Cox and Munk's model. For example, a MSS of 0.113 rad^2 is derived from Figure 5.8a, while Cox and Munk predict a value around 0.06 rad^2 at a wind speed 10.6 m s^{-1}. This discrepancy suggest that the traditional Cox-Munk framework is likely insufficient to retrieve the whole range of wave slopes [also see *Zappa et al.*, 2012]. The measuring techniques based on light refraction can image much larger wave slopes [e.g. *Jähne et al.*, 1994; *Stotts and Karp*, 1982] than light-reflection techniques. On the other hand, some of the maximum radiance may represent the focused light or multiple-scattered sunlight between wave facets. We examined the maximum radiance data in the two spatial patterns (Figure 5.8a and Figure 5.8b) and found they have large dispersions (CV varies from ~60% to 100%), varying from $10^{3.5}$ $\mu Wcm^{-2}sr^{-1}nm^{-1}$ to $10^{5.5}$ $\mu Wcm^{-2}sr^{-1}nm^{-1}$. So the refracted glitter patterns as shown in Figure 5.8a and Figure 5.8b have incorporated some spots where we actually sensed the focused light. A thresholding scheme for the radiance values may be necessary in the future to estimate precisely the refracted glitter underwater.

5.5. Summary

The radiance field right beneath the wavy sea surface as lit by the sun is a dynamic environment. According to our measurements, variations in the directional radiance at shallow depths follow the lognormal distribution. Both the amplitude and periodicity of the radiance variation are directionally dependent. The occurrence of the extreme CV patterns is associated with the sea wave field and the sun's position. The annular

distribution of the dominant frequency suggests that some specific mechanisms like internal reflection at the critical angles dominate the radiance dynamics in those viewing directions.

The amplitude of the radiance variation can be much greater than that for the irradiance, and the variations in the radiance and irradiance fields also differ in their periodicities. The difference in the observed radiance and irradiance variation is relevant to the effective size of the field of view of a radiometer. The radiance field variability is likely more related to the surface wave elevations. The irradiance fluctuations are more dominated by the wave focusing effect; it is an integration of the radiance over all directions in the hemisphere, and wave focusing induces faster variability in the irradiance field.

The average cosine appears to be a good descriptor for the radiance field structure with regard to the periodicity. The coefficient of variation of the average cosine increases with the solar zenith angle, but rarely exceeds 10% in near-surface sea water. The comparison between the radiance field and the sea wave field is positive in terms of the dominant frequency.

This study puts emphasis on the radiance distribution variability based on measurements within the first 5 meters below sea surface. It will be interesting to test if the identified extreme CV patterns or the spatial distribution patterns of maximum radiance at shallow depths can be used to derive the distribution of the surface wave slopes. It is anticipated that the radiance dominant frequencies at depth may not be close to those of the surface waves, considering the light scattering effect along the optical path

and the enlarged patch areas of sea surface being perceived by the radiance sensor with depth.

Chapter 6. Variability in the Underwater Light Field: Wave-induced Light Field Fluctuations in Irradiance Depth Profiles

6.1. Introduction

The downwelling plane irradiance ($\mu Wcm^{-2}nm^{-1}$), is a key radiometric quantity in hydrologic optics related applications, and the characteristics of the mean irradiance profile are well documented [*Gordon*, 1989; *Jerlov*, 1976; *Kirk*, 1994; *Preisendorfer*, 1976; *Zaneveld and Spinrad*, 1980]. In the upper water column, the mean irradiance profile is the best fit to an exponential relationship assuming a level surface and a plane-parallel environment with no change in surface illumination over the measurement interval,

---

* This chapter is based on a coauthored manuscript: Wei, J., M. R. Lewis, R. Van Dommelen, C. J. Zappa, and M. S. Twardowski (2013); Wave-induced light field fluctuations in measured irradiance depth profiles; *Journal of Geophysical Research*, in revision. The contribution of the author of this study includes conceiving and implementing the study design, collecting and analyzing data, and writing of the manuscript. The coauthors helped with data analyses and manuscript preparation.

$$E_d(z) = E_d(0^-)\exp\left[-\int_0^z K_d(z')dz'\right] \quad (6.1)$$

where E_d at depth z (m; positive downwards) is related to the irradiance just below the sea surface ($E_d(0^-)$) by the diffuse attenuation coefficient $K_d(z)$ (m^{-1}). Variability in the diffuse attenuation coefficient relates directly to key biogeochemical properties of the upper ocean [*Morel and Maritorena*, 2001; *Xing et al.*, 2011].

The irradiance field in the near-surface water column is subject to fluctuations about the mean at varying time scales. Celestial motions cause hourly, daily, seasonal, and yearly changes in the incident irradiance and the subsequent irradiance underwater. These relatively long-term irradiance variations can be predicted to first order [e.g. *Gregg and Carder*, 1990; *Sathyendranath and Platt*, 1988]. In the presence of sea-surface waves however, the light refraction occurring at the fluctuating air-sea interface leads to a rapidly changing underwater light field. The wave-induced irradiance fluctuations are readily observable at time-scales of tens of milliseconds to several seconds [*Darecki et al.*, 2011; *Dera and Gordon*, 1968; *Dera and Stramski*, 1986; *Snyder and Dera*, 1970; *Stramski*, 1986a; *Stramski and Dera*, 1988; *Zaneveld et al.*, 2001b].

The vertical distribution of the light fluctuations, including the magnitudes, periods and spectral content, is of ecological significance. In general, over half of the integrated primary production takes place in the first 40 meters of the water [*Siegel et al.*, 1995] and the rapidly fluctuating light can potentially impact the growth rate, photosynthetic efficiency or chlorophyll pigmentation for certain species of planktonic alga [*Greene and Gerard*, 1990; *Quéguiner and Legendre*, 1986; *Stramski et al.*, 1993; *Walsh and Legendre*, 1983]. It may strongly influence endosymbiotic photosynthesis of corals inhabiting shallow reef habitats [*Nakamura and Yamasaki*, 2008]. For fish in the littoral

zone, their early life stages (comprising eggs, larvae and juveniles) respond to the varying light climate [*Stoll*, 2009]. Marine animals' vision is also sensitive to the spatial and temporal fluctuations of the light field [*McFarland and Loew*, 1983]. From a purely physical perspective, the fluctuating irradiance signals are related to, and theoretically could be used to infer, the characteristics of sea-surface wave field.

Determination of the statistical nature of the short-term fluctuations in the irradiance field relies on appropriate sampling strategies in rough seas. For example, field data in support of understanding the nature of the fluctuating underwater irradiance has been largely acquired with sensors fixed at a nominal depth in the ocean [e.g. *Darecki et al.*, 2011; *Dera and Gordon*, 1968; *Dera et al.*, 1993; *Gernez and Antoine*, 2009; *Gernez et al.*, 2011; *Gordon et al.*, 1971; *Hofmann et al.*, 2008; *Nikolayev and Yakubenko*, 1978; *Nikolayev et al.*, 1972; *Prokopov et al.*, 1975; *Stramska and Dickey*, 1998; *Stramski*, 1986a; 1986b; *Stramski and Dera*, 1988]. Such observations provide detailed information on the light field statistics at specific depths, but are operationally difficult to extend for complete statistics along the vertical in the upper layers of interest. In spite of the limitation, a clearer picture of light field statistics has been developed from these traditional methods. For example, the magnitude and frequency of irradiance fluctuations have been shown to be dependent on the solar angle, wind speed and cloudiness [e.g. *Walker*, 1994]. Theoretical investigation often starts with a simplified sea surface model [*Hieronymi et al.*, 2012; *Nikolayev and Khulapov*, 1976; *Schenck*, 1957; *Snyder and Dera*, 1970; *Zaneveld et al.*, 2001b]; more advanced models reconstruct the sea surface based on existing wave spectra [e.g. *McLean and Freeman*, 1996]. Apart from the simplification and some lack of realism, theoretical models play an important role in

interpretations of the irradiance fluctuations, and sometimes produce predictions that are consistent with field observations [e.g. *You et al.*, 2010]. The present knowledge of the statistics of the underwater light field is however limited, inasmuch as the dynamic light field varies in the temporal domain as well as the spatial domain and because of the difficulty in measuring the fluctuating field near the sea surface in particular, but more generally throughout the vertical.

In this study, the magnitude and frequency structure of irradiance fluctuations is characterized as a function of water depth under clear skies based on the irradiance depth profiles measured by a free-fall radiometer [*Lewis et al.*, 1986; *Waters et al.*, 1990]. One hypothesis is that the vertical profiles of irradiance may be used to quantitatively reconstruct a dynamic irradiance field for the upper water column such as observed from optical profiles taken from sensors either lowered from vessels at sea or collected from free-fall optical systems. In practice, fluctuations are usually filtered out as "noise" to estimate the diffuse attenuation coefficient as under a plane sea surface [*Mueller*, 2003] or multiple casts are carried out and the resultant data statistically averaged [*Voss et al.*, 2010; *Zaneveld et al.*, 2001b; *Zibordi et al.*, 2004a]. By extracting the statistics such as the dominant frequency and the coefficient of variation from irradiance depth profiles, the dynamic irradiance field induced by sea surface waves for the whole water column of interest can be deduced in both the spatial and temporal domain.

The irradiance depth profiles presented here are representative of sea environments with relatively large surface waves. The main objective is to interpret the fluctuations in the irradiance depth profiles as the superposition of surface wave focusing effects. We address the following questions: (1) What is a generalized model for the irradiance

fluctuations in the surface water? (2) How do the frequency and amplitude of the irradiance fluctuations vary with water depth? and (3) what are the implications of the derivations of the irradiance depth profiles under a disturbed sea-surface?

6.2. Theoretical Formulation for Wave Focusing

We start with a theoretical examination of the irradiance distribution under a wavy sea surface in the context of geometrical optics. We assume only the direct radiation from the Sun with zenith angle θ_s. The sea surface is modeled as a one dimensional sine wave,

$$\zeta = \frac{H}{2} \cdot \sin(kx - \omega t) \tag{6.2}$$

where the surface elevation, ζ (m), is defined in terms of the sea wave height, H (m), the wavenumber, k (rad m^{-1}), the horizontal position, x (m), the angular frequency, ω (rad s^{-1}) and time, t (s). For gravity waves (wavelength, $\Lambda > 1.73$ cm), the wavenumber k relates to the angular frequency according to the wave dispersion equation in deep waters [*Young*, 1999]

$$f = \frac{\omega}{2\pi} = \frac{\sqrt{gk}}{2\pi} = \sqrt{\frac{g}{2\pi\Lambda}} \tag{6.3}$$

where Λ (m) is the wavelength of sea waves, f is the temporal frequency (Hz or s^{-1}), and g is the gravitational acceleration (m s^{-2}). The water below the sea surface is initially assumed purely transparent to light, i.e., no absorption and scattering, and is infinitely deep. At time $t = 0$, there is direct illumination incident onto the sea surface, with solar zenith angle $\theta_s = 0°$. Snell's law is followed at the interface where the rays are refracted. As shown in Figure 6.1, the waves act as optical lenses, and bundles of light rays are converged to a visual focal point under wave crests and are diverged beneath wave

troughs [also see *Minnaert*, 1954; *Schenck*, 1957; *Walker*, 1994; *Zaneveld et al.*, 2001b]. This wave focusing effect is a consequence of the lensing based on the sea surface curvature, which is related to both the shape and dimension of surface waves.

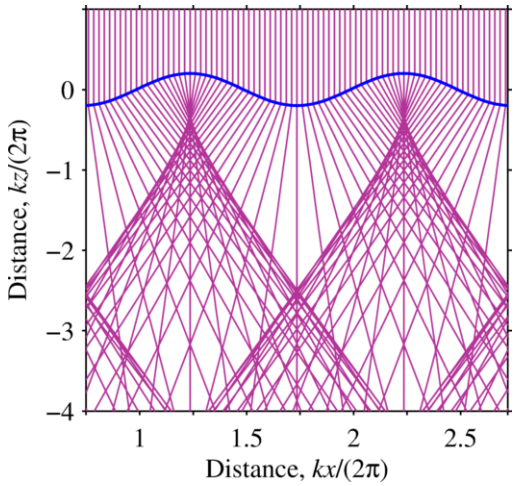

Figure 6.1 Light geometry under a sine wave. The incident is normal to the mean sea surface, represented by a sine wave, ζ=0.4×sin[kx/(2π)].

The focal depth is defined as the vertical distance from the point of principal intersection to the mean level sea surface. In Figure 6.2, the focal point O is formed by refracted rays at position A and B, onto which the direct rays are incident from a zenith angle. Assuming the sea surface takes a form of Eq. (6.2), the focal depth can be represented as

$$z_f = \Lambda\left[\frac{1}{4}\cos\theta_2 + \frac{H}{2\Lambda}\sin\theta_2\right]\cdot\frac{\sin(\alpha+\theta_3)}{\cos(\alpha+\theta_3+\theta_2)} \tag{6.4}$$

where θ_2 and θ_3 are the angles of refraction occurring at the wave crest and the inflection point; the other parameters are described as follows:

$$\alpha = \text{atan}(\frac{2}{Hk}) \tag{6.5}$$

$$\theta_2 = \text{asin}(\sin\theta_s / n_w) \tag{6.6}$$

$$\theta_3 = \text{asin}\left[\frac{\cos(\alpha+\theta_s)}{n_w}\right] \tag{6.7}$$

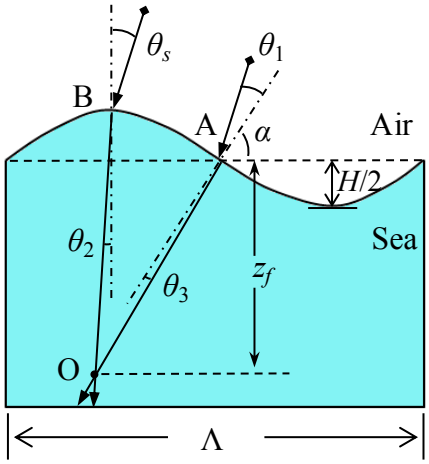

Figure 6.2 Schematic of focal point of refracted rays under wavy surface.

In Eq. (6.6) and Eq. (6.7), θ_s is the solar zenith angle (in radians) and n_w the dimensionless refractive index of sea water. The above equations are derived independently in this study; similar formulations are also given elsewhere [*McLean and Freeman*, 1996; *Nikolayev et al.*, 1972; *Zaneveld et al.*, 2001b]. In Figure 6.3a, the focal depth z_f is illustrated as a function of the solar zenith angle and the sea wave steepness, $Hk/2$. This model indicates that the focal depth monotonically decreases with increasing wave slope. In contrast, the focal depth increases until θ_s=25° when the sea slopes are large and then decreases with θ_s. Some previous work also estimated this parameter but focused on vertical incidence [e.g. *McLean and Freeman*, 1996; *Zaneveld et al.*, 2001b].

Since the oceanic wave steepness $Hk/2$ is usually less than a threshold value of 0.44-0.55 [*Toffoli et al.*, 2010], the ratio of $H/2\Lambda$ is very small (0.070~0.088) and the second term in Eq. (6.4) can be safely dropped. Then, by replacing the wavelength term in Eq. (6.4) with the dispersion relation in Eq. (6.3), the following power-law function can be obtained

$$f = F(\theta_s, H, \Lambda) \cdot z_f^{-1/2} \tag{6.8}$$

where the factor $F(\theta_s,H,\Lambda)$ (unit: $m^{1/2}\,s^{-1}$) is determined by the trigonometric functions of the solar zenith angle and the wave height and length,

$$F = \left[\frac{g \cos\theta_2 \sin(\alpha + \theta_3)}{8\pi \cos(\alpha + \theta_3 + \theta_2)} \right]^{1/2} \tag{6.9}$$

The subscript "*f*" in Eq. (6.8) will be dropped off from the depth term "*z*" in the following discussions. It is noted that this formulation actually describes the frequency signature of the irradiance fluctuations which vary inversely with the square root of the water depth, and is an extension to the previously proposed model [*Fraser et al.*, 1980]. The distribution of *F* factors is highlighted in Figure 6.3b. According to this example, *F* ranges from 0.5 to 5.3 $m^{1/2}\,s^{-1}$ with the given wave slopes and solar angles.

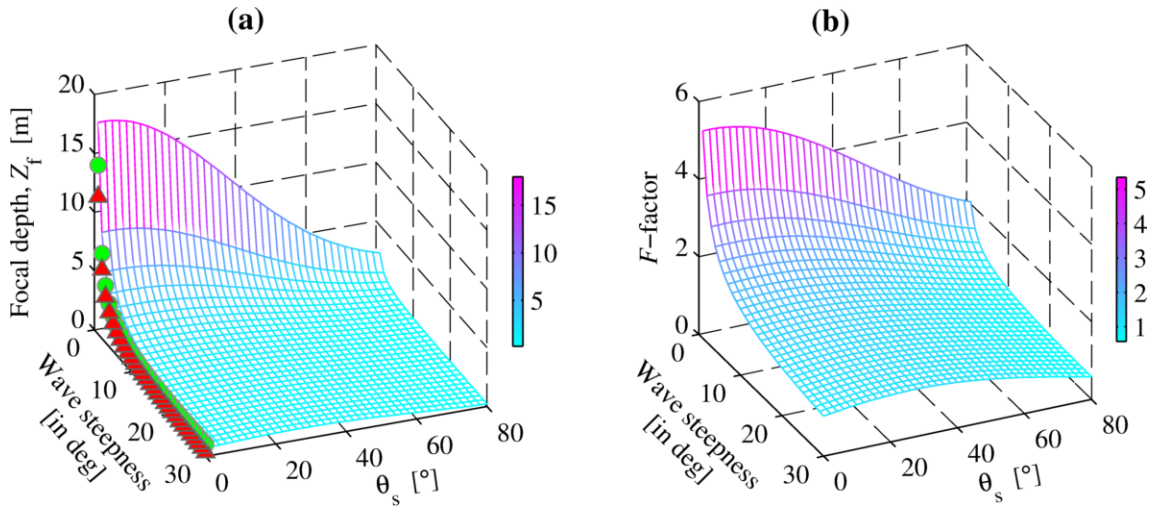

Figure 6.3 Modeling prediction of the irradiance fluctuations. (a) Focal depth of lighting geometry under a wavy sea surface. Two other predictions for vertical incidence are also overlaid according to *Zaneveld et al.* [2001b] (denoted in triangles) and *McLean and Freeman* [1996] (denoted as circles); a wavelength of 1 m is assumed. (b) The *F* factors varying with the solar zenith angle and sea wave slope.

The above derivations are based on the lighting geometry of a single wave train. The realistic sea surface is composed of a myriad of waves, of a great number of different heights, lengths, directions, and frequencies, juxtaposed as a consequence of local and far-field wind disturbances. Each wave train will produce characteristic foci dependent on the curvature: shorter waves focus the light at shallower depths, while focusing effects by longer waves are more prominent at greater depths. Eq. (6.3) is an estimate for gravity waves only. The smallest capillary waves might impact the underlying irradiance distribution as well [*Stramski and Dera*, 1988] and the measured irradiance field data

include information from both the gravity waves and the capillary waves [*Fraser et al.*, 1980; *Nikolayev et al.*, 1972; *Prokopov and Nikolayev*, 1976; *Snyder and Dera*, 1970; *Stramska and Dickey*, 1998]. In the ocean, the light also attenuates with absorption and scattering, so the irradiance measured at the primary foci is usually much higher than those at greater depth.

We do not intend to derive an analytic formulation like Eq. (6.8) for the amplitude of irradiance fluctuations in this section. In theory, the variance of the irradiance fluctuations can be very complicated [*Weber*, 2010].

6.3. Materials and Methods

6.3.1. Experimental Sites

All data used in this study were obtained during "Radiance in a Dynamic Ocean (RaDyO)" field campaigns in the Santa Barbara Channel (SBC), California in September 2008, and in the Pacific Ocean off Hawaii in August and September 2009. In the SBC, the experiment occurred approximately at the same site in the middle of the channel (34°12.3' N, 119°37.7' W), where the water depth is about 150 m. In the Pacific Ocean, the sampling sites extended westward ~200-500 km from south of the island of Hawaii.

The environmental conditions including the solar zenith angle, wind speed and sea wave height were different between the Pacific and SBC experiments (Table 6.1). The sky diffuseness is calculated as the ratio of the diffuse part of the downwelling plane irradiance above sea surface E_{diff} to the direct part of the irradiance E_{dir} using the RADTRAN model [*Gregg and Carder*, 1990]. The model parameters such as the solar zenith angle and wind speed are based on the in-situ data. Other model parameters are

input as follows: the sea-level pressure 101.1 kPa, average horizontal visibility 15 km, relative humidity 80%, precipitable water content 2.5 cm, total ozone 365 Dobson units, and airmass type 1 (marine). The large solar zenith angles observed in the SBC result in relatively high sky diffuseness, which is spectrally dependent (Figure 6.4a). More details of the wind conditions and wave measurements are reported by *Zappa et al*. [2012].

The two seas are representative of optically contrasting waters: the Pacific Ocean water off Hawaii can be treated as Case 1 water, for which the optical properties are dominated by the phytoplankton and related organic dissolved and particulate materials [*Morel and Prieur*, 1977]; the Santa Barbara Channel water generally belongs to Case 2 water whose optical properties are significantly influenced by other decoupled constituents such as inorganic particles and organic materials. Their in-situ optical properties are summarized in Figure 6.4b, Figure 6.4c and Figure 6.4d. In the coastal water of the Santa Barbara Channel the light attenuation in the blue band is very strong due to the absorption of high levels of dissolved organic matter (or colored dissolved organic material, a.k.a. CDOM) and organic detritus and phytoplankton. In contrast, irradiance in the Pacific diminishes slowly in the blue and drops much faster for longer wavelengths. With no exception, the scattering coefficient decreases for longer wavelengths.

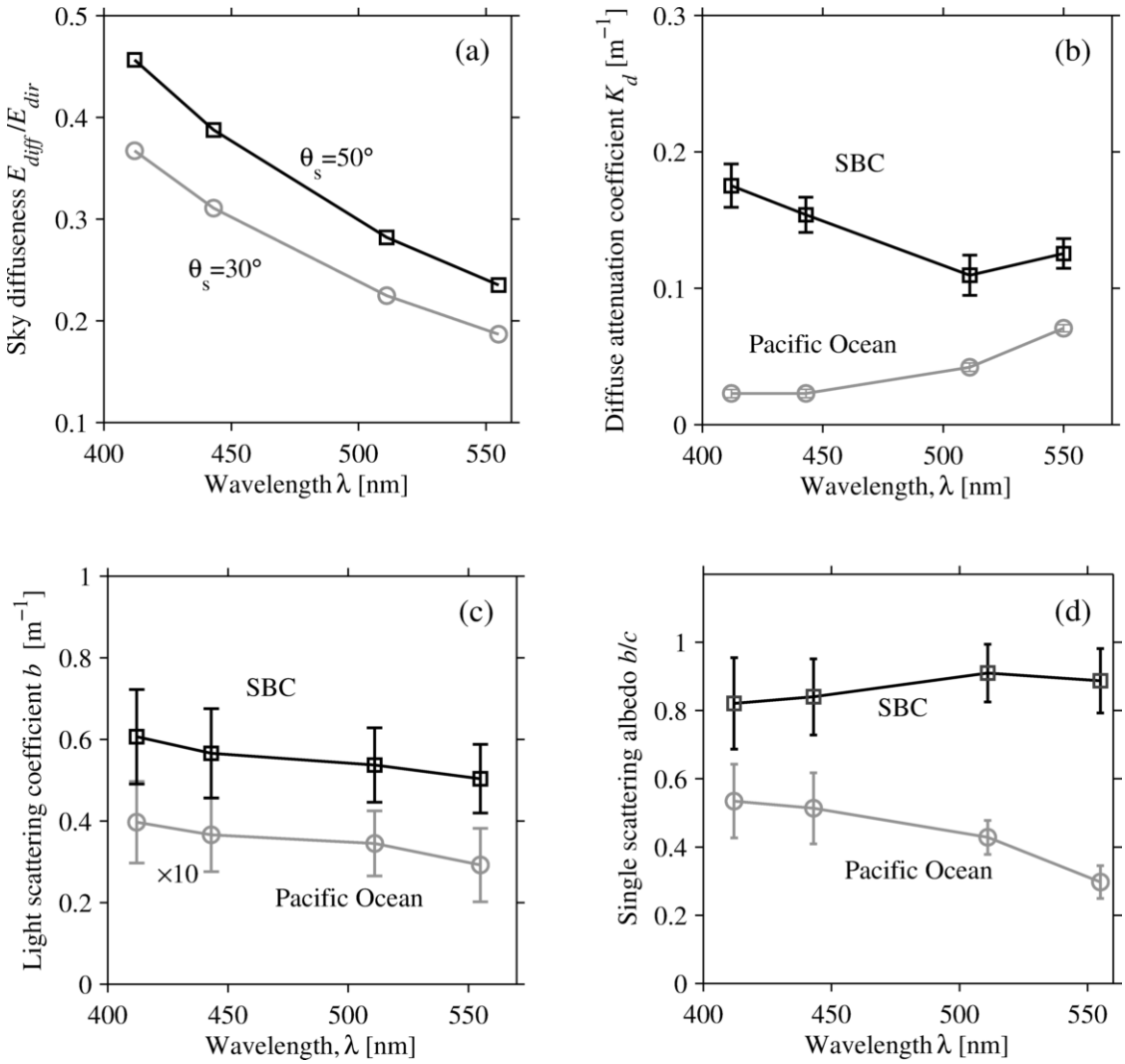

Figure 6.4 Summary of optical properties. (a) Sky diffuseness. (b) Diffuse attenuation coefficient for downwelling irradiance. (c) Light scattering coefficient. (d) Single scattering albedo.

Table 6.1 A summary over the irradiance measurements used for the present study.

Property	Santa Barbara Channel	Pacific Ocean
Observation date (UTC)	Sept. 9-Sept. 20, 2008	Aug. 27-Sept. 14, 2009
Observation time (UTC)	~18:00, & 22:00-23:00	20:00-21:00, & ~1:00
Observation time (Local Time)	~11:00, & 15:00-16:00	10:00-11:00, &~15:00
Sites of profile observations	9	11
Sites of time series observations	5	7
Profile-time series matchups	6	7
Instrument fall velocity, ω_s [m s^{-1}]	0.23±0.08	0.31±0.04
Data acquisition rate [Hz]	7	7
K_d(555nm) [m^{-1}]	0.13±0.01	0.07±0.00
Wind speed, U_{10} [m s^{-1}]	6.8±1.7	8.6±1.4
Solar zenith, θ_s [deg]	48.2±4.8	32.9±5.4
Significant wave height, H_s [m]	0.75-1.7	1.85-2.35
Dominant wave frequency, f_p [Hz]	0.08-0.3	0.07-0.14
Wave age, C_p/U_{10} (C_p is the phase speed)	0.68-5.36	1.25-2.54

6.3.2. Instrument and Deployments

A commercial system was used in our study to measure the irradiance depth profiles, which consisted of a coupled irradiance/radiance radiometer (OCR-504I/R, Satlantic LP, Halifax, Canada) installed on the wing of the free-fall profiling RadCam package. The downwelling irradiance sensor OCR-504I and the downwelling radiance camera are on the upper end of a cylindrical housing. A CTD sensor to measure the water conductivity, temperature and depth, and a tilt/compass sensor to measure the instrument's roll, pitch and heading are integrated with this instrument package. All the principal and ancillary sensors are synchronized and are linked to a control computer via a fiber optic cable.

The OCR-504I is a four-channel radiometer recording the downwelling plane irradiance at discrete wavelengths of 412, 443, 511 and 555 nm (FWHM 10 nm). Calibration of the irradiance sensor was carried out according to the ocean color calibration protocols [*Mueller et al.*, 2003]. This irradiance collector has surface area of 86 mm^2 and follows a cosine response within its 180° field of view. It samples instantaneously at a fixed frequency at 7 Hz. The measured irradiance data can be referenced to the instantaneous measurement of inclinations (tilt, pitch and yaw). The sky illumination condition was monitored with an all-sky radiance camera (at 555 nm) and a sky reference radiometer (at the same four wavelengths), which are also synchronized with the control computer.

Continuous irradiance depth profiles were obtained by releasing the instrument package in a free-fall mode [*Lewis et al.*, 1986; *Waters et al.*, 1990] at a speed of w_s = 0.2-0.3 m s^{-1} in the water column, from the deck of the R/V *Kilo Moana*. It usually took less than 3 minutes to profile the water column from the surface to 40 m depth. The instrument's inclinations were small, with tilts less than 5° for both roll and pitch 90% of the time. At some sites, replicate casts were obtained for irradiance depth profiles, which were generally offset in time by about 3 minutes.

The diffuse attenuation coefficients for the depth profiles, K_d, were determined using the irradiance integration method [*Zaneveld et al.*, 2001b]. The solar zenith angle, θ_s, was computed from the geographic coordinates and the time of observation [*Reda and Andreas*, 2004].

Irradiance fluctuations were also measured in the more traditional fashion by hanging the instrument package from a small float (25 cm in diameter), which followed the sea

surface displacements and henceforth was not present at a constant depth relative to the mean sea surface level. To reduce the shadowing effect by the small float, we constrained the measurement positions to the first 40 meters in the Pacific Ocean and the first 10 meters in the Santa Barbara Channel. With this arrangement, the float is often observed in vicinity of the Snell's boundary. These time series will be referred to as "fixed-position" or "fixed-depth" observations. These measurements took place within15-30 minutes after the irradiance profiling deployments. Changes of solar positions within this short time period were small (no larger than 5°, Table 1).

The upper water column was also profiled with a WET Labs AC-9 meter measuring the absorption coefficient a and the attenuation coefficient c at nine wavelengths including 412, 443 511, and 555 nm. The scattering coefficient is then given as the difference between the attenuation coefficient and absorption coefficient, $b = c - a$. Deployment and data processing of AC-9 are described in *Twardowski et al.* [2012]. In our experiments, the AC-9 meter was usually deployed 30 minutes to one hour before the OCR-504I radiometer. We determined the mean scattering coefficients by averaging the measurements over 0-40 m in Hawaiian experiment and 0-10 m in SBC (see Figure 6.4c and Figure 6.4d).

6.3.3. Irradiance Data Screening

The raw OCR-504I radiometer measurements of irradiance are calibrated to physical units, after applying the immersion coefficients. Both the irradiance depth profiles and fixed-depth irradiance time series undergo the following subsequent data quality checks.

The first check is to verify that the sky radiation is relatively stable during the instrument deployment. The downwelling irradiance above the sea surface, E_s, is derived from the sky reference camera and the OCR-504I surface radiometer recordings. The coefficient of variation (CV), or the ratio of the standard deviation of irradiance to the mean value of irradiance, is then estimated for the sky radiation. Those data sequences having CVs over 5% are eliminated from the following analysis. The second criterion is to ensure that the sky is clear by comparing the ratio of in-situ downwelling irradiance above the sea surface with theoretical values at 555 nm. The theoretical irradiance is calculated with the Hydrolight 5.0 software, which derives the E_s through the RADTRAN sky radiation model [*Gregg and Carder*, 1990]. The sky is regarded as "clear" only if the ratio is higher than 85%.

There are a total of 20 profiles and 12 fixed-position time series found after the above threshold checks.

6.3.4. Irradiance Data Decomposition

The irradiance depth profile data recorded from the OCR-504I radiometer are used as the principal data set in this study.

As a mathematical convenience, the irradiance values were first transformed into natural logarithmic scales. The transformed irradiance profiles were further normalized according to the following relation

$$I_n(z) = \frac{\ln E_d(z) - < \ln E_d(z) >}{< \ln E_d(z) >} \tag{6.10}$$

where $<\ln E_d(z)>$ is the smoothed irradiance computed as the linear fit to the log-transformed irradiance values, where the diffuse attenuation coefficient K_d in Eq. (6.1) is

treated as a constant for the range of water column of interest, and $I_n(z)$ is called the normalized irradiance residuals hereafter. For the wavelet transform, the irradiance profiles are treated as equivalent to a (non-stationary) time series, i.e., irradiance sequences with respect to observation time, denoted as $I_n(t)$. The data transformation applied by Eq. (6.10) is necessary to ensure that the wavelet transform produces reliable results [*Grinsted et al.*, 2004].

To identify the dominant modes of fluctuations in the irradiance depth profiles, the technique of wavelet transformation (WT) was used. The wavelet transform is advantageous over Fourier transform (FT) in that it is able to decompose the nonstationary irradiance profile data sequences into the time-period space and the depth-wavelength space, or the depth-period space assuming that the instrument dropping speed is nearly constant. Another advantage of using the wavelet transform is that it is scale independent and there is no need for a predetermined scale that could limit the frequency range. As such, wavelet analysis can likely reveal the evolution of dominant modes of irradiance fluctuations with depth and/or time. A summary of wavelet analysis in geophysics and the wavelet software were provided by *Torrence and Compo* [1998] and are available at http://atoc.colorado.edu/research/wavelets/. The continuous wavelet transform with uniform time steps Δt is defined as the convolution of I_n (t) with the wavelet function $\psi(t)$,

$$W_n(S) = \sum_{n'=0}^{N-1} I_n \psi^* \left[\frac{(n'-n)\Delta t}{S} \right] \tag{6.11}$$

where n is the localized time index, N is the number of points in the time series and the asterisk indicates the complex conjugate. Eq. (6.11) gives a complex continuous wavelet

transform (CWT). The squared modulus of the CWT, $|W_n(S)|^2$, is used in this context for convenience.

The choice of wavelet function in this study was the Morlet wavelet, a complex nonorthogonal wavelet consisting of a sinusoid modulated by a Gaussian envelope

$$\psi(t) = \pi^{-1/4} \exp\left[i\omega_0 \left(\frac{t}{S}\right) \right] \exp\left[-\frac{t^2}{2S^2} \right] \tag{6.12}$$

where t is the time (unit: s), S is the wavelet scale (unit: s) and ω_0 is the nondimensional frequency. In our analysis, the nondimensional parameter $\omega_0 = 6$ was used, such that there are three oscillations within the Gaussian envelope and the wavelet scale S is almost equal to the Fourier period, i.e. $T = 1.03 \times S$. We use the term "period" hereafter to describe the wavelet transform. The reciprocal of the period is the frequency, f, with the unit of Hertz.

To determine the significance of the wavelet spectra, a background red noise process was constructed and modeled as a first order univariate autoregressive (AR1, or Markov) process

$$x_n = \alpha x_{n-1} + \varepsilon_n \tag{6.13}$$

where α is the lag-1 autocorrelation, $x_0 = 0$, and ε_n is taken from Gaussian white noise. The normalized power spectrum of this AR1 process is defined as

$$P_k = \frac{1-\alpha^2}{1+\alpha^2 - 2\alpha\cos(2\pi k / N)} \tag{6.14}$$

where $k = 0 \ldots N/2$ is the Fourier frequency index, and α is the lag-1 autocorrelation estimated from the normalized irradiance residuals. The statistical significance of the wavelet power was then assessed relative to the null hypothesis that the signals (normalized irradiance residuals $I_n(t)$) have a mean power spectrum as P_k; if a peak in the

wavelet power spectrum is significantly above the background spectrum, it can be assumed to be a true feature. To determine the 95% confidence level (significant at 5%), the background spectrum of Eq. (6.14) was multiplied by the 95th percentile value for χ_2^2, which implies chi-square distribution with two degrees of freedom.

Based on the computed wavelet spectrum, we derived the dominant frequency by locating the frequency with a local maximum variance value. The identified frequencies are only accepted if the estimated confidence level is above 95%. A special relationship is determined between the variance of irradiance residuals, Var[$I_n(\lambda,z)$], and the coefficient of variation. The derivation starts with Eq. (6.10). We first take the variance for both sides of this equation, which is described as

$$Var\left[I_n(\lambda,z)\right] = \frac{Var\left[\ln E_d(\lambda,z)\right]}{<\ln E_d(\lambda,z)>^2} \tag{6.15}$$

The denominator is already known in our analyses. The numerator can be further transformed into the following relation by considering the second order Taylor expansion,

$$Var\left[I_n\right] = \frac{Var\left[E_d\right]}{(\mathrm{E}\left[E_d\right])^2} \cdot \frac{1}{<\ln E_d>^2} \tag{6.16}$$

In the above equation, E[E_d] denotes an expectation of the downwelling plane irradiance, and the dependence on depth and wavelength has been omitted for simplicity. Note that the first part on the right hand side of Eq. (6.16) actually gives the square of the CV at depth z. We derived the continuous CV profiles based on this scheme for each irradiance depth profile.

For the fixed-position irradiance time series data, we used spectral analysis to derive the power spectral density. The Parzen's windowing technique was adopted. The

dominant frequency f_p was determined as the one which gives the maximum variance. The coefficient of variation was also computed.

The parameters (CV and dominant frequency f_p) have been so computed from both the irradiance profiles and the fixed-position irradiance time series. To estimate the errors of each parameter derived from the irradiance profiles, the relative Root Mean Square Error (RMSE) for each parameter was computed according to

$$RMSE = \left[\frac{1}{n} \sum_{i=1}^{n} (P_i / Q_i - 1)^2 \right]^{1/2} \times 100\% \tag{6.17}$$

where P_i is the quantity (CV or f_p) derived from measured profiles and Q_i refers to the quantity from the fixed-position time series.

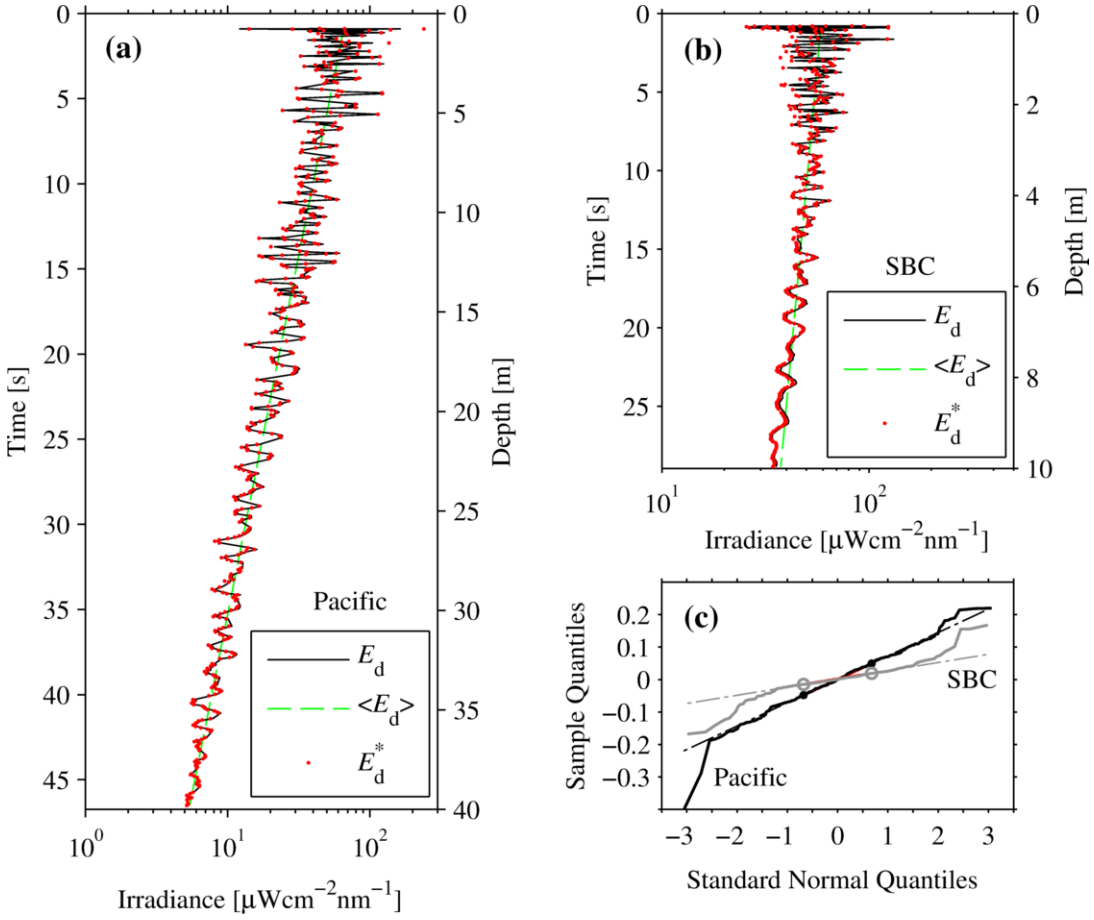

Figure 6.5 Example data of measured irradiance profiles. (a) Irradiance depth profiles (λ=555 nm) in the Pacific Ocean under clear sky. The irradiance profiles (including the tilt-uncorrected irradiance E_d, smoothed irradiance <E_d> and tilt-corrected irradiance E_d^*) were derived from the radiance distribution measured on September 5, 2009, 00:30 UTC; the camera package descends at a speed of 0.45 m s^{-1} in water; data acquisition frequency 4 Hz; clear sky; wind speed 10 m s^{-1}; sea surface is dominated by 1.5-2 m waves. (b) Irradiance depth profiles (555 nm) in the Santa Barbara Channel under clear sky. This profile was collected on September 15, 2008, 17:40 UTC; instrument dropping speed 0.2 m s^{-1}; significant surface wave height 1 m. (c) Quantiles-quantiles plot for the

irradiance residuals $I_n(z)$. In panel (3), the black thick line (corresponding to the Pacific Ocean data in panel (a)) and the gray thick line (corresponding to the SBC data in panel (b)) represent the irradiance residuals $I_n(z)$; the corresponding linear fits are denoted in dash-dot lines; and the 1st and 3rd quantiles are shown as black dots and open circles respectively.

6.4. Results

6.4.1. Example Data of Irradiance Depth Profiles

Irradiance depth profiles are presented in Figure 6.5a and Figure 6.5b for the clear oceanic waters (with moderate sea state) and the coastal waters (with relatively calm sea state) respectively. The smoothed irradiance, $<E_d>$, is described by an exponential fit to the original irradiance data (E_d) as indicated in Eq. (6.1) but with a constant K_d. As illustrated in the plots, the irradiance sequences are functions of water depth as well as the observation time.

The data sequences of irradiance depth profiles describe a unique yet nonstationary process, in which both the irradiance mean and variance vary with depth and time. The instantaneous irradiance oscillates about the mean and is slightly positively skewed. The deviations of the instantaneous irradiance about the mean irradiance profile are generally attenuated with water depth [also see *Siegel and Dickey*, 1988; *Zaneveld et al.*, 2001b]. The deviations of irradiance measurements from the mean irradiance $<E_d>$ are referred to as "the irradiance fluctuations" in depth profiles hereafter. The plots in Figure 6.5a and b also indicates that the distance (Δz, in terms of water depth) between two neighboring local maxima or minima in the irradiance profiles actually increases with water depth. In

Figure 6.5a, for example, Δz is about 0.5 m at depth of 5 m, but changes to a larger value of Δz = 1.5 m, at a position of 22 m, corresponding to the time difference, ΔT, increasing from 1.1 s to 3.3 s at the given drop velocity. The irradiance residuals approximately follow a normal distribution (Figure 6.5c).

6.4.2. Example Wavelet Spectra of Irradiance Profile

The wavelet spectra of the detrended and normalized irradiance sequence $I_n(t, z, 555\text{nm})$ in the time-period domain are illustrated in Figure 6.6, in which the absolute value squared of the transform is normalized by the total variance. The data were taken from the Hawaii experiment. The spectra corresponds to the irradiance depth profile demonstrated in Figure 6.5a. The x-axis gives the Fourier period, while the y-axis describes the evolution of observation time. The observation time scales to the water depth through the drop velocity (not shown in figure). The artifacts with the spectra are that the wavelet is not completely localized in time, and may be subjected to the edge effects. We have used the cone of influence (COI) to define such areas in Figure 6.6, where the black contour encloses regions of greater than 95% confidence for a red-noise process. The spectra show a characteristic distribution of periods. Wavelet transform in the time-period domain allows for identification of the local dominant periods of irradiance fluctuations, at which the power in the spectra reaches the maximum and is above the 95% confidence level. The dominant periods increase from 0.25 s near the surface to about 4 s at depth of 40 m. The inverse of the period gives the dominant temporal frequency f_p, which decreases with water depth.

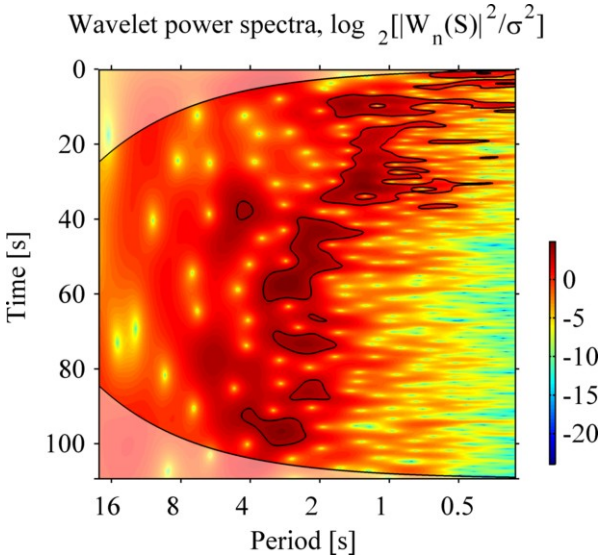

Figure 6.6 Normalized continuous wavelet power spectra, $\log_2[|W_n(S)|^2/\sigma^2]$, for the irradiance residuals I_n at λ = 555 nm. The normalization by σ^2 gives a measure of the power relative to white noise; the thick black contour represents the 95% confidence interval; the cone of influence (COI) is depicted by a transparent patch. The irradiance profile, E_d, was collected in clear Pacific Ocean off Hawaii, on September 5, 2009, 00:30 UTC; clear sky; solar zenith angle 32°; wind speed 9.2 m s^{-1};

6.4.3. Depth Distribution of Dominant Frequency

The relationship between the dominant frequency of irradiance fluctuations and water depth is described in this section. Data points are resampled at every half meter in the wavelet evolutionary spectra, and those with confidence levels lower than 95% are discarded. Figure 6.7a shows an example of the frequency distribution of irradiance fluctuations at 555 nm from the Pacific Ocean, representing the sea state under high winds of ~ 9 m s^{-1} and significant sea wave heights of 2.1 m. The model of Eq. (6.8), f_p =

$F \times z^{-0.5}$, where $z > 0$, is satisfactorily fitted to the resampled frequency data, with the F factor equal to 1.614 $m^{1/2} s^{-1}$ and the coefficient of multiple determination $R^2 = 0.574$.

In Figure 6.7b, the ensemble of such fitted f_p profiles from the Pacific Ocean is displayed in log space. These profiles represent the irradiance observations taken under similar environmental conditions, that is, high winds (U_{10} = 5-10 m s^{-1}) and medium solar zenith angles (θ_s = 27-35°). The fitted F factors have a mean value of 2.06 with a standard deviation of 0.41, i.e., $F = 2.06 \pm 0.41$ $m^{1/2} s^{-1}$.

Figure 6.7c presents an example for the f_p profile data measured in the Santa Barbara Channel, and Figure 6.7d illustrates the ensemble of fitted f_p profiles in the Santa Barbara Channel. The F factors are found to be generally lower than those observed in the Pacific, with a mean value of 1.31 and with the standard deviation of 0.20, i.e., $F = 1.31 \pm 0.20$ $m^{1/2} s^{-1}$.

Historical data [*Gernez and Antoine*, 2009; *Prokopov et al.*, 1975; *Snyder and Dera*, 1970; *Stramska and Dickey*, 1998] are also overlaid in Figure 6.7b and Figure 6.7d, which are slightly higher than our deviations in the Santa Barbara Channel but very close to our observations in the Pacific Ocean. This difference is likely contributed by the different solar zenith angles and wave conditions met in the field experiments (recalling Figure 6.3).

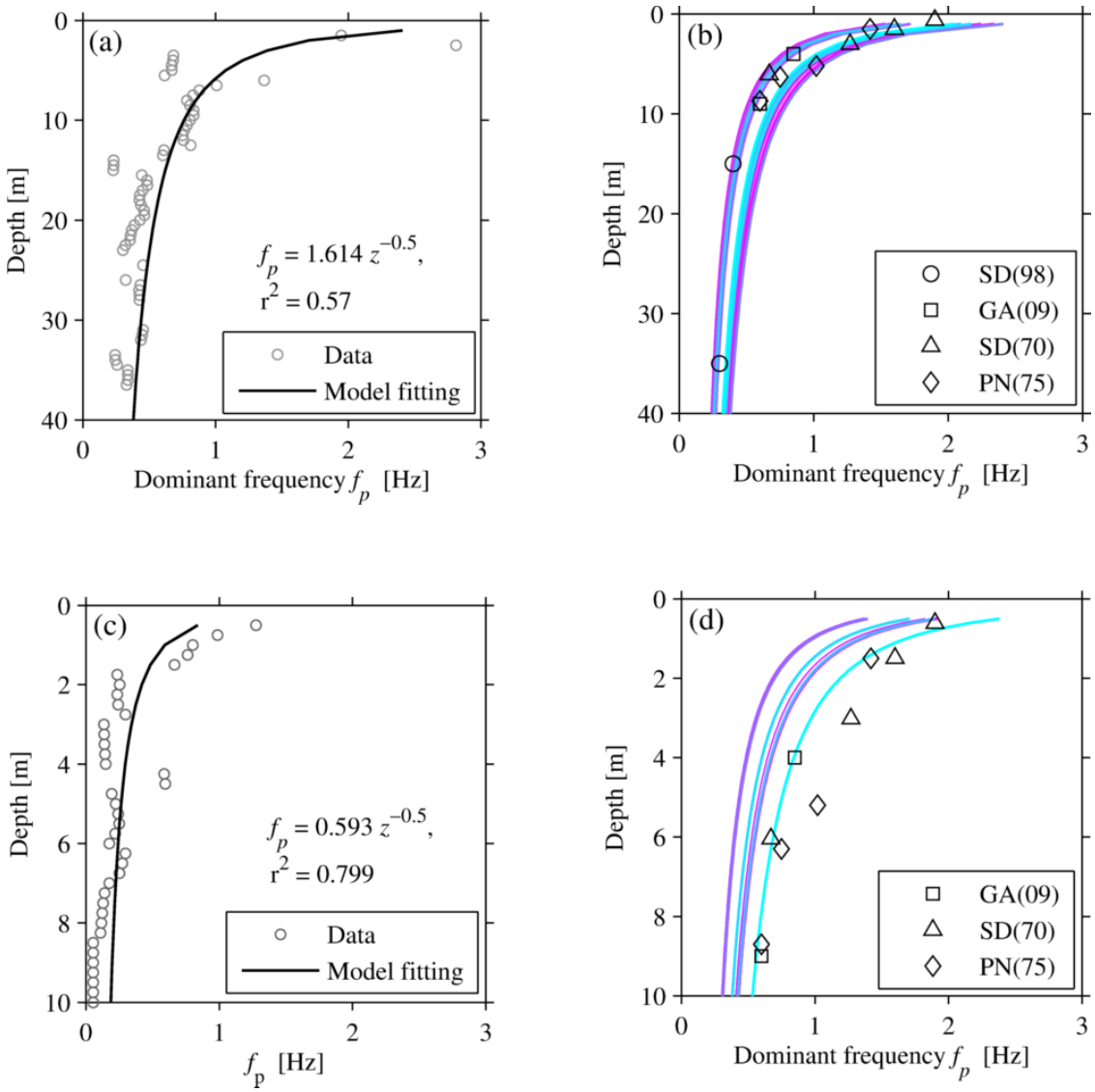

Figure 6.7 Depth evolution of the dominant frequency of the irradiance fluctuations derived from irradiance profiles (555 nm) measured under clear skies. (a) Example of model fitting for the Pacific Ocean data, which were retrieved on September 5, 2009, with wind speed 9.2 m s^{-1} and solar zenith angle 32°; the significant height of sea waves was 2.1 m. (b) The fitted f_p distributions in the Pacific Ocean; a total of 12 measured irradiance depth profiles are processed for the model fitting and represented by lines in different colors. (c) Example model fitting of the Santa Barbara Channel data, which were recorded

on September 14, 2008, with wind speed 7.7 m s^{-1} and solar zenith angle 54°; the significant height of sea waves was 0.85 m. (d) A family of the f_p profiles in the Santa Barbara Channel; a total of 9 irradiance depth profiles are used for the model fitting and represented by lines in different colors. The historical f_p data are overlaid for comparison. SD(98): λ = 555 nm, θ_s = 30°, by *Stramska and Dickey* [1998]; GA(09): λ = 510 nm, θ_s = 20-85°, by *Gernez and Antoine* [2009]; SD(70): λ=525 nm, θ_s = 35-44°, by *Snyder and Dera* [1970]; PN(75): λ = 525 nm, θ_s = 36-57°, by *Prokopov et al.* [1975].

6.4.4. Depth Distribution of Coefficient of Variation

The variance Var(I_n) is required for the derivation of the coefficient of variation (Eq. (6.16)). In our analysis, the variance is determined as the average over bands of 0.25 to 4 seconds for each depth based on an objective examination of the wavelet spectra of the irradiance depth profiles; 4 Hz (0.25 s in period) roughly corresponds to the Nyquist frequency of our data, and 0.25 Hz (4 s in period) is the dominant frequency over 5% significance found at depths of 40 m in the Pacific Ocean (see Figure 6.7). We also note that only the variance beyond the COI (that is free from edge effect) and above 5% significance level in the wavelet spectra is considered in the variance integration. Before the procedure was started to compute the coefficient of variation, the sufficiency of the chosen frequency band was first evaluated. It is found that more than 98% of the variance in the original series can be accounted for over the frequency band 0.25 Hz to 4 Hz.

The evolution of the coefficient of variation of the irradiance fluctuations with water depth is illustrated in Figure 6.8a and Figure 6.8c. Our analysis shows that the

coefficients of variation generally decrease with water depth; this finding agrees with previous reports from fixed-depth irradiance time series data [e.g. *Darecki et al.*, 2011; *Fraser et al.*, 1980; *Gernez and Antoine*, 2009; *Prokopov et al.*, 1975].

Several simple models are tested for description of the depth evolution of the coefficient of variation, including the exponential function and polynomial functions and a similar formulation with Eq. (6.8),

$$CV = \left(K_{CV} z\right)^{-1/2} \qquad (z > 0) \tag{6.18}$$

where K_{CV} (unit: m^{-1}) is the only parameter determining the coefficient of variation besides the water depth z. It is found that the model of Eq. (6.18) can satisfactorily fit most of the profiles in the two sea surface waters with the coefficient of determination often greater than 0.4. Hereafter, K_{CV} is called the attenuation coefficient for CV.

Families of fitted curves of the coefficients of variation as a function of water depth are displayed in Figure 6.8b and Figure 6.8d, representing the data from the Pacific and the Santa Barbara Channel, respectively. On average, the attenuation coefficients for CVs in SBC are greater than those in the Pacific Ocean. Some published data are also superimposed on these two plots for a qualitative comparison.

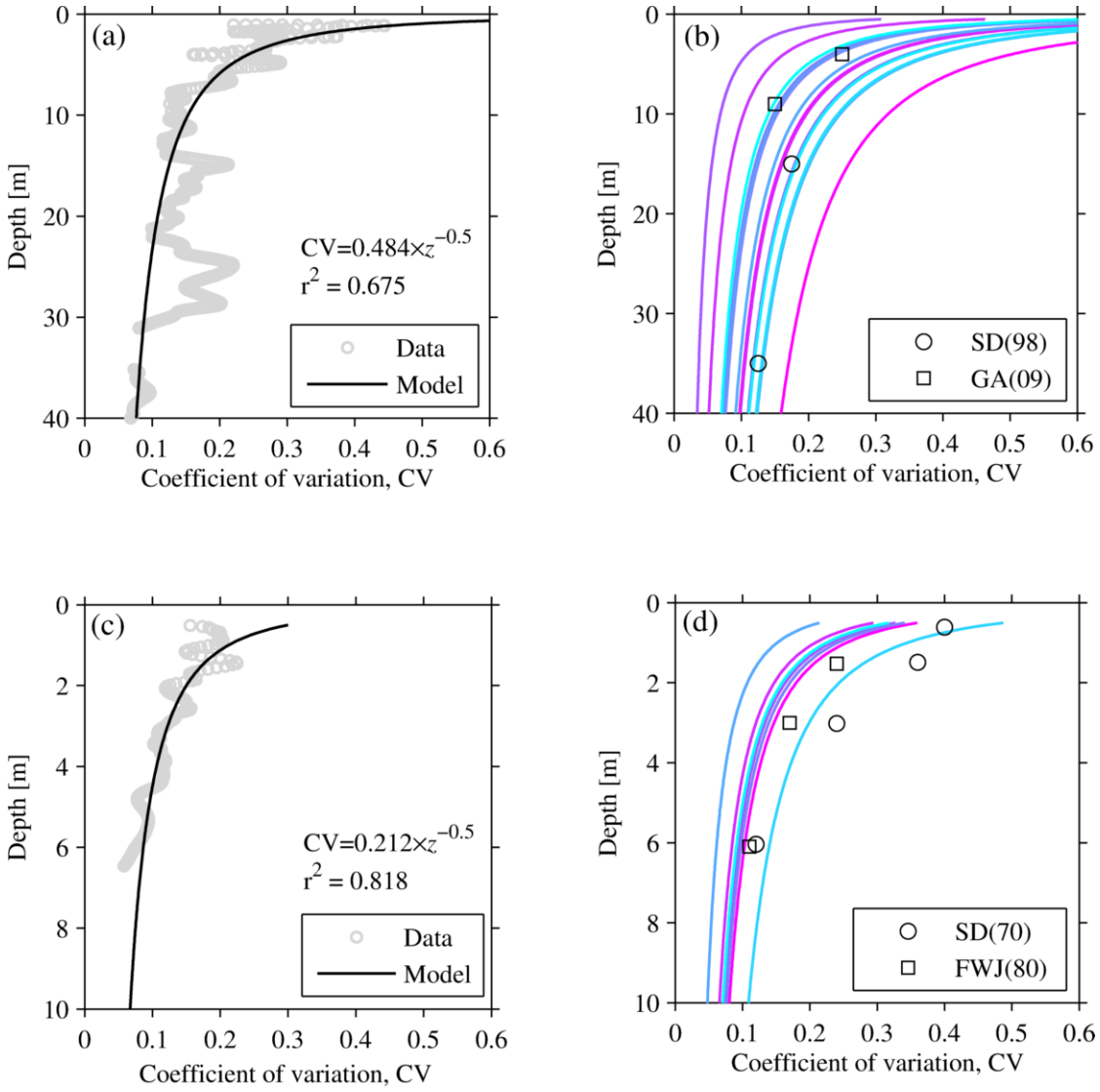

Figure 6.8 Depth evolution of the coefficient of variation of the irradiance fluctuations derived from irradiance profiles (555 nm) measured under clear skies. (a) Example of model fitting of the CV distribution in the Pacific Ocean; same profile was used as Figure 6.7a. (b) Ensemble of fitted CV profiles in Pacific Ocean represented by lines in different colors. (c) Example of model fitting of the CV distribution in the Santa Barbara Channel; same irradiance profile was used as Figure 6.7c. (d) A family of the CV profiles in the Santa

Barbara Channel represented by lines in different colors. Historical CV data are also shown for comparison. SD(98): λ = 555 nm, θ_s = 30°, by Stramska and Dickey [1998]; GA(09): λ = 510 nm, θ_s = 20-85°, by Gernez and Antoine [2009]; SD(70): λ = 525 nm, θ_s = 35-44°, by Snyder and Dera [1970]; FWJ(80): λ = 525 nm, θ_s = 42°, by Fraser et al. [1980].

6.4.5. Spectral Dependence of Irradiance Fluctuations

The depth distributions of the dominant frequency and the coefficient of variation have been presented so far for one wavelength at λ = 555 nm, and their spectral dependence is now examined for all four wavelengths including 412, 443, 511 and 555 nm. These spectral irradiance data were measured simultaneously by the OCR-504I radiometer.

We have not observed apparent and consistent trends in the spectral F factor based on individual irradiance profiling deployment (data not shown). The F factors derived from the Pacific Ocean and the Santa Barbara Channel are pooled in Figure 6.9a. The SBC data give a rather flat distribution of F factors over these spectral bands (ANOVA, F-ratio = 0.06, p = 0.982). Although the mean F factor reaches a low value at 443 nm and then increases a bit, the spectral dependence is not significant either for the Pacific Ocean data (ANOVA, F-ratio = 1.03, p = 0.394).

Unlike the frequency content, the amplitudes of the irradiance fluctuations show a systematic variation with the wavelength according to individual irradiance profiling deployments (data not shown). All the derived K_{CV} factors are summarized in Figure 6.9b, which shows a monotonic decrease of the mean K_{CV} factors with the light wavelength.

This variability is significant for both the Pacific data (ANOVA, F-ratio = 3.78, $p = 0.021$) and the SBC data (ANOVA, F-ratio = 8.75, $p < 0.001$). According to Eq. (6.18), the spectral variability of K_{CV} means the coefficient of variation is actually increasing with the optical wavelength.

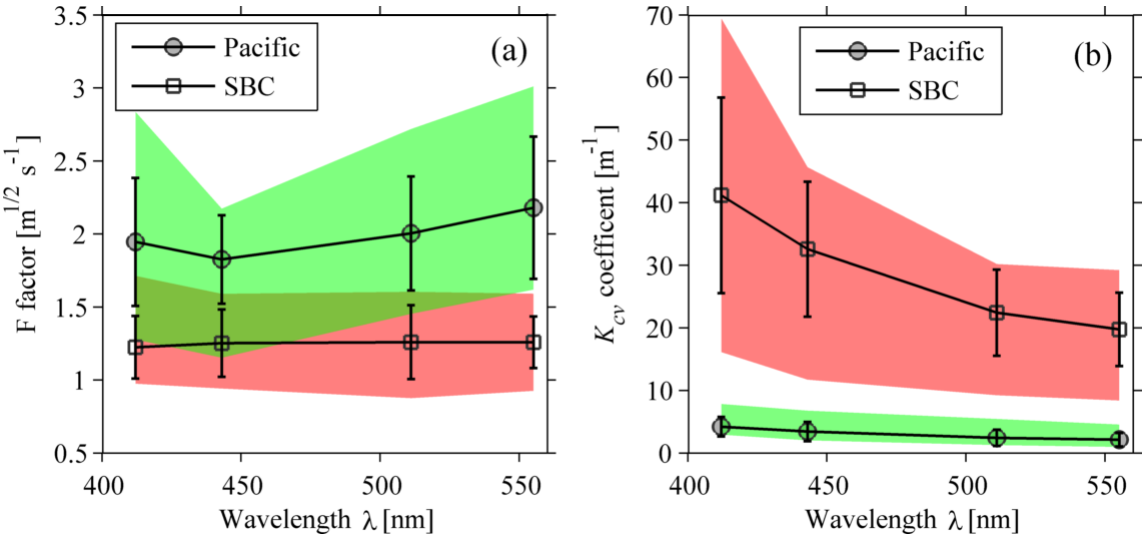

Figure 6.9 Spectral dependence of irradiance fluctuations in the measured irradiance depth profiles under clear skies. The mean values are denoted as circles (for Pacific Ocean data) and squares (for SBC data); the error bars represent the standard deviations of the data. The shaded areas (green for Pacific data, and red for SBC data) describe the upper and lower limits of the observed parameters.

6.4.6. Data Validation and Repeatability

In previous sections we have been focusing on the signatures of light field fluctuations in the continuous irradiance profiles. We now present the validation of the irradiance depth profile derivations against the independent measurements of irradiance variability at fixed depths and second by examination of replicate profiles.

For the first comparison, statistics derived from fixed depth deployments were compared with those derived from a profile collected within 15-30 minutes and under clear skies. The OCR-504 radiometer suspended at fixed depths often underwent a little larger tilt (but usually less than 10°) than those of depth profiling data. We first checked for the potential impact of the sensor's tilt on the irradiance measurements and according to our observation, the absolute difference induced by the instrument's tilt is less than 5% with regard to the mean, standard deviation and CV of the irradiance time series; this is consistent with theoretical predictions [*Gege and Pinnel*, 2011].

We compared parameters derived from the irradiance depth profiles with those measured by suspending the instrument at fixed depths below the sea-surface in Figure 6.10. The dominant frequencies determined from the two data sets agree with each other (Figure 6.10a) with no significant difference according to a paired *t*-test (t = -0.704, df = 35, and p = 0.486, at α = 5% significance level). For the coefficient of variation (Figure 6.10b), the two methods have also generated consistent results (t = -0.191, df = 31, and p = 0.85, at α = 5% significance level). As an additional result, we derived the mean irradiance $\overline{E}_d$ from the fixed-depth irradiance time series by taking the exponential of the mean of the log-transformed irradiance. In Figure 6.10c, the profiles generate an average irradiance at depth that is not significantly different from that derived from the fixed-

position time series; the paired t test is insignificant (t = 0.683, df = 23, and p = 0.501, at α = 5% significance level). For the mean irradiance, we have corrected for the variation of above-surface irradiance E_s even though it is small.

We also examined replicate irradiance profiles taken by the free-fall OCR-504I unit. Each pair represents repeated profiles with the same environmental conditions including the wind speed and solar zenith angle and within 15-30 minutes of each other. With regard to the dominant frequency, the pairs of derived F factors show no significant difference with each other after the paired t test (p =0.0.117, t = 1.609, df = 35, α = 0.05). Since the coefficient of variation is dependent on wavelength (refer to previous figures), we test the repeatability of the paired K_{CV} coefficients with respect to each wavelength and find that p-values are all greater than 0.325 and insignificant at significance level α = 0.05. The K_{CV} parameters are also pooled together for the paired t test, which shows the paired data again are not significantly different. The paired t-test results for the comparison are summarized in Table 6.2.

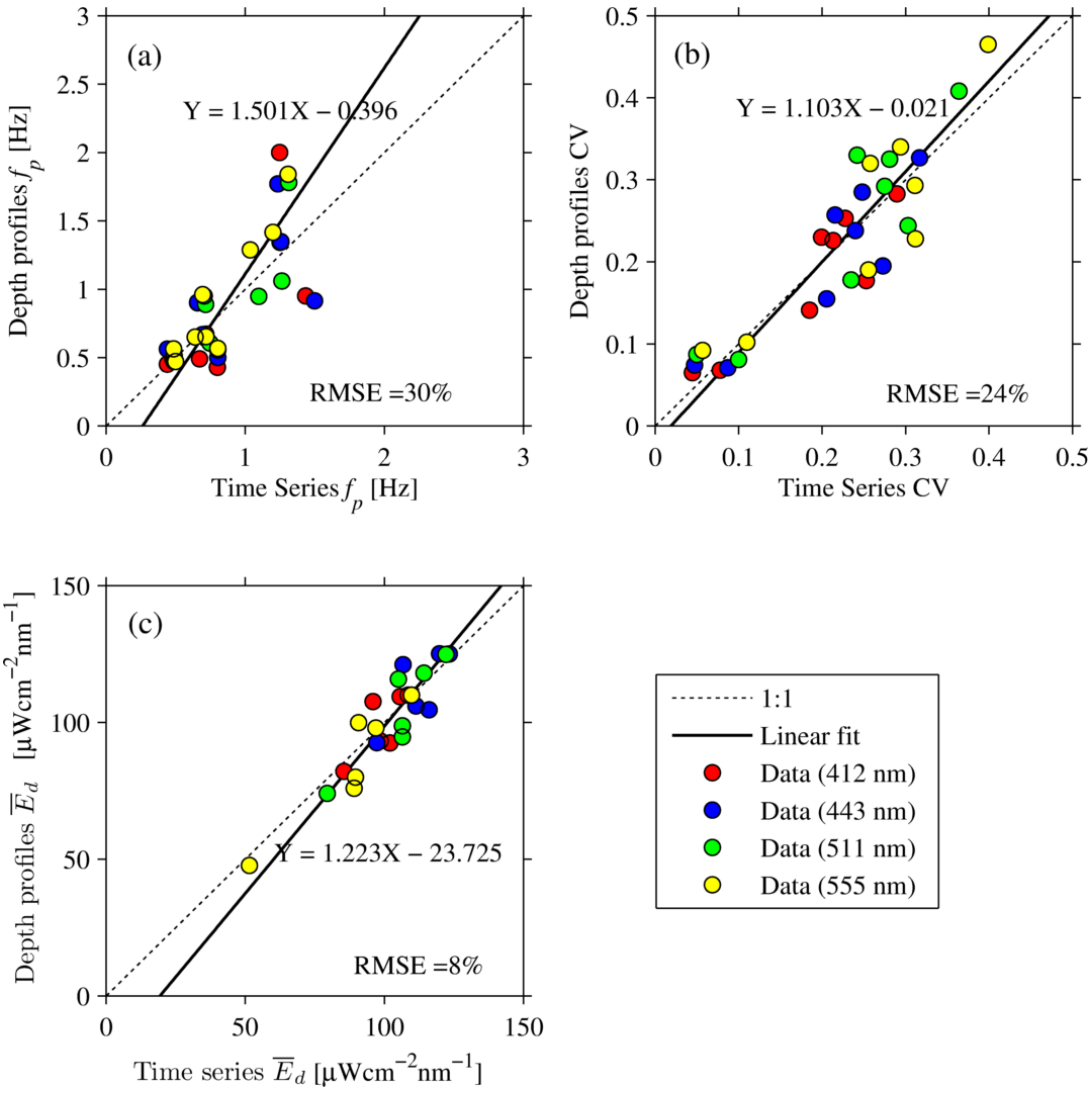

Figure 6.10 Scatter plots of signatures derived from irradiance depth profiles and fixed position time series under clear skies. (a) Dominant frequency f_p derived within water depths of 0.6-13.5 m. (b) Coefficient of variation derived within water depths of 2.3-13.5 m. (c) Mean irradiance derived within water depths of 0.6-13.5 m. The RMSE is also indicated for the depth profiles' deviations and time series derivations.

Table 6.2 Summary of paired *t*-test for the comparison of the two matched *F* factors and K_{CV} factors derived from the two irradiance depth profiles[†].

Light wavelength λ (nm)	*F* factor			K_{CV} factor		
	p-value	*t*	df	*p*-value	*t*	df
412	0.325	1.048	8	0.876	-0.161	8
443	0.732	0.355	8	0.747	0.335	8
511	0.383	0.923	8	0.780	-0.289	8
555	0.476	0.748	8	0.901	-0.128	8
All data‡	0.117	1.609	35	0.896	-0.132	35

[†] The paired *t* test is carried for both sides at the significance level $\alpha = 0.05$.
[‡] All spectral data (412, 443, 511 and 555 nm) are considered together.

6.5. Discussion and Conclusions

We have examined for the first time the fluctuating signals in the downwelling plane irradiance depth profiles recorded by a profiling radiometer in the upper ocean using the wavelet transform method where the irradiance depth profiles (time-stamped data sequence) are treated as non-stationary time series. Unlike data from fixed-depth deployments [e.g. *Darecki et al.*, 2011; *Fraser et al.*, 1980; *Gernez and Antoine*, 2009; *Prokopov et al.*, 1975; *Snyder and Dera*, 1970; *Stramska and Dickey*, 1998], the irradiance depth profile is a realization of the dynamic light field under the influence of surface waves but along the vertical. The derived light field statistics from the depth profiles hence allow derivation of quantitative spatial information, including the vertical variation in the dominant frequency and coefficient of variation of the light field fluctuations.

In our study, the frequency of irradiance fluctuations is observed to diminish with water depth (Figure 6.7), which have been described before. In a qualitative sense, and assuming that sub-surface fluctuations are due to sea surface waves with varying periods, it is clear that large waves with longer periods have a dominant influence in deeper waters while small waves of short periods are more important sources of variability in shallower regions beneath the sea surface. This is consistent with ray models such as Eq. (6.4) in this study and those proposed before [e.g. *Walker*, 1994; *Zaneveld et al.*, 2001b] and can readily be observed in published irradiance profile data [e.g. *Schubert et al.*, 2001; *Zaneveld et al.*, 2001b; *Zibordi et al.*, 2004a]. We found, somewhat surprisingly, that a rather simple model of surface wave focusing (Eq. (6.8)), which predicts an inverse square root dependency on depth, could explain a large fraction of the vertical variance in the dominant frequencies of irradiance fluctuations in the upper ocean. Furthermore, the model can explain to a remarkable degree similar observations reported in the past from optical measurements taken from moorings at fixed depths below the surface, particularly for clear waters (Figure 6.7b) [e.g. *Fraser et al.*, 1980; *Gernez and Antoine*, 2009; *Snyder and Dera*, 1970; *Stramska and Dickey*, 1998].

We note that the parameter F in our model varies with environmental conditions such as the solar zenith angle and wave steepness [also see *Nikolayev et al.*, 1972]. In the original formulation of Eq. (6.9), for example, the F factor depends on the wave steepness $Hk/2$ for a constant solar zenith angle θ_s. The data points scattered about the fitted curves in Figure 6.7a and Figure 6.7c can be ascribed to the changing wave steepness of the instantaneous topography of sea surface. The model fitting with an estimation of F factor then relates the light field dynamics to the average steepness of

surface waves. Variation of sea wave height and/or wave period (wave length) and the wind speed causes changes in the average steepness, and henceforth variation in the F factor. Based on the estimated F factors, Eq. (6.9) can be used to estimate ratios of wave height H to wavelength Λ of 0.099 and 0.117 for the Pacific experiment and SBC experiment, respectively. According to *Kumar et al.* [2009], the wave steepness is associated with several critical parameters of the wave field, including the significant wave height, dominant period and wind speed, $\delta = \omega_p^{5/2} H_s U_{10}^{1/2} g^{-3/2}$, where δ is the wave steepness parameterized as the ratio of H to Λ, ω_p is the dominant angular frequency, and H_s is the significant wave height. Direct measurements of the surface wave height field from the laser altimeter [*Zappa et al.*, 2012] resulted in derived δ = 0.094 and δ = 0.195 for the Pacific and SBC experiments respectively which is in remarkable agreement with our results based solely on optical variation.

With Eq. (6.16), we calculated the variance profile Var[I_n] by averaging the variance between 0.25-4 s periods from the wavelet spectrum, which are found to represent >95% of the variance. The coefficient of variation is then described as an inverse square root function of the water depth (Eq. (6.18); Figure 6.8). As with the dominant frequency, the simple model also explains a large amount of the vertical variance in other studies which utilized fixed-depth time series data [e.g. *Darecki et al.*, 2011; *Fraser et al.*, 1980; *Gernez and Antoine*, 2009; *Gernez et al.*, 2011; *Snyder and Dera*, 1970; *Stramska and Dickey*, 1998], but provides quantitative details along the water column of interest. Our depth-profile derivations sometimes exhibit maxima in the coefficient of variation between 1-3 m depth (e.g. Figure 6.8c). The occurrence of local maximum CV at shallow depths is theoretically possible [*Weber*, 2010]. The estimation of the total variance very near the

sea-surface could be biased because we did not resolve the smallest of wave fluctuations (see below) and as a consequence, we only utilized data deeper than three meters in fitting Eq. (6.18) to our data. Unlike the dominant frequency observations, we have no simple mechanistic model of the variance that relates the observed inverse square root dependency on the surface wave field. There are several issues which merit further discussion.

Like commonly used underwater radiometers, our instrument has a data acquisition rate of less than 10 Hz and hence does not resolve the fastest light flashes that exist. For example, the capillary waves (less than 1.73cm in length) could play a role in the underwater irradiance field distribution. They may produce "light flashes" with durations as short as tens of milliseconds [*Stramski and Dera*, 1988] in near surface layers. However, the capillary waves do not generate the dominant signals in the measured light field fluctuations for deeper waters, where it is valid to consider only the gravity waves in Eq. (6.8) when modeling the wave-induced irradiance fluctuations and distributions.

Measurement of these fast-changing light signals requires radiometers with higher acquisition rate such as the “Porcupine” [e.g. *Darecki et al.*, 2011]. However the dominant frequency of irradiance fluctuations as derived from the power spectra of irradiance data rarely exceeds 3 Hz. Rather, it usually falls within a range of low-frequency bands, for example, ~1-1.2 Hz within water depths of 0.5-2 m [*Dera and Stramski*, 1986] and 1.1-2.5 Hz within 0.86-2.84 m water depths [*You et al.*, 2010]. We believe that our instrument with the sampling frequency of 7 Hz is sufficient to capture the dominant signals in the temporal domain, but to be safe, have restricted our analysis to waters greater than 3 meters of depth.

Another problem associated with the sampling frequency is its potential influence on the variance of measured irradiance fluctuations at the very shallow depths [e.g. *Darecki et al.*, 2011; *Dera and Stramski*, 1986]. Examination of the irradiance time series sampled at 1 kHz [*You et al.*, 2010] shows that the proportion of the variance lying within the frequency band less than 7 Hz increases from about 50% at 0.86 m, the shallowest depth modeled, to 92% at 2.85 m. We conclude that an instrument with a sample frequency of 7 Hz is sufficient to measure the total variance of the irradiance fluctuations in waters greater than 3 meters.

The area of the diffuser of the radiometer is also crucial in analysis of the irradiance fluctuations at small water depths. The larger the area, the more that the very high frequency and high wavenumber irradiance fluctuations are depressed [*Dera and Stramski*, 1986]. Recent study has suggested that the irradiance fluctuations as measured below 2 m depths are generally independent of the surface area of the diffuser [*Darecki et al.*, 2011]. When the sea is covered by large gravity waves, for example, the fluctuating light signals are less sensitive to the area of the diffuser, which is an appropriate spatial integrator and interpretation of the depth evolution of the coefficient of variation in waters deeper than 3 meters (Figure 6.8).

The fall velocity of the instrument in the water column is another factor which can potentially impact the analysis of irradiance fluctuations. The instrument in our experiments fell at about 0.2-0.3 m/s; the irradiance field was sampled every 5 cm along the vertical. According to our study, this strategy is sufficient for sampling the spatial (vertical) variation of the irradiance fluctuations. We do not know yet the maximum allowed fall speed that can be adopted for representative sampling of light field

fluctuations in irradiance profiles. The basic principle is that the slower the instrument falls, the more information will be resolved along the vertical.

The surface wave field includes the combined effect of waves of many different wavelengths, traveling through each other at different phase speeds, i.e., are dispersive, and sometimes travelling in different directions [*Jelley*, 1989]. The differences observed in the coefficients of variation between the replicate irradiance profiles (data not shown), and between the matchups of irradiance depth profiles and fixed-position time series (Figure 6.10), to the first order, could be ascribed to the focusing effects of light by differing instantaneous sea surface topography. But, the consistency between such data pairs is strongly suggestive of the same statistics for the dynamic air-sea boundary. The finding of consistent mean irradiance values (Figure 6.10c) is in agreement with previous reports [*Zibordi et al.*, 2009].

Our theoretical development of the dominant frequency distribution is suggestive of dependence on environmental conditions such as the solar zenith angle and wave slopes [also see *Nikolayev et al.*, 1972]. The data presented in our study represent the dynamic light field under distinctive conditions. For example, low solar zenith angles (~32°) and moderate sea states were met in the Pacific experiment, while larger solar zeniths (~48°) and relatively calmer sea states were observed in the field expedition in the Santa Barbara Channel. Since these controlling factors in our experiment varied over a very small range, the available information of the environmental dependence is limited. The two study areas discussed above differ with respect to the spectral distribution of the diffuse attenuation coefficient (Figure 6.4b), but show the same spectral dependence for the scattering coefficient (Figure 6.4c). The dominant frequencies of irradiance fluctuations

are independent of optical wavelength, in accordance with previous reports [e.g. *Darecki et al.*, 2011; *Gege and Pinnel*, 2011; *Gernez and Antoine*, 2009; *Stramska and Dickey*, 1998]. However, the rate of change in the variance with depth does show a spectral dependency, and decreases with increasing optical wavelength. The scattering at these four wavebands seems important in determining the vertical rate of change of the variance, since the optical scattering tends to smear out the contrast of the light field signals [*Wells*, 1973], and bring down the variance of fluctuating irradiance field. The SBC water has a mean scattering coefficient and scattering albedo much higher than the Pacific water (Figure 6.4c and Figure 6.4d) and henceforth could lead to much more attenuated variability (Figure 6.9b). The spectrally decreasing sky diffuseness (Figure 6.4a) is partly responsible as well [*Stramski*, 1986b], but probably to a smaller degree [*Gege and Pinnel*, 2011].

Chapter 7. Conclusions

This thesis work is a continuation of studies on the optical aspects of oceanography, with an attempt to quantify the radiance distribution and its variation in the ocean. I have particularly dealt with the problem of instrumentation for measuring the high dynamic range radiance field and the interpretation of the mean and variance of the light field as measured in the dynamic ocean environment. In this brief closing chapter, I summarize the findings and contributions and investigate their potential for future improvements and applications.

7.1. Findings and Contributions

Development of the high dynamic range radiance camera radiometer is a critical improvement to underwater optical radiometry (Chapter 3). The camera radiometer is built on the fisheye lens and CMOS imaging technologies and designed to measure the light field in the hemispheric space. Two coupled cameras map the full light field. The high dynamic range nonlinear response function is a rare practice in ocean optical radiometry and the calibration is challenging. Other components potentially affecting the measurement uncertainties, such as the immersion factor, point spread function, and polarization effect, are also taken into account in the calibrations. The high intra-scene dynamic range over 10^6 and system dynamic range over 10^9 makes this camera unique among all existing oceanographic radiometers. The camera system has a nominal spatial resolution better than 0.5° along the zenith direction and a fast sampling frequency (up to 15 Hz).

The calibrated camera is consequently capable of measuring the radiance distribution in absolute units in $\mu Wcm^{-2}sr^{-1}nm^{-1}$ in the strongest and highly dynamic air-ocean boundary layers, without the need of occulting the sun. One can profile the water column for the highly contrasting light field from just below the sea surface to depths on the order of 100 meters. Comparison of the camera's measurements with the standard ocean color radiometer suggests a good agreement.

Refinement of the knowledge follows closely behind the introduction of the new scientific instrument. We have now been able to quantify the mean light field in the upper ocean water column based on the measured fine structure of the radiance field, which may vary dramatically when viewed from different directions (Chapter 4). This characteristic directionality represents some of the most fundamental properties of the ambient light field. Based on the radiance distribution, we have derived and characterized all types of irradiances, *K* functions and distribution functions as a function of water depth and water types.

Some of the derivations of the mean light field are qualitatively in agreement with historical data; but our study has provided unprecedented and complete details and quantitative information on the light field structure. For example, the radiance distribution may be inverted to obtain the absorption coefficient of sea water from Gershun's law throughout the upper water column. The variation of the downwelling average cosine is shown to be dependent on sea water types. The simultaneous measurements of the sky radiance distribution and the underwater radiance distribution allow for a detailed model validation.

The wave-induced variability in the radiance distribution in near-surface ocean water is an extremely significant finding. Effort is particularly made to gain insights into this dynamic light field (Chapter 5). We have determined the radiance fluctuations in every direction as well as the irradiance and average cosine fluctuations in terms of the probability distribution, periodicity and amplitude of the variation. We have found that both the radiance and irradiance fluctuations at shallow depths can be described as a process following the lognormal distribution. The variation of the radiance is anisotropic with regard to its amplitude and periodicity; both have been shown to relate directly to the sea wave field. The irradiance tends to vary at faster frequency than radiance in the surface water. The dispersion of the downwelling average cosine fluctuations is found to increase with the solar zenith angle but generally varies less than 10% in the ocean surface environment.

The highly resolved radiance measurements (in time and space domains) presented in Chapter 5 have unraveled some of the most fundamental features pertinent to the structure of the dynamic radiance field. The differential variability of the directional radiance including the extreme CV pattern, bi-model pattern, and the distribution pattern of the maximum radiance all have relevance to the surface waves. The closeness in their dominant frequencies is another direct consequence of the wave modulation of the light field. Our study has also revealed the inherent difference in the radiance variability and irradiance variability, probably because the former is confined within a certain usually small solid angle while the latter is integrated over the hemisphere (180 degree).

The study on the wave-induced irradiance field (Chapter 6) is pursued not from the fixed-depth time series, but with the irradiance depth profiles obtained when profiling the

upper water column with a commercial irradiance sensor. The analyses show that the periodicity and amplitude of the wave-induced irradiance fluctuations are imbedded in the irradiance depth profiles. We have demonstrated that the normalized and detrended continuous irradiance depth profiles might be decomposed into fluctuations in the time-frequency domain. The dominant frequencies and the coefficient of variation, are further isolated from the irradiance profile decompositions. The derivations are consistent with the fixed-depth time series data.

One contribution of this specific study is that we have found the irradiance depth profiles can be used to derive the light field statistics quantitatively and as accurately as from fixed-depth time series deployments, which extend from the surface to depths of the water column. These signals in the depth profiles were thought unpredictable and more often treated as noise. The irradiance distributions are spatially (in the vertical) evolving and inter-connected in the depth profiles, and we have established the connections between these variations and the surface wave field.

7.2. Future Prospects

The radiance distribution as a function of depth and time are the most basic radiometric quantities for describing the structure of the solar radiation in the upper layers of the ocean. With the demonstrated techniques, we are now at a threshold of obtaining more complete data of the angular structure of the solar radiant energy in the upper ocean. It will greatly expand the applicability of the introduced technique of instrumentation by further development with spectral resolving power. The spectral radiance field will provide the most complete information necessary for understanding the light propagation..

A surge of work is expected when the measurements of the entire underwater daylight structure in the upper ocean water column become available. The advanced forward radiative transfer models can be validated against the radiance distribution measurements [e.g. *Mobley et al.*, 1993]. Many optical models predict the relationship between the inherent optical properties and the average cosines [*Bannister*, 1992; *Hirata*, 2003; *Kirk*, 1991, 1999; *Talaulikar et al.*, 2012], but, are rarely tested against data. The scattering phase function is the most rarely measured quantity among the inherent optical properties. It is of great interest to experiment with the radiance distribution data and simultaneous measurements of the beam attenuation coefficient and absorption coefficient, since it is possible to derive the scattering phase function of the hydrosols from radiance distribution data [*Zaneveld*, 1974].

Future studies should also consider the fast variability of the light field in that the dynamic processes of the light field are important as a tool to investigate the light-wave relationship [*Jähne et al.*, 1994], biologically, and probably in many other aspects [*Dickey et al.*, 2011]. For example, our study has identified some of the conspicuous features from the radiance field which apparently relate to the surface waves. The question is, at this point, how one can confidently derive or describe the surface wave slopes from the knowledge of the underwater radiance time series data. Increasing the spatial resolution (angular resolution) and the temporal resolution of the radiance camera may help answer this question. Little is known yet of the response of living organisms and animals to the fast fluctuating light field. For example, marine animals may be sensitive to and utilize the spatial patterns of the variance and periodicity of the angular structure of the solar radiation [e.g. *Sabbah et al.*, 2012].

The research presented in this thesis provides invaluable theoretical and quantitative context in which it is of interest to further explore these important oceanographic questions.

Appendix A. Copyright Agreement Letters

1. Copyright Release Letter - 1

From: pubscopyright <copyright@osa.org> Thu, Jan 3, 2013 at 3:31 PM

To: Jianwei Wei <Jianwei.Wei@dal.ca>

Subject: copyright release request

Dear Dr. Wei,

Thank you for contacting The Optical Society.

Because you are the author of the source paper from which you wish to reproduce material, OSA considers your requested use of its copyrighted materials to be permissible within the author rights granted in the Copyright Transfer Agreement submitted by the requester on acceptance for publication of his/her manuscript. It is requested that a complete citation of the original material be included in any publication. This permission assumes that the material was not reproduced from another source when published in the original publication.

Please let me know if you have any questions.

Kind Regards,

Susannah Lehman

January 3, 2013

Authorized Agent, The Optical Society

---------- The above is a response to the copyright request email ----------

From: Jianwei Wei <Jianwei.Wei@dal.ca> Fri, Dec 21, 2012 at 2:19 PM

To: copyright@osa.org

Subject: copyright release request

Dear Sir or Madame,

I am preparing my PhD thesis for submission to the Faculty of Graduate Studies at Dalhousie University, Halifax, Nova Scotia, Canada. I am seeking your permission to include a manuscript version of the following paper as a chapter in the thesis:

> A new instrument for measuring the high dynamic range radiance distribution in near-surface sea water. Jianwei Wei, Ronnie Van Dommelen, Marlon Lewis, Scott McLean, and Kenneth Voss, *Optics Express*, vol.20, no.24, 27024-27038, 2012

Canadian graduate theses are reproduced by the Library and Archives of Canada (formerly National Library of Canada) through a non-exclusive, world-wide license to reproduce, loan, distribute, or sell theses. I am also seeking your permission for the material described above to be reproduced and distributed by the LAC (NLC). Further details about the LAC (NLC) thesis program are available on the LAC(NLC) website (www.nlc-bnc.ca).

Full publication details and a copy of this permission letter will be included in the thesis.

Yours sincerely,

Jianwei Wei

Department of Oceanography

Dalhousie University

Halifax, Nova Scotia, B3H 4R2, Canada

2. Copyright Release Letter - 2

From: Jeanette Panning <JPanning@agu.org> Fri, Dec 21, 2012 at 2:47 PM

To: "Jianwei.Wei@dal.ca" <Jianwei.Wei@dal.ca>

Dear Dr. Wei,

We are pleased to grant permission for the use of the material requested for inclusion in your thesis. The following non-exclusive rights are granted to AGU authors:

- All proprietary rights other than copyright (such as patent rights).
- The right to present the material orally.
- The right to reproduce figures, tables, and extracts, appropriately cited.
- The right to make hard paper copies of all or part of the paper for classroom use.
- The right to deny subsequent commercial use of the paper.

Further reproduction or distribution is not permitted beyond that stipulated. The copyright credit line should appear on the first page of the article or book chapter. The following must also be included, "Reproduced by permission of American Geophysical Union." To ensure that credit is given to the original source(s) and that authors receive full credit through appropriate citation to their papers,

We recommend that the full bibliographic reference be cited in the reference list. The standard credit line for journal articles is: "Author(s), title of work, publication title, volume number, issue number, citation number (or page number(s) prior to 2002), year. Copyright [year] American Geophysical Union."

If an article was placed in the public domain, in which case the words "Not subject to U.S. copyright" appear on the bottom of the first page or screen of the article, please substitute "published" for the word "copyright" in the credit line mentioned above.

Copyright information is provided on the inside cover of our journals. For permission for any other use, please contact the AGU Publications Office at AGU, 2000 Florida Ave., N.W., Washington, DC 20009.

Best wishes,

Jeanette

Jeanette Panning

Manager Editor Coordination

American Geophysical Union

+1.202.777.7382

JPanning@agu.org

www.agu.org

---------- The above is a response to the copyright request email ----------

From: Jianwei Wei <Jianwei.Wei@dal.ca> Fri, Dec 21, 2012 at 2:35 PM

To: author.help@agu.org

Subject: copyright release request

Dear Sir or Madame,

I am preparing my PhD thesis for submission to the Faculty of Graduate Studies at Dalhousie University, Halifax, Nova Scotia, Canada. I am seeking your permission to include a manuscript version of the following paper as a chapter in the thesis:

> Quantitative estimation of the underwater radiance distribution. Marlon Lewis, Jianwei Wei, Ronnie Van Dommelen, and Kenneth J. Voss. *Journal of Geophysical Research*, vol.116, C00H06, doi:10.1029/2011JC007275, 2011

Canadian graduate theses are reproduced by the Library and Archives of Canada (formerly National Library of Canada) through a non-exclusive, world-wide license to reproduce, loan, distribute, or sell theses. I am also seeking your permission for the material described above to be reproduced and distributed by the LAC (NLC). Further details about the LAC (NLC) thesis program are available on the LAC(NLC) website (www.nlc-bnc.ca).

Full publication details and a copy of this permission letter will be included in the thesis.

Yours sincerely,

Jianwei Wei

Department of Oceanography

Dalhousie University

Halifax, Nova Scotia, B3H 4R2, Canada

References

Aas, E., and N. K. Højerslev (1999), Analysis of underwater radiance observations: apparent optical properties and analytic functions describing the angular radiance distribution, *J. Geophys. Res.*, *104*(C4), 8015-8024.

Ackleson, S. G. (2001), Ocean optics research at the start of the 21st century, *Oceanography*, *14*(3), 5-8.

Adams, J. T., E. Aas, N. K. Hjøerslev, and B. Lundgren (2002), Comparison of radiance and polarization values observed in the Mediterranean Sea and simulated in a Monte Carlo model, *Appl. Opt.*, *41*(15), 2724-2733.

Aldrich, J. (1997), R. A. Fisher and the making of maximum likelihood 1912-1922, *Stat. Sci.*, *12*(3), 162-176.

Anderson, C. R., D. A. Siegel, M. A. Brzezinski, and N. Guillocheau (2008), Controls on temporal patterns in phytoplankton community structure in the Santa Barbara Channel, California, *J. Geophys. Res.*, *113*(C04038), doi:10.1029/2007JC004321.

Antoine, D., A. Morel, and E. Leymarie (2013), Underwater radiance distributions measured with miniaturized multispectral radiance cameras, *J. Atmos. Oceanic Tech.*, *30*(1), 74-95.

Austin, R. W. (1974), The remote sensing of spectral radiance from below the ocean surface, in *Optical Aspects of Oceanography*, edited by N. G. Jerlov and E. Steemann Nielsen, pp. 317-344, Academic Press, New York.

Bannister, T. T. (1992), Model of the mean cosine of underwater radiance and estimation of underwater scalar irradiance, *Limnol. Oceanogr.*, *37*(4), 773-780.

Behrenfeld, M. J., and P. G. Falkowski (1997), Photosynthetic rates derived from satellite-based chlorophyll concentration, *Limnol. Oceanogr.*, *42*(1), 1-20.

Berwald, J., D. Stramski, C. D. Mobley, and D. A. Kiefer (1995), Influences of absorption and scattering on vertical changes in the average cosine of the underwater light field, *Limnol. Oceanogr.*, *40*(8), 1347-1357.

Boynton, G. C., and H. R. Gordon (2002), Irradiance inversion algorithm for absorption and backscattering profiles in natural waters: improvement for clear waters, *Appl. Opt.*, *41*(12), 2224-2227.

Bréon, F. M., and N. Henriot (2006), Spaceborne observations of ocean glint reflectance and modeling of wave slope distributions, *J. Geophys. Res.*, *111*(C06005), doi:10.1029/2005JC003343.

Chang, G. C., A. H. Barnard, S. McLean, P. J. Egli, C. Moore, J. R. V. Zaneveld, T. D. Dickey, and A. Hanson (2006), In situ optical variability and relationships in the Santa Barbara Channel: implications for remote sensing, *Appl. Opt.*, *45*(15), 3593-3604.

Collins, D. G., W. G. Blättner, M. B. Wells, and H. G. Horak (1972), Backward Monte Carlo calculations of the polarization characteristics of the radiation emerging from spherical-shell atmospheres, *Appl. Opt.*, *11*(11), 2684-2696.

Cox, C., and W. Munk (1954), Statistics of the sea surface derived from sun glitter, *J. Mar. Res.*, *13*(2), 198-227.

Cox, C., and W. Munk (1956), Slopes of the sea surface deduced from photographs of sun glitter, *Bull. Scripps Inst. Oceanogr. Univ. Calif.*, *6*(9), 401-488.

Cullen, J. J., A. M. Ciotti, R. F. Davis, and M. R. Lewis (1997), Optical detection and assessment of algal blooms, *Limnol. Oceanogr.*, *42*(5), 1223-1239.

Darecki, M., D. Stramski, and M. Sokolski (2011), Measurements of high-frequency light fluctuations induced by sea surface waves with an underwater porcupine radiometer system, *J. Geophys. Res.*, *116*(C00H09), doi:10.1029/2011JC007338.

Dera, J., and H. R. Gordon (1968), Light field fluctuations in the photic zone, *Limnol. Oceanogr.*, *13*(4), 697-699.

Dera, J., and D. Stramski (1986), Maximum effects of sunlight focusing under a wind-disturbed sea surface, *Oceanologia*, *23*, 15-42.

Dera, J., S. Sagan, and D. Stramski (1993), Focusing of sunlight by sea surface waves: new results from the Black Sea, *Oceanologia*, *34*, 13-25.

Deser, C., M. A. Alexander, S.-P. Xie, and A. S. Phillips (2010), Sea surface temperature variability: patterns and mechanisms, *Annu. Rev. Mar. Sci.*, *2*, 115-143.

Dickey, T. D., and G. C. Chang (2001), Recent advances and future visions: temporal variability of optical and bio-optical properties of the ocean, *Oceanography*, *14*(3), 15-29.

Dickey, T. D., and P. G. Falkowski (2002), Solar energy and its biological-physical interactions in the sea, in *The Sea*, edited by A. R. Robinson, J. J. McCarthy and B. J. Rothschild, pp. 401-440, John Wiley & Sons, Inc., New York.

Dickey, T. D., G. W. Kattawar, and K. J. Voss (2011), Shedding new light on light in the ocean, *Phys. Today*, *64*(4), 44-49.

Dickey, T. D., et al. (2012), Introduction to special section on recent advances in the study of optical variability in the near-surface and upper ocean, *J. Geophys. Res.*, *117*(C00H20), doi:10.1029/2012JC007964.

Dierssen, H. M., R. M. Kudela, J. P. Ryan, and R. C. Zimmerman (2006), Red and black tides: quantitative analysis of water-leaving radiance and perceived color for phytoplankton, colored dissolved organic matter, and suspended sediments, *Limnol. Oceanogr.*, *51*(6), 2646-2659.

Du, H., and K. J. Voss (2004), Effects of point-spread function on calibration and radiometric accuracy of CCD camera, *Appl. Opt.*, *43*(3), 665-670.

Duntley, S. Q. (1959), The underwater radiance distribution problem, *SIO Ref. Ser.*, *3-6*, 1-8.

Duntley, S. Q., R. J. Uhl, R. W. Austin, A. R. Boileau, and J. E. Tyler (1955), An underwater photometer, *J. Opt. Soc. Am.*, *45*(10), 904A.

Ebuchi, N., H. Kawamura, and Y. Toba (1987), Fine structure of laboratory wind-wave surfaces studied using an optical method, *Bound.-Lay. Meteorol.*, *39*(1-2), 133-151.

Falkowski, P. G. (1984), Physiological responses of phytoplankton to natural light regimes, *J. Plankton Res.*, *6*(2), 295-307.

Falkowski, P. G., E. A. Laws, R. T. Barber, and J. W. Murray (2003), Phytoplankton and their role in primary, new, and export production, in *Ocean Biogeochemistry: The Role of the Ocean Carbon Cycle in Global Change*, edited by M. J. R. Fasham, pp. 99-121, Springer-Verlag Berlin Heidelberg.

Fedorov, A. V., and W. K. Melville (1998), An experimental and numerical study of parasitic capillary waves, *Phys. Fluids*, *10*(6), 1315-1323.

Fraser, A. B., R. E. Walker, and F. C. Jurgens (1980), Spatial and temporal correlation of underwater sunlight fluctuations in the sea, *IEEE J. Ocean. Eng.*, *5*(3), 195-198.

Gege, P., and N. Pinnel (2011), Sources of variance of downwelling irradiance in water, *Appl. Opt.*, *50*(15), 2192-2203.

Gernez, P., and D. Antoine (2009), Field characterization of wave-induced underwater light field fluctuations, *J. Geophys. Res.*, *114*(C06025), doi:10.1029/2008JC005059.

Gernez, P., D. Stramski, and M. Darecki (2011), Vertical changes in the probability distribution of downward irradiance within the near-surface ocean under sunny conditions, *J. Geophys. Res.*, *116*(C00H07), doi:10.1029/2011JC007156.

Gershun, A. A. (1939), The light field (translated in English by P. Moon and G. Timoshenko), *J. Math. Phys.*, *18*, 51-151.

Gordon, H. R. (1989), Can the Lambert-Beer law be applied to the diffuse attenuation coefficient of ocean water? *Limnol. Oceanogr.*, *34*(8), 1389-1409.

Gordon, H. R. (2002), Inverse methods in hydrologic optics, *Oceanologia*, *44*(1), 9-58.

Gordon, H. R., and A. Morel (1983), *Remote Assessment of Ocean Color for Interpretation of Satellite Visible Imagery: A Review*, 114 pp., Springer-Verlag, New York.

Gordon, H. R., and K. Ding (1992), Self-shading of in-water optical instruments, *Limnol. Oceanogr.*, *37*(3), 491-500.

Gordon, H. R., and G. C. Boynton (1998), Radiance-irradiance inversion algorithm for estimating the absorption and backscattering coefficients of natural waters: vertically stratified water bodies, *Appl. Opt.*, *37*(18), 3886-3896.

Gordon, H. R., J. M. Smith, and O. B. Brown (1971), Spectra of underwater light-field fluctuations in the photic zone, *Bull. Mar. Sci.*, *21*(2), 466-470.

Gordon, H. R., M. R. Lewis, S. D. McLean, M. S. Twardowski, S. A. Freeman, K. J. Voss, and G. C. Boynton (2009), Spectra of particulate backscattering in natural waters, *Opt. Express*, *17*(18), 16192-16208.

Greene, R. M., and V. A. Gerard (1990), Effects of high-frequency light fluctuations on growth and photoacclimation of the red alga Chondrus crispus, *Mar. Biol.*, *105*(2), 337-344.

Gregg, W. W., and K. L. Carder (1990), A simple spectral solar irradiance model for cloudless maritime atmospheres, *Limnol. Oceanogr.*, *35*(8), 1657-1675.

Grinsted, A., J. C. Moore, and S. Jevrejeva (2004), Application of the cross wavelet transform and wavelet coherence to geophysical time series, *Nonlinear Proc. Geoph.*, *11*(5/6), 561-566.

Harrison, A. W., and C. A. Coombes (1988), An opaque cloud cover model of sky short wavelength radiance, *Sol. Energy*, *41*(4), 387-392.

Hieronymi, M., A. Macke, and O. Zielinski (2012), Modeling of wave-induced irradiance variability in the upper ocean mixed layer, *Ocean Sci. Discuss.*, *8*(2), 103-120.

Hirata, T. (2003), Irradiance inversion theory to retrieve volume scattering function of seawater, *Appl. Opt.*, *42*(9), 1564-1573.

Hirata, T., and N. K. Højerslev (2008), Relationship between the irradiance reflectance and inherent optical properties of seawater, *J. Geophys. Res.*, *113*(C3), doi:10.1029/2007JC004325.

Hirata, T., N. Hardman-Mountford, J. Aiken, and J. Fishwick (2009), Relationship between the distribution function of ocean nadir radiance and inherent optical properties for oceanic waters, *Appl. Opt.*, *48*(17), 3129-3138.

Hofmann, H., A. Lorke, and F. Peeters (2008), Temporal scales of water-level fluctuations in lakes and their ecological implications, *Hydrobiologia*, *613*(1), 85-96.

Højerslev, N. K., and J. R. V. Zaneveld (1977), A theoretical proof of the existence of the submarine asymptotic daylight field, *34*, 16 pp, Department of Physical Oceanography, University of Copenhagen, Copenhagen.

Hubbard, B. E., P. W. Carter, and D. M. Milder (2006), The virtual periscope, in *Ocean Optics XVIII*, edited, Montreal, Canada.

Hwang, P. A. (1999), Microstructure of ocean surface roughness: a study of spatial measurement and laboratory investigation of modulation analysis, *J. Atmos. Oceanic Tech.*, *16*(11), 1619-1629.

Hwang, P. A. (2002), Phase distribution of small-scale ocean surface roughness, *J. Phys. Oceanogr.*, *32*(11), 2977-2987.

Jähne, B., J. Klinke, and S. Waas (1994), Imaging of short ocean wind waves: a critical theoretical review, *J. Opt. Soc. Am. A.*, *11*(8), 2197-2209.

Jassby, A. D., and T. Platt (1976), Mathematical formulation of the relationship between photosynthesis and light for phytoplankton, *Limnol. Oceanogr.*, *21*(4), 540-547.

Jelley, J. V. (1989), Sea waves: their nature, behaviors, and practical importance, *Endeavour*, *13*(4), 148-156.

Jerlov, N. G. (1976), *Marine Optics*, 231 pp., Elsevier Scientific Publishing Company, Amsterdam.

Jerlov, N. G., and M. Fukuda (1960), Radiance distribution in the upper layers of the sea, *Tellus*, *12*(3), 348-355.

Jerlov, N. G., and K. Nygård (1968), Inherent optical properties computed from radiance measurements in the Baltic, *1*, 6 pp, Institut For Fysisk Oceanografi, Copenhagen.

Johnsen, S., and H. M. Sosik (2004), Shedding light on light in the ocean, *Oceanus*, *43*(2), 1-5.

Johnson, N. G., and G. Liljequist (1938), On the angular distributions of submarine daylight and on the total submarine illumination, *Sven. Hydrogr. - Biol. Komm. Skr., Ny Ser. Hydrogr.*, *14*, 1-15.

Kattawar, G. W., and G. N. Plass (1976), Asymptotic radiance and polarization in optically thick media: ocean and clouds, *Appl. Opt.*, *15*(12), 3166-3178.

Kirk, J. T. O. (1981), Monte Carlo study of the nature of underwater light field in, and the relationships between optical properties of, turbid yellow waters, *Aust. J. Mar. Freshwater Res.*, *32*(4), 517-532.

Kirk, J. T. O. (1991), Volume scattering function, average cosines, and the underwater light field, *Limnol. Oceanogr.*, *36*(3), 455-467.

Kirk, J. T. O. (1994), *Light and Photosynthesis in Aquatic Ecosystems*, Second ed., 509 pp., Cambridge University Press.

Kirk, J. T. O. (1999), Multiple scattering of a photon flux: implications for the integral average cosine of the underwater light field, *Appl. Opt.*, *38*(15), 3134-3140.

Kirk, J. T. O. (2004), Monte Carlo modelling of radiative transfer in the ocean, in *Short courses presented at Ocean Optics XVII*, edited, p. 72, Fremantle, Australia.

Kumar, R. R., B. P. Kumar, A. N. V. Satyanarayana, D. B. Subrahamanyam, A. D. Rao, and S. K. Dube (2009), Parameterization of sea surface drag under varying sea state and its dependence on wave age, *Nat. Hazards.*, *49*(2), 187-197.

Leathers, R. A., T. V. Downes, C. O. Davis, and C. D. Mobley (2004), Monte Carlo radiative transfer simulations for ocean optics: a practical guide, memorandum report, 54 pp, Office of Naval Research, Arlington, VA.

Lee, Z., K. L. Carder, C. D. Mobley, R. G. Steward, and J. S. Patch (1999), Hyperspectral remote sensing for shallow wWaters. 2. Deriving bottom depths and water properties by optimization, *Appl. Opt.*, *38*(18), 3831-3843.

Lee, Z., et al. (2011), An assessment of optical properties and primary production derived from remote sensing in the Southern Ocean (SO GasEx), *J. Geophys. Res.*, *116*(C00F03), doi: 10.1029/2010JC006747.

Lewis, M. R., N. Kuring, and C. Yentsch (1988), Global patterns of ocean transparency: implications for the new production of the open ocean, *J. Geophys. Res.*, *93*(C6), 6847-6856.

Lewis, M. R., D. Hebert, W. G. Harrison, T. Platt, and N. S. Oakey (1986), Vertical nitrate fluxes in the oligotrophic ocean, *Science*, *234*(4778), 870-873.

Lewis, M. R., M.-E. Carr, G. C. Feldman, W. Esaias, and C. McClain (1990), Influence of penetrating solar radiation on the heat budget of the equatorial Pacific Ocean, *Nature*, *347*(6293), 543-545.

Leymarie, E., D. Doxaran, and M. Babin (2010), Uncertainties associated to measurements of inherent optical properties in natural waters, *Appl. Opt.*, *49*(28), 5415-5436.

Limpert, E., W. A. Stahel, and M. Abbt (2001), Log-normal distributions across the sciences: keys and clues, *Bioscience*, *51*(5), 341-352.

Litchman, E. (2000), Growth rates of phytoplankton under fluctuating light, *Freshwater Biol.*, *44*(22), 223-235.

Longuet-Higgins, M. S. (1963), The generation of capillary waves by steep gravity waves, *J. Fluid Mech.*, *240*, 138-159.

Longuet-Higgins, M. S. (1995), Parasitic capillary waves: a direct calculation, *J. Fluid Mech.*, *301*, 79-107.

Lundgren, B., and N. K. Højerslev (1971), Daylight measurements in the Sargasso sea. Results from the "Dana" expedition (January-April 1966), *14*, 44 pp, Department of Physical Oceanography, University of Copenhagen, Copenhagen.

Lynch, D. K., D. S. P. Dearborn, and J. A. Lock (2011), Glitter and glints on water, *Appl. Opt.*, *50*(28), F39-F49.

Maffione, R. A. (2001), Evolution and revolution in measuring ocean optical properties, *Oceanography*, *14*(3), 9-14.

Mäthger, L. M. (2003), The response of squid and fish to changes in the angular distribution of light, *J. Mar. Biol. Ass. U.K.*, *83*(4), 849-856.

McCormick, N. J. (2004), Analytic inverse radiative transfer equations for atmospheric and hydrologic optics, *J. Opt. Soc. Am. A.*, *21*(6), 1009-1017.

McFarland, W. N., and E. Loew (1983), Wave produced changes in underwater light and their relations to vision, *Env. Biol. Fish.*, *8*(3/4), 173-184.

McLean, J. W., and J. D. Freeman (1996), Effects of ocean waves on airborne lidar imaging, *Appl. Opt.*, *35*(18), 3261-3269.

Minnaert, M. (1954), *The Nature of Light and Color in the Open Air*, 390 pp., Dover Publications Inc., New York.

Miyamoto, K. (1964), Fish eye lens, *J. Opt. Soc. Am.*, *54*(8), 1060-1061.

Mobley, C. D. (1989), A numerical model for the computation of radiance distributions in natural waters with wind-roughened surfaces, *Limnol. Oceanogr.*, *34*(8), 1473-1483.

Mobley, C. D. (1994), *Light and Water: Radiative Transfer in Natural Waters*, 592 pp., Academic Press, Inc., San Diego, California.

Mobley, C. D., and R. W. Preisendorfer (1988), A numerical model for the computation of radiance distributions in natural waters with wind-roughened surfaces, in *NOAA Technical Memorandum ERL PMEL-75*, edited, p. 195, Pacific Marine Environmental Laboratory, Seattle, WA.

Mobley, C. D., and L. K. Sundman (2008), Hydrolight 5 and Ecolight 5 user's guide, edited, Sequoia Scientific, Inc., Bellevue, WA.

Mobley, C. D., B. Gentili, H. R. Gordon, Z. H. Jin, G. W. Kattawar, A. Morel, P. Reinersman, K. Stamnes, and R. H. Stavn (1993), Comparison of numerical models for computing underwater light fields, *Appl. Opt.*, *32*(36), 7484-7504.

Moore, C., A. Barnard, P. Fietzek, M. R. Lewis, H. M. Sosik, S. White, and O. Zielinski (2009), Optical tools for ocean monitoring and research, *Ocean Sci.*, *5*(4), 661-684.

Morel, A. (1974), Optical properties of pure water and pure sea water, in *Optical Aspects of Oceanography*, edited by N. G. Jerlov and E. Steemann Nielsen, p. 494, Academic Press Inc, New York, NY.

Morel, A. (1991), Light and marine photosynthesis: a spectral model with geochemical and climatological implications, *Prog. Oceanogr.*, *26*(3), 263-306.

Morel, A., and L. Prieur (1977), Analysis of variations in ocean color, *Limnol. Oceanogr.*, *22*(4), 709-722.

Morel, A., and B. Gentili (1993), Diffuse reflectance of oceanic waters. II. Bidirectional aspects, *Appl. Opt.*, *32*(33), 6864-6879.

Morel, A., and S. Maritorena (2001), Bio-optical properties of oceanic waters: a reappraisal, *J. Geophys. Res.*, *106*(C4), 7163-7180.

Morel, A., and B. Gentili (2004), Radiation transport within oceanic (case 1) water, *J. Geophys. Res.*, *109*(C06008), doi:10.1029/2003JC002259.

Morel, A., D. Antoine, and B. Gentili (2002), Bidirectional reflectance of oceanic waters: accounting for Raman scattering and varying particle scattering phase function, *Appl. Opt.*, *41*(30), 6289-6306.

Mueller, J. L. (2003), In-water radiometric profile measurements and data analysis protocols, in *Ocean Optics Protocols for Satellite Ocean Color Sensor Validation, Revision 4*, edited by J. L. Mueller, G. S. Fargion and C. R. McClain, National Aeronautical and Space Administration, Goddard Space Flight Space Center, Greenbelt, Maryland.

Mueller, J. L., G. S. Fargion, and C. R. McClain (Eds.) (2003), *Ocean Optics Protocols for Satellite Ocean Color Sensor Validation, Revision 4*, NASA, Goddard Space Flight Center, Greenbelt, MD.

Mullamaa, Y.-A. R., and V. P. Nikolayev (1972), Fluctuations of the luminescence of the sun as measured under water, *Izv. Atmos. Ocean. Phys.*, *8*(4), 382-388.

Muller-Karger, F. E., C. Hu, S. Andrefouet, R. Varela, and R. Thunell (2005), The color of the coastal ocean and applications in the solution of research and management problems, in *Remote Sensing of Coastal Aquatic Environments: Technologies, Techniques and Applications*, edited by R. L. Miller, C. E. Del Castillo and B. A. McKee, pp. 101-127, Springer, Norwell, MA.

Nakamura, T., and H. Yamasaki (2008), Flicker light effects on photosynthesis of symbiotic algae in the reef-building coral Acropora digitifera (Cnidaria: Anthozoa: Scleractinia), *Pac. Sci.*, *62*(3), 341-350.

Nicodemus, F. E. (1978), *Self-study Manual on Optical Radiation Measurements: Part I - Concepts, Chapters 4 and 5*, 118 pp., U.S. Government Printing Office, Washington.

Nikolayev, V. P., and M. S. Khulapov (1976), Use of a nonstatistical model to explain the mechanism of underwater illumination fluctuation, *Izv. Atmos. Ocean. Phys.*, *12*(9), 993-997.

Nikolayev, V. P., and V. G. Yakubenko (1978), Experimental research into the spatial structure on the fluctuations of the underwater light field, *Izv. Atmos. Ocean. Phys.*, *14*(4), 301-305.

Nikolayev, V. P., O. I. Prokopov, G. V. Rozenberg, and V. I. Shevernev (1972), Statistical properties of the underwater illumination, *Izv. Atmos. Ocean. Phys.*, *8*(9), 936-944.

Pettersson, H. (1938), Measurements of the angular distribution of submarine light, *Rapp. Cons. Explor. Mer.*, *108*(2), 7-12.

Plass, G. N., and G. W. Kattawar (1969), Radiative transfer in an atmosphere-ocean system, *Appl. Opt.*, *8*(2), 455-466.

Plass, G. N., G. W. Kattawar, and J. A. Guinn, Jr. (1976), Radiance distribution over a ruffled sea: contributions from glitter, sky, and ocean, *Appl. Opt.*, *15*(12), 3161-3165.

Platt, T., and A. D. Jassby (1976), The relationship between photosynthesis and light for natural assemblages of coastal marine phytoplankton, *J. Phycol.*, *12*(4), 421-430.

Platt, T., and S. Sathyendranath (1988), Oceanic primary production: estimation by remote sensing at local and regional scales, *Science*, *241*(4873), 1613-1620.

Porter, W. C., B. Kopp, J. C. Dunlap, R. Widenhorn, and E. Bodegom (2008), Dark current measurements in a CMOS imager, *Proc. SPIE*, *6816*, doi:10.1117/1112.769079.

Preisendorfer, R. W. (1958a), On the existence of characteristic diffuse light in natural waters, *SIO Ref. Ser.*, *58-59*, 1-17.

Preisendorfer, R. W. (1958b), Some practical consequences of the asymptotic radiance hypothesis, *SIO Ref. Ser.*, *58-60*, 1-31.

Preisendorfer, R. W. (1959), Theoretical proof of the existence of characteristic diffuse light in natural waters, *J. Mar. Res.*, *18*(1), 1-9.

Preisendorfer, R. W. (1976), *Hydrologic Optics*, 218 pp., U.S. Government Printing Office.

Preisendorfer, R. W., and C. D. Mobley (1985), Unpolarized irradiance reflectances and glitter patterns of random capillary waves on lakes and seas, by Monte Carlo simulation,

NOAA Technical Memorandum, *ERL PMEL-63*, 141 pp, Pacific Marine Environmental Laboratory, Seattle, WA.

Priestley, M. B. (1981), *Spectral Analysis and Time Series*, 890 pp., Academic Press, London.

Prokopov, O. I., and V. P. Nikolayev (1976), A study of underwater illumination fluctuations in the Mediterranean Sea, *Izv. Atmos. Ocean. Phys.*, *12*(5), 559-563.

Prokopov, O. I., V. P. Nikolayev, A. A. Zhil'tsov, and L. M. Nesterenko (1975), Some results of a study of light field fluctuations in the sea from the "Chernomor" underwater laboratory, *Izv. Atmos. Ocean. Phys.*, *11*(11), 1179-1183.

Quéguiner, B., and L. Legendre (1986), Phytoplankton photosynthetic adaptation to high frequency light fluctuations simulating those induced by sea surface waves, *Mar. Biol.*, 482-491.

Reda, I., and A. Andreas (2004), Solar position algorithm for solar radiation applications, *Sol. Energy*, *76*(5), 577-589.

Rørslett, B., I. A. N. Hawes, and A.-M. Schwarz (1997), Features of the underwater light climate just below the surface in some New Zealand inland waters, *Freshwater Biol.*, *37*(2), 441-454.

Rudnick, D., and S. T. Cole (2011), On sampling the ocean using underwater gliders, *J. Geophys. Res.*, *116*(C08010), doi:10.1029/2010JC006849.

Ryther, J. H. (1956), Photosynthesis in the ocean as a function of light intensity, *Limnol. Oceanogr.*, *1*(1), 61-70.

Sabbah, S., and N. Shashar (2006), Underwater light polarization and radiance fluctuations induced by surface waves, *Appl. Opt.*, *45*(19), 4726-4739.

Sabbah, S., S. M. Gray, and C. W. Hawryshyn (2012), Radiance fluctuations induced by surface waves can enhance the appearance of underwater objects, *Limnol. Oceanogr.*, *57*(4), 1025-1041.

Sasaki, T., S. Watanabe, G. Oshiba, and N. Okami (1958), Measurements of angular distribution of submarine daylight by means of a new instrument, *J. Oceanogr. Soc. Jpn.*, *14*(2), 47-52.

Sathyendranath, S., and T. Platt (1988), The spectral irradiance field at the surface and in the interior of the ocean: a model for applications in oceanography and remote sensing, *J. Geophys. Res.*, *93*(C8), 9270-9280.

Schenck, H., Jr (1957), On the focusing of sunlight by ocean waves, *J. Opt. Soc. Am.*, *47*(7), 653-657.

Schubert, H., S. Sagert, and R. M. Forster (2001), Evaluation of the different levels of variability in the underwater light field of a shallow estuary, *Helgol. Mar. Res.*, *55*, 12-22.

Scott, D. W. (1979), On optimal and data-based histograms, *Biometrika*, *66*(3), 605-610.

Siegel, D. A., and T. D. Dickey (1987), On the parameterization of irradiance for open ocean photoprocesses, *J. Geophys. Res.*, *92*(C13), 14648-14662.

Siegel, D. A., and T. D. Dickey (1988), Characterization of downwelling spectral irradiance fluctuations, *Proc. SPIE*, *925*, 67-74.

Siegel, D. A., A. F. Michaels, J. C. Sorensen, M. C. O'Brien, and M. A. Hammer (1995), Seasonal variability of light availability and utilization in the Sargasso Sea, *J. Geophys. Res.*, *100*(C5), 8695-8713.

Siegel, D. A., S. Maritorena, N. B. Nelson, M. J. Behrenfeld, and C. R. McClain (2005), Colored dissolved organic matter and its influence on the satellite-based characterization of the ocean biosphere, *Geophys. Res. Lett.*, *32*(L20605), doi:10.1029/2005GL024310.

Smith, R. C. (1974), Structure of solar radiation in the upper layers of the sea, in *Optical Aspects of Oceanography*, edited by N. G. Jerlov and E. Steemann Nielsen, pp. 95-119, Academic Press, New York.

Smith, R. C., R. W. Austin, and J. E. Tyler (1970), An oceanographic radiance distribution camera system, *Appl. Opt.*, *9*(9), 2015-2016.

Smith, R. C., C. R. Booth, and J. L. Star (1984), Oceanographic bio-optical profiling system, *Appl. Opt.*, *23*(16), 2791-2797.

Snyder, R. L., and J. Dera (1970), Wave-induced light-field fluctuations in the sea, *J. Opt. Soc. Am.*, *60*(8), 1072-1079.

Spinrad, R. W., K. L. Carder, and M. J. Perry (1994), *Ocean optics*, 283 pp., Oxford University Press; Clarendon Press, New York; Oxford.

Steemann Nielsen, E. (1974), Light and primary production, in *Optical Aspects of Oceanography*, edited by N. G. Jerlov and E. Steemann Nielsen, pp. 361-388, Academic Press, New York.

Stoll, S. (2009), Effects of light level fluctuations on the early life stages of fish in the littoral zone of lakes, PhD thesis, 168 pp, University of Konstanz, Konstanz, Germany.

Stotts, L. B., and S. Karp (1982), Wave slope statistics derived from optical radiance measurements below the sea surface, *Appl. Opt.*, *21*(6), 976-981.

Strain, P. M., and P. A. Yeats (1999), The relationships between chemical measures and potential predictors of the eutrophication status of inlets, *Mar. Pollut. Bull.*, *38*(12), 1163-1170.

Stramska, M., and T. D. Dickey (1998), Short-term variability of the underwater light field in the oligotrophic ocean in response to surface waves and clouds, *Deep-Sea Res. Pt I.*, *45*(9), 1393-1410.

Stramski, D. (1986a), Fluctuations of solar irradiance induced by surface waves in the Baltic, *B. Pol. Acad. Sci. Earth*, *34*(3), 333-344.

Stramski, D. (1986b), The effect of daylight diffuseness on the focusing of sunlight by sea surface waves, *Oceanologia*, *24*, 11-27.

Stramski, D., and J. Dera (1988), On the mechanism for producing flashing light under a wind-disturbed water surface, *Oceanologia*, *25*, 5-21.

Stramski, D., G. Rosenberg, and L. Legendre (1993), Photosynthetic and optical properties of the marine chlorophyte Dunaliella tertiolecta grown under fluctuating light caused by surface-wave focusing, *Mar. Biol.*, *115*(3), 363-372.

Sverdrup, H. U., M. W. Johnson, and R. H. Fleming (1942), *The Oceans: Their Physics, Chemistry, and General Biology*, 1087 pp., Prentice-Hall, Inc., New York.

Talaulikar, M., S. Thayapurath, E. Desa, S. G. P. Matondkar, T. S. Kumar, A. Lotliker, and A. Inamdar (2012), Empirical algorithm to estimate the average cosine of underwater light field at 490 nm, *Remote Sens. Lett.*, *3*(7), 585-593.

Toffoli, A., A. Babanin, M. Onorato, and T. Waseda (2010), Maximum steepness of oceanic waves: Field and laboratory experiments, *Geophys. Res. Lett.*, *37*(5), L05603,doi:05610.01029/02009GL041771.

Torrence, C., and G. P. Compo (1998), A practical guide to wavelet analysis, *B. Am. Meteorol. Soc.*, *79*(1), 61-78.

Twardowski, M. S., J. M. Sullivan, P. L. Donaghay, and J. R. V. Zaneveld (1999), Microscale quantification of the absorption by dissolved and particulate material in coastal waters with an ac-9, *J. Atmos. Oceanic Tech.*, *16*(6), 691-707.

Twardowski, M. S., M. R. Lewis, A. H. Barnard, and J. R. V. Zaneveld (2005), In-water instrumentation and platforms for ocean color remote sensing applications, in *Remote Sensing of Coastal Aquatic Environments: Technologies, Techniques and Applications*, edited by R. L. Miller, C. E. Del Castillo and B. A. McKee, pp. 69-100, Springer, Norwell, MA.

Twardowski, M. S., X. Zhang, S. Vagle, J. M. Sullivan, S. Freeman, H. Czerski, Y. You, L. Bi, and G. Kattawar (2012), The optical volume scattering function in a surf zone inverted to derive sediment and bubble particle subpopulations, *J. Geophys. Res.*, *117*(C00H17), doi:10.1029/2011JC007347.

Tyler, J. E. (1958), Radiance distribution as a function of depth in the submarine environment, *SIO Ref.*, *58-25*.

Tyler, J. E. (1960), Radiance distribution as a function of depth in an underwater environment, *Bull. Scripps Inst. Oceanogr. Univ. Calif.*, *7*, 363-411.

Voss, K. J. (1989a), Use of the radiance distribution to measure the optical absorption coefficient in the ocean, *Limnol. Oceanogr.*, *34*(8), 1614-1662.

Voss, K. J. (1989b), Electro-optic camera system for measurement of the underwater radiance distribution, *Opt. Eng.*, *28*(3), 384-387.

Voss, K. J., and G. Zibordi (1989), Radiometric and geometric calibration of a visible spectral electro-optic fisheye camera radiance distribution system, *J. Atmos. Oceanic Tech.*, *6*(4), 652-662.

Voss, K. J., and A. L. Chapin (1992), Next generation in-water radiance distribution camera system, paper presented at Ocean Optics XI, SPIE, San Diego, California, 20-22 July.

Voss, K. J., and A. Morel (2005), Bidirectional reflectance function for oceanic waters with varying chlorophyll concentrations: measurements versus predictions, *Limnol. Oceanogr.*, *50*(2), 698-705.

Voss, K. J., and A. Chapin (2005), Upwelling radiance distribution camera system, NURADS, *Opt. Express*, *13*(11), 4250-4262.

Voss, K. J., A. Morel, and D. Antoine (2007), Detailed validation of the bidirectional effect in various case 1 waters for application to ocean color imagery, *Biogeosciences*, *4*(5), 781-789.

Voss, K. J., C. D. Mobley, L. K. Sundman, J. E. Ivey, and C. H. Mazel (2003), The spectral upwelling radiance distribution in optically shallow waters, *Limnol. Oceanogr.*, *48*(1, Part 2), 364-373.

Voss, K. J., S. McLean, M. R. Lewis, C. Johnson, S. Flora, M. Feinholz, M. Yarbrough, C. C. Trees, M. S. Twardowski, and D. K. Clark (2010), An example crossover experiment for testing new vicarious calibration techniques for satellite ocean color radiometry, *J. Atmos. Oceanic Tech.*, *27*(10), 1747-1759.

Walker, R. E. (1994), *Marine Light Field Statistics*, 675 pp., John Wiley & Sons, Inc., New York.

Walsh, P., and L. Legendre (1983), Photosynthesis of natural phytoplankton under high frequency light fluctuations simulating those induced by sea surface waves, *Limnol. Oceanogr.*, *28*(4), 688-697.

Waterman, T. H. (1954), Polarization patterns in submarine illumination, *Science*, *120*(3127), 927-932.

Waters, K. J., R. C. Smith, and M. R. Lewis (1990), Avoiding ship-induced light-field perturbation in the determination of oceanic optical properties, *Oceanography*, *3*(2), 18-21.

Weber, V. (2010), Coefficient of variation of underwater irradiance fluctuations, *Radiophys. and Quantum Electronics*, *53*(1), 13-27.

Wells, W. H. (1973), Theory of small angle scattering, *Optics of the Sea*, *AGARD Lecture Series 61*, 3.3-1- 3.3-19.

Whitney, L. V. (1941), The angular distribution of characteristic diffuse light in natural waters, *J. Mar. Res.*, *4*(2), 122-131.

Wyatt, C. L., V. Privalsky, and R. Datla (1998), *Recommended Practice: Symbols, Terms, Units and Uncertainty Analysis for Radiometric Sensor Calibration*, 120 pp., U.S. Dept. of Commerce, Washington, D.C.

Xing, X., A. Morel, H. Claustre, D. Antoine, F. D'Ortenzio, A. Poteau, and A. Mignot (2011), Combined processing and mutual interpretation of radiometry and fluorimetry from autonomous profiling Bio-Argo floats: Chlorophyll a retrieval, *J. Geophys. Res.*, *116*(C6), doi:10.1029/2010JC006899.

Yakubenko, V. G., and V. P. Nikolayev (1978), Experimental studies of brightness fluctuations of the underwater light field, *Izv. Atmos. Ocean. Phys.*, *14*(8), 624-628.

Yakubenko, V. G., V. P. Nikolayev, and M. S. Khulapov (1978), Effect of light-sensor drift on the results of spectral research into fluctuations of the underwater light field, *Izv. Atmos. Ocean. Phys.*, *14*(5), 406-409.

Yakubenko, V. G., V. P. Nikolayev, O. I. Prokopov, A. A. Zhil'tsov, and L. M. Nesterenko (1974), On the brightness fluctuations of an underwater light field, *Izv. Atmos. Ocean. Phys.*, *10*(9), 1009-1013.

You, Y., D. Stramski, M. Darecki, and G. W. Kattawar (2010), Modeling of wave-induced irradiance fluctuations at near-surface depths in the ocean: a comparison with measurements, *Appl. Opt.*, *49*(6), 1041-1053.

You, Y., G. W. Kattawar, K. J. Voss, P. Bhandari, J. Wei, M. Lewis, C. J. Zappa, and H. Schultz (2011), Polarized light field under dynamic ocean surfaces: numerical modeling compared with measurements, *J. Geophys. Res.*, *116*(C00H05), doi:10.1029/2011JC007278.

Young, I. R. (1999), *Wind Generated Ocean Waves*, 288 pp., Elsevier Science Ltd, Oxford, UK.

Zaneveld, J. R. V. (1974), New developments of the theory of radiative transfer in the oceans, in *Optical Aspects of Oceanography*, edited by N. G. Jerlov and E. Steemann Nielsen, pp. 121-134, Academic Press Inc, New York, NY.

Zaneveld, J. R. V., and R. W. Spinrad (1980), An arc tangent model of irradiance in the sea, *J. Geophys. Res.*, *85*(C9), 4919-4922.

Zaneveld, J. R. V., E. Boss, and P. A. Hwang (2001a), The influence of coherent waves on the remotely sensed reflectance, *Opt. Express*, *9*(6), 260-266.

Zaneveld, J. R. V., E. Boss, and A. Barnard (2001b), Influence of surface waves on measured and modeled irradiance profiles, *Appl. Opt.*, *40*(9), 1442-1449.

Zappa, C. J., M. L. Banner, H. Schultz, J. R. Gemmrich, R. P. Morison, D. A. LeBel, and T. D. Dickey (2012), An overview of sea state conditions and air-sea fluxes during RaDyO, *J. Geophys. Res.*, *117*(C00H19), doi:10.1029/2011JC007336.

Zibordi, G., and J. F. Berthon (2001), Relationships between Q-factor and seawater optical properties in a coastal region, *Limnol. Oceanogr.*, *46*(5), 1130-1140.

Zibordi, G., D. D'alimonte, and J. F. Berthon (2004a), An evaluation of depth resolution requirements for optical profiling in coastal waters, *J. Atmos. Oceanic Tech.*, *21*, 1059-1073.

Zibordi, G., J. F. Berthon, and D. D'Alimonte (2009), An evaluation of radiometric products from fixed-depth and continuous in-water profile data from moderately complex water, *J. Atmos. Oceanic Tech.*, *26*(1), 91-106.

Zibordi, G., S. B. Hooker, J. Mueller, and G. Lazin (2004b), Characterization of the immersion factor for a series of in-water optical radiometers, *J. Atmos. Oceanic Tech.*, *21*(3), 501-514.